UNIVERSITÀ DI NAPOLI FEDERICO II
Dipartimento di Scienze Fisiche

INTERNATIONAL PHD SCHOOL IN NOVEL TECHNOLOGIES
FOR MATERIALS, SENSORS AND IMAGING

XXI COURSE

Phase-sensitive detection in Raman Tweezers: biological applications

Anna Chiara De Luca

TUTOR: Prof. Antonio Sasso

CO-TUTOR: Prof. Paolo Russo

ACADEMIC YEAR 2007-2008

Contents

List of Figures

List of Tables

Introduction

In the biomedicine field, scientists act as detectives working hard to unravel the mysteries surrounding cells. To this end, Raman spectroscopy has revealed itself particularly useful, providing information concerning both the chemical composition and the structural conformation of the investigated samples. If compared to many other techniques devoted to the identification of microorganisms (as for instance fluorescence spectroscopy), Raman spectroscopy presents the relevant advantage of providing sharp peaks correlated to vibrational modes of the investigated sample. Moreover, it is a noninvasive technique, not requiring the addition of chemical agents or labels for a sample identification.

Therefore, Raman spectra behave as the fingerprints of the analyzed sample. Hence, the Raman spectroscopy technique represents a powerful tool to detect cellular transformations in real time, contributing to elucidate many biochemical processes even in living cells [1].

However, the analytical capabilities of Raman spectroscopy are limited by its inability to manipulate, and therefore analyze the samples without making physical contact or disturbing their unique environment. This limitation has been resolved by coupling Raman spectroscopy to a technology called Optical Tweezers (OT). The new method, termed Raman Tweezers (RT), employs Optical Tweezers to trap a microsized object in order to confine its motion for Raman spectroscopic analysis [2].

Optical Tweezers are based on the force exerted on micrometer-sized particles by a strongly focused laser beam. They allow trapping and manipulation of single particles without any mechanical contact [3]. The technique, which was first developed by Arthur Ashkin *et al.* in 1970 [4], has the ability to control objects ranging in size from 5 nm to over 100 μm, among which atoms, viruses, bacteria, proteins, cells, or other biological molecules [5–7]. In such a way, a single selected particle can be

spectroscopically analyzed in its natural environment, without any need to fix it to a substrate.

Therefore, Raman Tweezers have the capability to analyze a molecule from each angle and therefore provide more accurate information about identity, structure, and conformation. In addition, sample confinement in the laser beam focus maximizes the excitation and collection of Raman scattering and, at the same time, reduces the intrinsic interference effects due to the cover plate [8]. This optical trap also allows Raman Tweezers to easily separate molecules for an isolated study, such as their response to different conditions and/or treatments [9].

The first publication on using Raman Tweezers for living cells dates back to 2002 [10]. In their work, Ajito and Torimitsu, by combining the laser trapping technique with near-infrared Raman (NIR) spectroscopy, analyzed single cellular organelles in the nanometer range. The samples were synaptosomes, nerve-ending particles (about 500-700 nm in diameter) isolated from a neuron in a rat brain, dispersed in the phosphate buffer solution. The NIR laser Raman trapping system captured a single synaptosome without photochemical damage and provided a Raman spectrum of the sample with less fluorescence background.

Over the course of the next six years, the techniques of Raman Tweezers have made unique and revolutionary contributions to the experimental studies in the fields of biophysics. Raman Tweezers has been applied for the identification and characterization of single optically trapped microparticles, red blood cells, yeast cells, bacterial cells, and liposomal membranes [11,12]. For instance, a Raman Tweezers system was used to control and to characterize the coagulation of two liquid aerosol droplets and to investigate the formation and properties of multiphase aerosol [13]. Recently, RT has also been reported to identify the bacterial spores in aqueous solution, in which bacterial spores are discriminated from non-biological particles, such as polystyrene spheres, on the basis of Raman signature [14]. Unilamellar phospholipid vesicle were optically trapped and the effect of optical forces on the lipid membrane shape was investigated by using confocal Raman microscopy [15]. Near infrared laser tweezers Raman spectroscopy system was also applied to study the effect of alcohol on single human red blood cells [16] and to distinguish activation-dependent phases of T cells [17]. As matter of fact, Raman Tweezers has the potential to become an incredibly effective diagnostic tool, and therefore holds great promise in the field of biomedicine for distinguishing between normal and diseased cells.

In my PhD-work, mainly performed in the *Laser Spectroscopy and Optical Manipulation group* of Prof. A. Sasso, I have started a new research activity consisting of the Raman analysis of single particles of bio-technological interest. To achieve this goal, the following steps have been followed:

- Build-up of a RT system allowing Raman analysis of an optically trapped cell in a non-invasive way.

- Implementation of a novel electronics method, allowing an optimum suppression of scattering signal from the environment surrounding the optically trapped object.

- Applicability test of the Raman Tweezers technique to model experiments. In particular, I have focused my research on the characterization of normal and thalassemic red blood cells.

Since the aim of my thesis is to study living cells *in vivo*, with particular reference to red blood cells (RBCs), the main challenges have been to find correct laser wavelength and intensity, alignment and calibration of the Raman Tweezers system and finally its application to demonstrate its usefulness.

Erythrocyte are used as model organism in these Raman Tweezers experiments. In fact, the human RBCs represent a very simple cell, they are devoid of the nucleus and are rich in hemoglobin (Hb), a protein composed of four globular protein with an embedded heme group. The heme group presents a strong Hb-absorption band in the visible region [18]. This feature gives rise to a resonant enhancement of the Hb-signal, when it is an excitation wavelength closed to the heme electronic absorption bands. In such a way, it becomes possible to acquire the Raman spectrum of the Hb inside a single erythrocyte without any influence of the surrounding globin or other parts of the RBC crossed by the Raman probe [19–21]. This is a quite interesting issue for the characterization of Hb-related blood diseases, such as thalassemias. Therefore, it has been chosen a doubled frequency Nd:YVO laser (at 532 nm) to excite the Raman spectra.

The most widespread RT systems use two separate beams for trapping and the Raman excitation (for example [22]) with a single objective. This configuration has the advantage that the wavelength and the power of the trapping beam and the Raman probe can be adjusted independently. Also in the present work, it has been

used a two-wavelength Raman Tweezers system, where an IR laser (Nd:YAG at 1064 nm) has been used to trap the sample. This selection has revealed to be quite useful, mainly because it becomes possible to study living cells (RBCs) for long time periods, keeping the level of photo-damage low.

After building the RT set-up, it has been possible to characterize the system by acquiring the Raman spectra of trapped polystyrene beads. By this preliminary study, it has been clear the presence of a general problem affecting both Raman spectrometers and Raman Tweezers systems, i.e. the background caused by the environment surrounding the sample under investigation. It is possible to find many practical experimental situations in which the inelastic as well as elastic scattering from the solvent, in which the sample is embedded, can affect severely the reliability and reproducibility of the measurements. This happens, for instance, when the solvent has strong Raman-active bands that spectrally overlap with the sample Raman features. In this case, reasonable but often distorted spectra are created using either manual or automatic subtraction procedures [23]. This drawback is particularly relevant when Raman spectroscopy is used to monitor the health state of single microorganism. In fact, the diagnosis of cellular disorders is often performed by monitoring the relative intensities of selected Raman peaks. Therefore, it is required a high accuracy in subtracting the solvent contribution [2, 24]. To tackle this problem, during my PhD work, I have implemented a novel method that allows acquiring Raman spectra of a single trapped particle free from any background contribution [25,26]. The method is based on the use of two collinear and copropagating laser beams. The first is devoted to trapping (trap laser), while the second one is used to excite the Raman transitions (pump laser). The trap laser moves the trapped particle periodically, by means of a galvomirror, back and forth across the pump laser. The back-scattered photons are analyzed by a spectrometer and detected by a photomultiplier. Then, the resulting signal is sent to a lock-in amplifier for *phase-sensitive* detection. The obtained results demonstrate that our Raman Tweezers system may find valuable applications in rapid sensing of biological samples in aqueous solutions.

Finally, it has been demonstrated the potential of the developed Raman Tweezers system as a diagnostic tool to study a specific disease related to oxygenation capability of individual red blood cells, known as thalassemia. Thalassemia is the name of a group of genetic blood disorders. In thalassemia, the genetic defect results in reduced rate of synthesis of one of the globin chains that make up the Hb. If there is

a reduced synthesis of one of the globin chains, the RBCs do not form properly and cannot carry sufficient oxygen. By way of a resonant excitation of Hb Raman bands, it has been examined the oxygenation capability of both normal and thalassemic erythrocytes. A reduction of this fundamental erythrocyte function for thalassemia has been shown. Raman spectroscopy has been also used to draw hemoglobin distribution inside single erythrocytes. The results have confirmed the characteristic anomaly (target shape), occurring in thalassemia and some other blood disorders. Finally, the deformability of thalassemic erythrocytes has been quantified by measuring the membrane shear modulus using an Optical Stretcher (double-trap system).

The success of the spectroscopical and mechanical characterization of normal and thalassemic RBCs reported in this thesis provide an interesting starting point to explore the application of Raman Tweezers systems in the analysis of several blood disorders.

The structure of the thesis can be summarized as follow.

Chapter 1 describes the basic physical principles of Optical Tweezers, its biological application and its current state of the art.

Chapter 2 gives an overview of the theory and of the applications of Raman Spectroscopy. The aim of this chapter is to demonstrate the capability of Raman spectroscopy to provide microscopic information especially of biological materials. Particular interest is devoted to describe a combination of Raman microscopy with Optical Tweezers (Raman Tweezers).

Chapter 3 describes in detail the experimental setup developed to characterize spectroscopically and also mechanically single-cells.

Chapter 4 introduces Raman measurement methods based on standard confocal and *phase-sensitive* techniques. In particular, in this chapter, they are described the benefits of the novel *phase-sensitive* method to analyze a single trapped particle in aqueous solution free from any background contribution.

Chapter 5 shows the use of Raman Tweezers combined with a *phase-sensitive* detection scheme. This chapter is mainly devoted to a systematic characterization of the novel technique. In particular, it is described in detail the formation of the Raman signal and its dependence on several parameters, such as the height

from the coverslip surface, the size of the bead, the amplitude of the spatial modulation of the trapped particle, and the pump laser intensity. Finally, a comparison with the standard confocal Raman microscopy is also shown.

Chapter 6 presents the results of the characterization of the RBCs from normal and thalassemic donors obtained by using an Optical Tweezers system integrated with a Raman probe. In particular, it is compared the Raman spectrum of a single thalassemic RBC with that obtained from an healthy subject, relating the observed differences to the analyzed disease. They are also investigated the photo-induced effects caused by the laser radiations used for both trapping and Raman excitation.

Chapter 7 shows how Raman analysis can be used to map the hemoglobin distribution inside single erythrocytes (Raman imaging). In particular, the results shown in this section reveal the characteristic anomaly (target shape) occurring in thalassemia.

Chapter 8 describes the cellular response to applied mechanical stress, by using an Optical Stretcher system (double-trap system). Some significant difference in the functionality of the thalassemic RBCs with respect to normal erythrocytes are highlighted.

Chapter 9 contains the conclusions based on the performed experiments.

Finally, the thesis includes the list of the publications related to the work here described.

Part I

Theoretical Background

1

Optical Tweezers

Using a strongly focused laser beam, dielectric particles with size from several nanometers up to tens microns can be trapped and manipulated without any mechanical contact. These so-called "Optical Tweezers" are an important tool for the research in chemistry, physics and biology.

In this chapter I will discuss the basic physical principles of the Optical Tweezers and the main calibration procedure. Finally, I will briefly show an overview on the theory and show some applications based on the Optical Tweezers.

1.1   Introduction to the Optical Tweezers

The Optical Tweezers (OT) trace their origin back to the time of the discovery of significant radiation pressure forces on dielectric spheres using lasers. Although this technique can be considered relatively recent, the physics behind the OT has been known for a long time.

In his manuscript "De Cometis" of 1619, the German astronomer Johannes Kepler wrote that the comets tails point away from the sun because they are "pushed" in

that direction by the sun radiation. Two centuries later, James Clerk Maxwell, in his theory of electromagnetism, confirmed theoretically that light itself can exert an optical force (*radiation pressure*) on matter. The existence of the radiation pressure was demonstrated experimentally only in the first decade of the twentieth century by Peter Lebedev in a series of experiments showing that parallel plates in vacuum rotated when illuminated with light. The advent of lasers in the 1960 finally enabled researchers to study the radiation pressure through the use of intense, collimated light beams. An early pioneer of such studies was Arthur Ashkin of Bell Laboratories. By focusing laser light, Ashkin *et. al* in 1970 showed that micrometric polystyrene spheres could be levitated against gravity using the force of radiation pressure [4,27]. Radiation pressure forces are those arising from the momentum of the light itself. Ashkin and Chu also worked on trapping and manipulation of atoms [5], and Steven Chu received the Nobel Prize in Physics for the development of methods to cool and trap atoms with laser light in 1997 [28]. In 1987, Ashkin began to trap living biological objects in a three-dimensional trap using a single laser [6,7]. Over the course of the next 20 years or so the techniques of optical trapping and manipulation have made unique and revolutionary contributions to the experimental studies in the fields of light scattering, atomic physics, biophysics and chemistry (see Fig. 1.1).

These optical manipulation techniques can be applied to neutral particles as diverse as:

1. small dielectric spheres in the size range from tens nanometers to tens microns (including biological particles such as viruses, bacteria, living cells, organelles within cells and macromolecules),

2. atoms and molecules at temperatures ranging from hundreds of degrees Kelvin down to about one nanokelvin,

3. atomic particles in Bose-Einstein and fermionic condensates in atomic vapors.

Among the unique capabilities of the optical manipulation there is the simple ability to non-invasively hold single particle fixed in space, free from any mechanical support, using a single beam of light. A submicrometer particle in a trap, can be localized to within a small fraction of a wavelength of radiation [29] or moved over long distance of many centimeters [30].
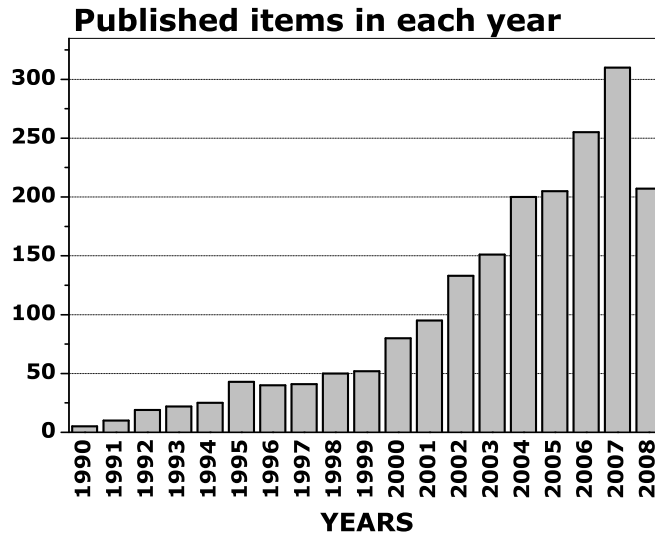
Figure 1.1: *Yearly number of publications about the topic "Optical Tweezers" indexed within Web of Science.*

Optical Traps are also well suitable to study the mechanics or dynamics at cellular and subcellular levels. In fact, although optical forces (few pN) are minuscule on the scale of larger organism, they can be significant on the scale of macromolecules, organelles and cells. A force of ten piconewtons can stretch, bend or distort single macromolecules, such as DNA and RNA, or macromolecular assemblies, including microtubules and actin filaments.

There are many excellent review papers that give an overview of the optical tweezers, the theory underlying them, their construction, their application, and recent developments [31].

In particular, in this chapter, I will introduce the principles behind the Optical Tweezers and examine the forces on a bead trapped by a laser.

1.2   Theory of the Optical Tweezers

An optical trap is formed by tightly focusing a laser beam with an objective lens of high numerical aperture (NA). As matter particles do, also light quanta or photons carry a momentum p:

$$p = \frac{E}{c} = \frac{h\nu}{c} = \frac{h}{\lambda} \tag{1.1}$$

where $E = h\nu$ is the energy of a photon of frequency ν and wavelength λ. The optical trap is based on the transfer of momentum between the beam of radiation and the object that it is passing through (*radiation pressure*). For macroscopic objects, the radiation pressure exerted by typical light sources is many orders of magnitude too small to have any measurable effect. However, a focused laser beam can be used to trap small objects (<100 μm) in a three dimensional "potential well".

The resulting optical force has traditionally been decomposed into two components: a *scattering* force, in the direction of light propagation and a *gradient* force, in the direction of the spatial light gradient. For stable trapping in all three dimensions the axial gradient component of the force pulling the particle towards the focal region must exceed the scattering component of the force pushing it away from that region. This condition needs a very steep gradient of the light produced by sharply focusing the trapping laser beam to a diffraction-limited spot using an objective of high NA. As a result of this balance between the gradient force and the scattering force, the axial equilibrium position of a trapped particle is located slightly beyond the focal point.

The theoretical description of this effect depends on the size of the trapped objects. One refers to a **ray optics regime** when the diameter of the particle is greater than the wavelength of light ($d \gg \lambda$). In this case diffraction effects can be neglected and the trapping forces of the light can be understood in terms of geometric or ray optics. If the diameter of the particle is smaller than the wavelength of light ($d \ll \lambda$), one needs a description based on electromagnetic dipoles. This regime is called the **Rayleigh regime**. For particles that are in between these two models, an additional model must be used.

1.2.1 Ray optics regime

When the diameter of a particle is much larger than the wavelength of the trapping laser ($d \gg \lambda$), the forces on a particle can be described using ray optics, as it was done by Ashkin in 1992 [32]. When a light ray, travelling in a medium with refractive index n_1, impinges on a dielectric sphere with refractive index n_2, the light ray is refracted according to Snell's law. The light ray is again refracted when it leaves the particle. The momentum of the light ray is changed because of the refraction by the particle. This change in momentum is transferred to the particle because the momentum is conserved.
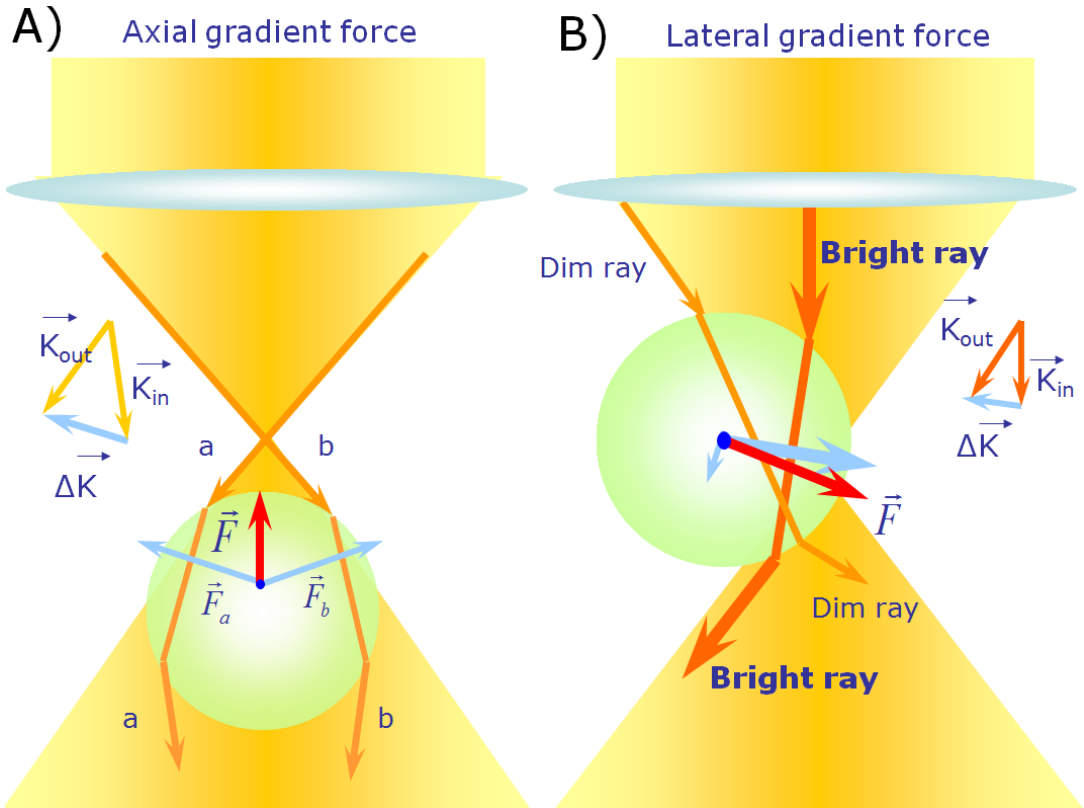
Figure 1.2: *Qualitative view of the origin of the trapping force. Part A: figure shows the axial gradient force towards the focus of the trapping beam. Part B: figure shows the lateral gradient force of a non-uniformly distributed laser beam.*

The ray-optics diagram used in Fig. 1.2 gives a qualitative description of the trapping. In this figure, the trap action on a dielectric sphere is described in terms of the total force due to a typical pair of rays *a* and *b* of the converging beam, under the simplifying assumption of zero surface reflection. In this approximation the forces F_a and F_b are entirely due to refraction and are shown pointing to the direction of the momentum change. One sees that for arbitrary displacements of the sphere origin O from the focus f the vector sum of F_a and F_b gives a net restoring force F directed back to the focus (Fig. 1.2-part A), and the trap is stable (axial gradient force). The lateral gradient force (Fig. 1.2-part B) can be understood as follows. If *bright* and *dim* rays come from parts of the beam with different intensity, the momentum changes of the rays differ in magnitude, causing a net reaction force on the refracting medium in the direction of the high intensity.

A light beam is described as a collection of light rays and each individual ray is weighted according to its intensity. The contributions of all rays are summed to calculate the total optical force on a particle.
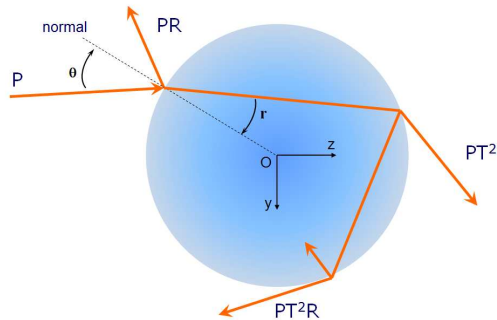
Figure 1.3: *Geometry needed to calculate the force due to the scattering of a single incident ray of power* P *by a dielectric sphere, showing the reflected ray* PR *and infinite set of refracted rays* PT^2R^n.

Let us consider first the force due to a single ray of power P hitting a dielectric sphere at an angle of incidence θ with incident momentum per second of $n_1 P/c$ (see Fig. 1.3). The total force on the sphere is the sum of the contributions due to the reflected ray of power PR and the infinite number of emergent refracted rays with decreasing

power PT^2, PT^2R, ... PT^2R^n... .The quantities R and T are the Fresnel reflection and transmission coefficients of the surface at θ. The net force acting through the origin O can be broken into F_Z and F_Y, given by:

$$F_Z = F_{scatt} = \frac{n_1 P}{c}\{1 + R\cos 2\theta - \frac{T^2[\cos(2\theta - 2r) + R\cos 2\theta]}{1 + R^2 + 2R\cos 2r}\} \quad , \tag{1.2}$$

$$F_Y = F_{grad} = \frac{n_1 P}{c}\{R\sin 2\theta - \frac{T^2[\sin(2\theta - 2r) + R\sin 2\theta]}{1 + R^2 + 2R\cos 2r}\} \quad , \tag{1.3}$$

where θ and r are the angles of incidence and refraction. These formulas sum over all scattered rays and they are exact therefore. The forces are polarization dependent since R and T are different for rays polarized perpendicular or parallel to the plane of incidence.

In Eq. 1.2, F_Z indicates the component pointing to the direction of the incident ray, also known as *scattering force* component F_{scatt}. Similarly, in eq. 1.3, F_Y indicates the component pointing to the direction perpendicular to the ray, also known as *gradient force* component F_{grad}.

The vectorial sum of these two trapping force components gives the total force due to a single ray of power P:

$$F_Y = F_{grad} = \frac{n_1 P}{c}\sqrt{Q_{scatt}^2 + Q_{grad}^2} = \frac{n_1 P}{c}Q(\theta, \frac{n_2}{n_1}, R, T) \quad , \tag{1.4}$$

where Q is the dimensionless efficiency and the variables determining the effective Q-value have been explicitly stated. The total force exerted on the object is found by summing over all rays passing through it. Ashkin has worked out these calculations for a laser beam with a Gaussian profile [32].

1.2.2 Rayleigh regime

When the diameter (d) of a particle is much smaller than the wavelength of the trapping laser, the optical forces on the particle can be calculated by treating the particle as an induced point dipole which scatters light elastically.

The trapping light exerts a scattering force on the induced dipole as it absorbs and reradiates light from the trapping beam. The scattering force is proportional to the optical intensity and points toward the propagation of the laser light [6]. The scattering force is described by the equation below [33]:

$$F_{scatt} = n_m \frac{<S>\sigma_{scatt}}{c} \quad , \tag{1.5}$$

where

$$\sigma_{scatt} = \frac{8}{3}\pi(kr)^4 r^2 (\frac{m^2-1}{m^2+2})^2 \ , \tag{1.6}$$

is the scattering cross section of a Rayleigh sphere with radius r [34]. The quantity $<S>$ is the time averaged Poynting vector, where n is the refractive index of the particle, n_m is the refractive index of the medium, $m = n/n_m$ is the relative index, and $k = 2\pi n_m/\lambda$ is the wavenumber of the light.

As the laser polarizes the object, the object experiences a force in the direction of gradient of the electromagnetic field. This gradient force is proportional to the gradient intensity and points to the direction of the intensity gradient [6]. The gradient force is the polarizability of the particle. It is defined by the following equation [33]:

$$F_{grad} = \frac{\alpha}{2}\nabla < E^2 > \ , \tag{1.7}$$

where the polarizability α of the particle is:

$$\alpha = n_m^2 r^3 (\frac{m^2-1}{m^2+2}) \ . \tag{1.8}$$

The object then experiences a force directed toward the brighter region of light. A particle with a large dielectric constant within the laser beam will exert a force, which is directed toward the focus of the beam. Thus, a trapped particle can be manipulated, by moving the focus of the beam.

1.2.3   Electromagnetic regime

For particles between *Ray optics* and *Rayleigh* regimes ($\lambda/20 < d < 3\lambda$), theoretical calculations are used to describe the trapping power. This is the region of most interest, yet it is the least described. Biological application of the Optical Tweezers often use spherical dielectric particles with diameters of 0.2-1.0 μm. The previous calculations are not consistent with the experimental data in this region. For such particles, diffraction effects are significant. Moreover, the vector character of the electromagnetic field cannot be neglected, for highly focused laser beams. These factors increase enormously the difficulty of computing realistic forces in the intermediate regime. The time-averaged force due to an arbitrary electromagnetic field, that acts on an arbitrary particle, is given by the following integral over the particle surface:

$$F_i =< \oint_S \mathbf{T}_{ij} dS > \ , \tag{1.9}$$

where the brackets denote a temporal average and T_{ij} [35] is the Maxwell stress tensor:

$$\mathbf{T}_{ij} = \frac{1}{4\pi}[\epsilon E_i E_j + B_i B_j - \frac{1}{2}(\epsilon E_i E_i + B_i B_i)\delta_{ij}] \ , \tag{1.10}$$

where ϵ is the electric permittivity.
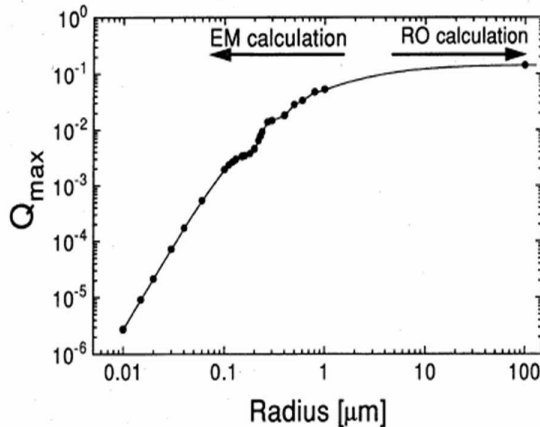
Figure 1.4: *Computed efficiency* Q_{max} *as a function of sphere radius.*

In related work, Wright *et al.* used the *Electromagnetic* and *Ray optics* theory to compute the maximal axial trapping efficiency Q_{max}, for polystyrene beads (n=1.57), as a function of particles size (see Fig. 1.4) [36]. For small radii (*r < 0.1 μm*), trapping force scale with r^3, as expected by Rayleigh theory. The experimental measurements of Q_{max} for beads with different diameter showed that the *Electromagnetic* theory gives better estimates for *r < 1 μm* than *Ray optics* theory, and that the *Ray optics* theory gives good results for *r > 10 μm* (at λ = 1064 nm).

1.3 Optimization of an Optical Trap

From equations 1.2-1.4 it is clear that, at least for the ray optics approach, the trapping forces can be optimized by increasing the laser power *P*, the refractive index of the surrounding medium n_1, or the *Q-values*. The laser power can only be increased up to a certain limit, above which more laser light would lead to heating or photo-damage of the optics of the examined system (especially delicate biomaterials). Increasing the refractive index is hardly ever an option, because most samples

require an aqueous solvent of $n_1 \approx 1.3$. This leaves the geometric *Q-values* as the parameters to be optimized.
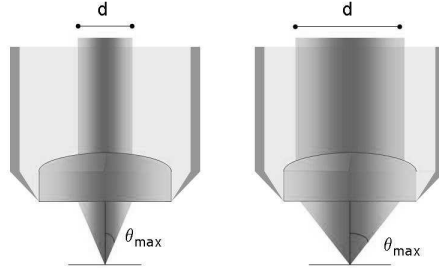
Figure 1.5: *Scheme of a laser beam focused by an objective lens for different beam diameters* d.

The maximum incidence angle θ_{max} is determined by the optics used to focus the laser beam, that usually is a microscope objective lens, as in our case. One of the specifications of an objective is the so-called *numerical aperture* (NA). This is a measure of the solid angle over which the objective lens can gather light. It is defined as:

$$NA = n_3 \sin \theta \ ,\tag{1.11}$$

where n_3 is the refractive index of the immersion medium (i.e. the medium between the sample and the objective lens) and θ is one-half the angular aperture (see figure 1.5). The value of n_3 varies between 1.0 for air and $\sim$1.5 for most immersion oils. The NA of the objective in our setup is 1.4. Another parameter which influences θ_{max} in a similar way is the beam diameter d. As indicated in the figure 1.5, an expanded beam yields a larger θ_{max} and therefore a stronger intensity gradient in the focus. In order to optimize the trapping quality with a Gaussian profile beam, the beam should *overfill* the back aperture of the objective lens. This increases the intensity of the highly convergent rays coming from the edge of the aperture compared to the configuration where the aperture is just filled. These convergent rays contribute largely to F_{grad}, enabling it to overcome F_{scatt}^z.

1.4   Force measurement
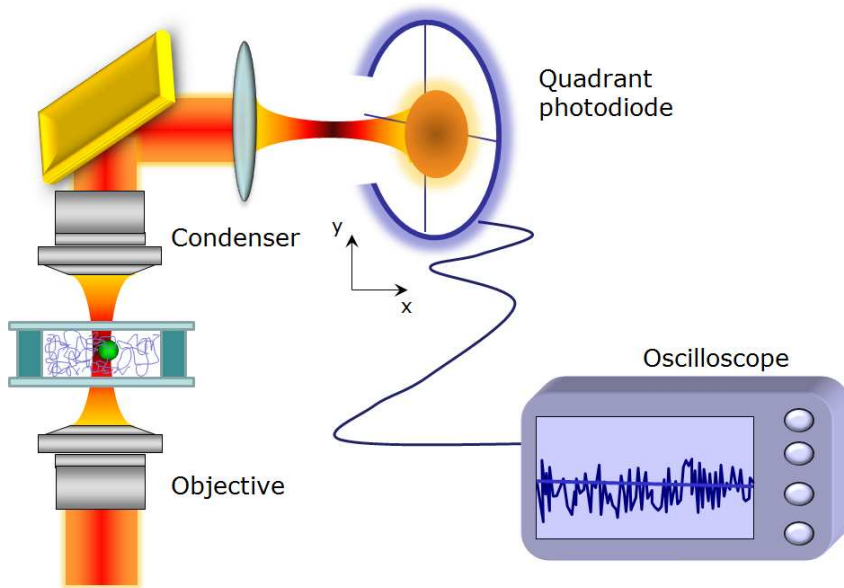
Figure 1.6: *Configuration for the detection of lateral displacement of a trapped sphere from the trap center. The back focal plane of the condenser is imaged onto a quadrant diode. QPD signals are constructed from the signals of the four individual segments of the QPD.*

The Optical Tweezers can be used to measure directly forces on trapped object. These external forces tend to push or pull the particle from the center of the trap. In turn, the refractive object refracts the rays passing through it. Gittes and Schmidt [37] have developed a model based on the far-field interference of the outgoing laser light with the scattered light from the trapped particle. This model describes intensity shifts due to the lateral (i.e. off-axis) displacement of the particle. The illuminating and scattered light is collimated by a condenser lens of focal length f. In the back focal plane (BFP) of this lens, the intensity distribution does not change when moving the optical trap around in the sample. The distribution is only affected by the motion of the trapped object with respect to the trap. This is the reason why this plane is

imaged onto a quadrant photodiode (QPD), a light sensitive diode divided into four equal segments which is used to detect changes in the intensity distribution. This method of displacement or force detection of a trapped object is known as *back-focal-plane interferometry.*

Figure 1.6 shows the configuration for the detection of the lateral displacement from the trap center. The voltage signal given by the QPD is constructed by the four individual segments of the detector (I_i, i=1,...4) [37]:

$$V_x = (I_1 + I_2) - (I_3 + I_4) \ , \tag{1.12}$$

$$V_y = (I_1 + I_4) - (I_2 + I_3) \ , \tag{1.13}$$

$$V_z = (I_1 + I_2 + I_3 + I_4) \ . \tag{1.14}$$

The hypothesis of the theoretical work of Gittes *et al.* [37] are essentially two: i) the diameter of the trapped particle is smaller than the wavelength of light (Rayleigh) and ìi) the incident beam can be described as a gaussian beam.

The response function from equation 1.12 is plotted in figure 1.7 for a 1 μm sphere diameter. For small displacements the response is approximately linear ($x = \beta V_x$). From a linear fit of the experimental data it is possible to calibrate the response β of the detector.

If a force of known magnitude and direction is applied to the trapped bead (preferably within the linear range) and one observes the response of the quadrant diode signals, one can calibrate the detector to physically relevant units of force or displacement. This procedure will be treated in the next section.

1.5   Calibration of detector signals

The detector response to external forces can be calibrated by using several methods [38]. In this work, we have used the *Brownian motion calibration* [39]. For this method, we measured displacement fluctuations *x(t)* of a trapped bead due to the continuous and random collisions with solvent molecules.

A trapped bead in a viscous fluid will feel both the diffusional forces and a restoring optical force, confining its motion within the laser focus. Assuming the confining
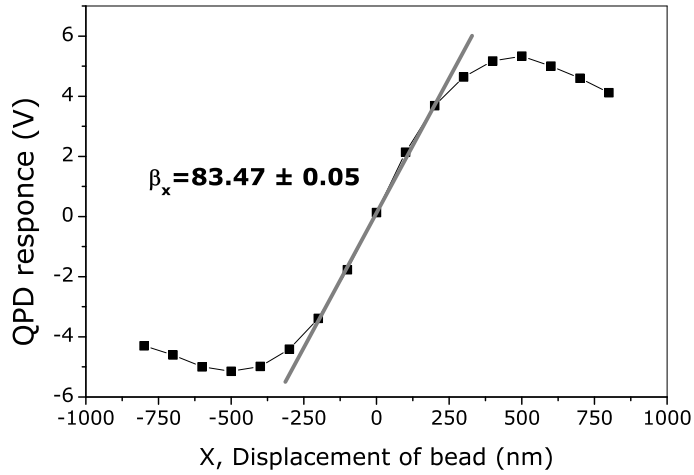
Figure 1.7: *Voltage response versus the displacement of the bead (x), where the linear range is determined by scanning a region of 1 µm with a step size of 100 nm.*

force to be linear in the displacement with a proportionality constant k_x, the *Langevin* equation of the bead's motion becomes:

$$F(t) = \gamma \frac{dx}{dt} + k_x x \ .$$

(1.15)

F(t) represents the random thermal force, which averages to zero over time. The power spectrum of *F(t)*, $S_F(f)$, contains the contribution to *F(t)* of motions with different frequencies. After calculating the Fourier transform of *Langevin* equation 1.15, the power spectral density (PSD) of these fluctuation is found to have a Lorentzian shape:

$$S_x(f) = \frac{k_B T}{\gamma \pi^2 (f_c^2 + f^2)} \ ,$$

(1.16)

where k_B is the Boltzmann factor, T is the temperature, $\gamma = 3\pi\eta d$ is the Stokes drag coefficient for a sphere of diameter d immersed in a fluid of viscosity η and $f_c = k_x/2\pi\gamma$ is called the corner frequency. The corner frequency can now be found fitting the measured PSD with a Lorentzian profile. Because of the linear relation of the

detector signal $x(t) = \beta V_x(t)$ for small displacement $x(t)$, the PSD of the detector signal $S_x^V(f)$ is given by:

$$S_x^V(f) = \frac{1}{\beta^2} \frac{k_B T}{\gamma \pi^2 (f_c^2 + f^2)} = \frac{A}{(f_c^2 + f^2)} \quad , \tag{1.17}$$

and one can see that k_x can be found estimating the corner frequency f_c, by way of a fit procedure, once the solvent viscosity is known.
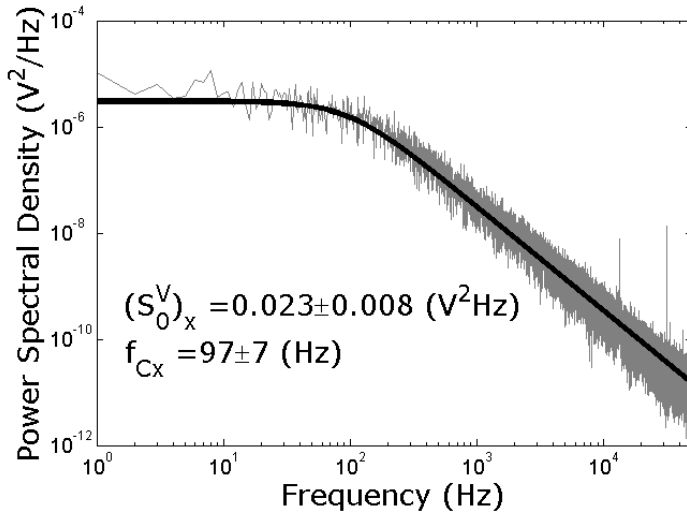
Figure 1.8: *Power spectral density (PSD) of a bead in an optical trap. The PSD can be used to determine the stiffness of the trap.*

Figure 1.8 shows an example of the power spectral density $S_x^V(f)$ for an optically trapped 2-μm polystyrene bead. A Lorentzian fit is plotted in the same figure. At low frequencies, the PSD function will rich a plateau value $S_x^V(0)$ that can be used to calculate sensitivity β. In fact, the equation:

$$S_x^V(0) = \frac{k_B T}{\beta^2 \gamma \pi^2} \quad , \tag{1.18}$$

can be used to calibrate the response β of the detector if the bead diameter and the solvent viscosity are known.

1.6   Applications in Biology

Since their development in 1986, the optical tweezers have had a multitude of applications [40–52].

An early application of the Optical Tweezers in biology involved the measurements of force generation of organelle transport [53]. In particular, Ashkin *at. al.* have trapped single mitochondria (the diameter is 320 nm) and studied the driving force of mitochondria moving along microtubules, allowing them to estimate the force generated by a single motor to be 2.6×10^{-7} dynes.

Experiments were performed with tweezers to manipulate live sperm cells in 3-D and to measure their swimming force [54].

One of the most important biological applications of the Optical Tweezers is to study of molecular motors. These mechanoenzymes interact with microtubules or actin filaments of the cell to generate the forces responsible for cell motility, muscle action, cell locomotion, and organelle movement within cells. In early works using the Optical Tweezers, Block *et al.* [33, 55] attached single kinesin motor molecules to spheres, and placed them directly onto microtubules where they could be activated ATP. Later they studied the detailed motion of a kinesin motor molecules into a sequence of 8-nm steps as it advanced along a microtubule by using an optical trapping interferometric position monitor with sub-nanometer resolution [56]. Finally, Block *et al.* measured the complete force-velocity relationship of single kinesin motors as a function of ATP concentrations [57]. A maximum force of $\sim$ 5-6 pN was observed. Simmons *et al.* [58] shortly thereafter introduced a new feedback enhanced tweezers trap with a detection capability of sub-nanometers in position, piconewtons in force and ms in time response. They studied the interaction of actin with myosin in a dual trap scheme which suspended the actin filament over a single myosin molecule. They observed stepwise motion of about 11 nm and forces of about 3-4 pN.

The optical tweezers have been also applied to single-molecule manipulation or detection. Bustamante *et al.* , for example, used the OT to study the folding/unfolding of RNA hairpins [59–61]. A recent exciting advantage in the field is the extension of tweezers force measuring technique to a new class of motors, the nucleic acid motor enzymes. Using an optical trap the force generated by a single RNA polymerase enzyme has been measured as it pulled itself along a DNA molecule while synthesizing an RNA transcript [62]. The motion is slow, but the motors is surprisingly powerful.

It has been observed to stall reversibly at 14 pN.

In 1999 Hènon and Lenormand [63] determined the shear modulus of human ery-throcytes by using the optical tweezers to apply force. The optical tweezers were used to trap small silica beads diametrically positioned on the red blood cell membrane. The trapping beam was split into two separate beams: the cell was deformed, increasing the distance between the trap.

1.7   Conclusion.

Looking ahead early to the years of new century, it seems fair to predict that the use of optical manipulation techniques will continue to grow at an increasingly rapid pace in the many subfields of physics, chemistry, and biology involving small particles.

In recent years, massive efforts have also been made to combine the Optical Tweezers with several spectroscopic techniques, such as fluorescence [64], absorption [65] and Raman spectroscopy [8]. Among these techniques, the Raman analysis of a trapped object has revealed particularly useful, providing information relative to both the chemical composition and the structural conformation of the investigated samples.

In the next chapter we focus our attention to the theory of Raman scattering.

2

Raman Spectroscopy

The Raman spectroscopy has revealed to be a powerful tool for microscopic analysis of organic and biological materials. When it is combined with the Optical Tweezers (Raman Tweezers), it allows to investigate single, selected micrometric particles in their natural environment. Therefore, unwanted interferences from the cover plate are reduced.

In this chapter I will give an overview of the theory, and show some applications of the Raman Spectroscopy.

2.1   Introduction to the Raman scattering.

When the light is scattered from a molecule, most photons are elastically scattered (Rayleigh scattering). The scattered photons have the same energy (frequency) and wavelength of the incident photons. However, a small fraction of the light (approximately 1 in 10^7 photons) is scattered at optical frequencies usually lower then the frequency of the incident photons. The process leading to this inelastic scatter is termed Raman effect.

The effect of the inelastically scattering of the light was first reported by the In-

dian physicist C. V. Raman [66] and independently by G. Landsberg and L. Mandelstam [67], in 1928. By monitoring the light scattering from various crystalline and amorphus solids, fluids and gases with a mercury arc lamp, Raman succeeded to distinguish elastic scattering from additional spectral bands. He described this findings as a "spectrum of the new radiation", and deemed it as the result of energy exchange between the incident light and the scattering medium. Raman received the Nobel Prize in 1930 for his work and in 1998 the Raman Effect was designated an ACS National Historical Chemical Landmark as a recognition of its significance as a tool for analyzing the composition of liquids, gases, and solids.

The introduction of the laser in the 1960s allowed Raman spectroscopy to be more accessible to the scientific community [68–70]. In the mid 1990's, the next generation of smaller, more compact instruments started to evolve. They utilized newer lasers, optics and detectors and began the micro Raman revolution [71–75].

2.2   Classical theory of Raman scattering.
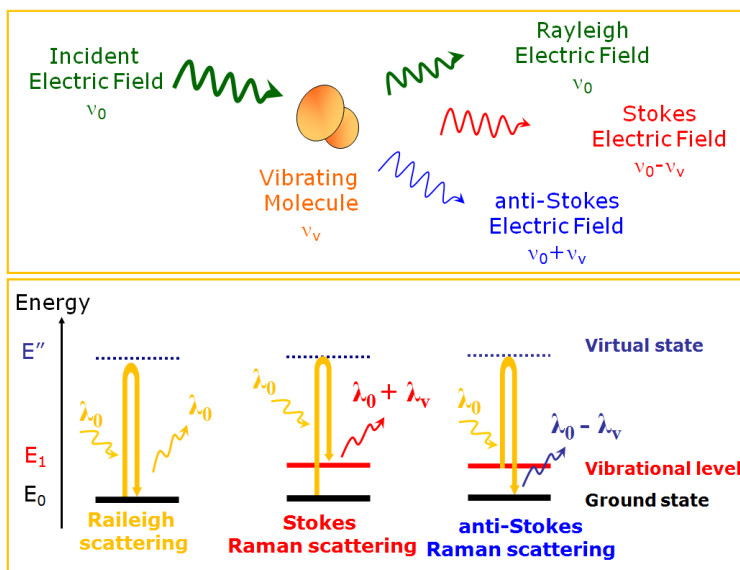
Figure 2.1: *Schematic diagram of Raman scattering by molecules.*

The Raman effect occurs when light impinges upon a molecule and interacts with

the electron cloud of the bonds of that molecule. The incident photon excites one of the electrons into a virtual state. For the spontaneous Raman effect, the molecule will be excited from the ground state to a virtual energy state, and relax into a vibrational excited state, which generates the Stokes Raman scattering. If the molecule is already in an elevated vibrational energy state, the Raman scattering is then called anti-Stokes Raman scattering. A simplified energy diagram that illustrates these concepts is shown in Fig. 2.1. Stokes radiation occurs at lower energy (longer wavelength) than the Rayleigh radiation, and anti-Stokes radiation has greater energy. The energy increase or decrease is related to the vibrational energy levels in the ground electronic state of the molecule, and, the observed Raman shift of Stokes and anti-Stokes features are a direct measure of the vibrational energies of the molecule.

A simple classical electromagnetic field description of the Raman spectroscopy can be used to explain many of the important features of the Raman band intensities [76].

When a molecule is introduced into an electric field E, an electric dipole momentum P is induced in the molecule (see Fig. 2.2). If α is the polarizability of the molecule, then the induced dipole moment is given by:

$$\vec{P} = \alpha \vec{E} \ . \tag{2.1}$$
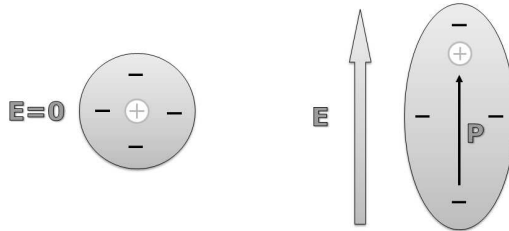
Figure 2.2: *Visualization of an induced dipole momentum before and after an electric field is applied.*

When electromagnetic radiation of frequency ν_0 falls on the molecule, this introduces a varying electric field E whose dependence on the time t is given by:

$$\vec{E} = \vec{E_0} \cos \omega_0 t \ , \tag{2.2}$$

where E_0 is the equilibrium value of the electric field. Hence, from equations 2.1 and

2.2:

$$\vec{P} = \alpha\vec{E_0}\cos\omega_0 t \ \ . \tag{2.3}$$

Thus, the electromagnetic radiation induces a varying electric dipole moment which then permits emission of light identical in frequency the one that of the incident radiation. This is the *Rayleigh scattering*.

In the equation 2.1 both E and P are vectors, and in case of an isotropic molecule both their direction are identical. This makes α scalar. However, for non-isotropic molecules the application of an electric field in a fixed direction induces a moment in different direction, and α becomes a tensor. In general, molecules are non-isotropic, and the three equations which take account of the unequal polarizability along different principal axes of the molecule are:

$$P_x = \alpha_{xx}E_x + \alpha_{xy}E_y + \alpha_{xz}E_z \ \ , \tag{2.4}$$

$$P_y = \alpha_{yx}E_x + \alpha_{yy}E_y + \alpha_{yz}E_z \ \ , \tag{2.5}$$

$$P_z = \alpha_{zx}E_x + \alpha_{zy}E_y + \alpha_{zz}E_z \ \ , \tag{2.6}$$

where for example P_z is the induced electric dipole moment in the direction of the z-axis. The tensor α is defined by these nine coefficients α_{xx}, α_{xy}... α_{zz}. However, since $\alpha_{xy}{=}\alpha_{yx}$, $\alpha_{yz}{=}\alpha_{zy}$ and $\alpha_{xz}{=}\alpha_{zx}$ the tensor α is really defined by six coefficients. If any of these six polarizability coefficients changes during a rotation or a vibration, then the theoretical criterion for a Raman spectrum is satisfied. For very small vibration amplitudes, the polarizability of the molecule is related to the normal vibrational coordinate q_n by the equation:

$$\alpha = \alpha_0 + (\frac{\partial\alpha}{\partial q_n})_0 q_n \ \ , \tag{2.7}$$

where the label zero refers to the coordinate value at equilibrium configuration. Equation 2.7 holds for each of the six coefficients which define α.

The dependence of the normal vibrational frequency ν_v on the normal coordinate q_v is given by:

$$q_v = q_0\cos(\omega_n t) \ \ , \tag{2.8}$$

where q_0 is the normal coordinate of the initial position. Substituting eq. 2.2 in eq. 2.4 we obtain:

$$P_x = (\alpha_{xx}E_x^0 + \alpha_{xy}E_y^0 + \alpha_{xz}E_z^0)\cos(\omega_0 t) \ . \tag{2.9}$$

Taking α from eq. 2.7 and q_n from eq. 2.8 the following expression is obtained:

$$
\begin{aligned}
P_x \ = \ & \left(\alpha_{xx}^0 E_x^0 + \alpha_{xy}^0 E_y^0 + \alpha_{xz}^0 E_z^0\right)\cos(\omega_0 t) + \\[2mm]
& + \left\{ \left(\frac{\partial \alpha_{xx}}{\partial q_n}\right)_0 E_x^0 + \left(\frac{\partial \alpha_{xy}}{\partial q_v}\right)_0 E_y^0 + \left(\frac{\partial \alpha_{xz}}{\partial q_n}\right)_0 E_z^0 \right\} \\[2mm]
& q_0 \cos(\omega_n t)\cos(\omega_0 t) \ .
\end{aligned}
\tag{2.10}
$$

Equation 2.10 may be readily transformed into:

$$
\begin{aligned}
P_x \ = \ & \left(\alpha_{xx}^0 E_x^0 + \alpha_{xy}^0 E_y^0 + \alpha_{xz}^0 E_z^0\right)\cos(\omega_0 t) + \\[2mm]
& + \frac{q_0}{2}\left\{ \left(\frac{\partial \alpha_{xx}}{\partial q_n}\right)_0 E_x^0 + \left(\frac{\partial \alpha_{xy}}{\partial q_n}\right)_0 E_y^0 + \left(\frac{\partial \alpha_{xz}}{\partial q_n}\right)_0 E_z^0 \right\} \\[2mm]
& \{\cos(\omega_0 + \omega_n)t + \cos(\omega_0 - \omega_v)t\} \ .
\end{aligned}
\tag{2.11}
$$

The first term of eq. 2.11 contains only one frequency factor ω_0, that is the one of the incident radiation. This term is interpreted in terms of the *Rayleigh scattering*. In addition to the incident frequency, the second term contains the frequencies $\omega_0 \pm \omega_n$. Thus, the induced dipole moment can also oscillate with two frequencies $\omega_0 \pm \omega_n$, interpreted as the vibrational frequencies. The $\omega_0 - \omega_n$ and $\omega_0 + \omega_n$ frequencies are known, respectively, as the *Stokes* and *anti-Stokes lines*.

Equation 2.11 is important since the α_0 in the first term determines the properties of the Rayleigh radiation, while in the second term $(\partial \alpha / \partial q_n)_0$ determines the properties of the Raman scattering. In fact, it is clear that if $(\partial \alpha / \partial q_n)_0$ equals zero, so do the *Stokes* and *anti-Stokes* terms and there will be no Raman scattering. This gives a selection rule for the Raman-active motions: for a vibration to be Raman active,

the polarizability of the molecule must change with the vibrational motion. Thus, Raman spectroscopy complements the IR spectroscopy (which is based on dipole-moment changes).

Although very simple classical considerations can explain the appearance of the *Stokes* and *anti-Stokes lines*, once the intensity of *Stokes* and *anti-Stokes lines* is considered the classical theory is most unsatisfactory. In fact, the classical theory predicts that the *Stokes* and *anti-Stokes lines* should be of equal intensity, whereas in practice the latter are very much less intense than the former.

A quantum mechanical approach is necessary to describe the intensity in the *Stokes* and *anti-Stokes lines*.

2.3   Quantum theory of Raman scattering
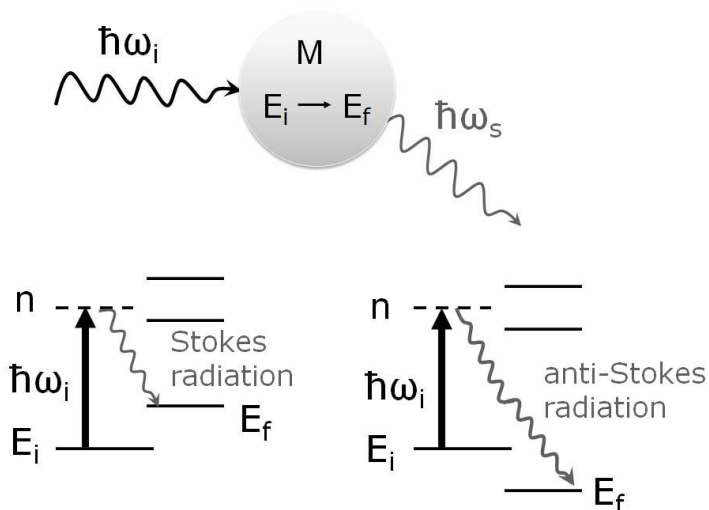
Figure 2.3: *Schematic representation of the quantum theory for Raman scattering.*

In the quantum theory [77,78], the Raman scattering process is viewed as an excitation to a virtual state lower in energy than a real electronic transition with nearly coincident de-excitation and a change in vibrational energy, as schematically reported in Fig. 2.3.

The expectation value of the component α_{ij} of the polarizability tensor is given by:

$$\langle\alpha_{ij}\rangle_{ab} = \int u_b^*(q)\alpha_{ij}u_a(q)dq \ , \tag{2.12}$$

where the function $u(q)$ represent the molecular eigenfunctions in the initial level a and the final level b. The integration extends over all nuclear coordinates. This shows that a computation of the intensities of Raman lines is based on the knowledge of the molecular wave function of the initial and final states.

For small displacement q_n the molecular potential can be approximated by a harmonic potential, where the coupling between the different vibrational modes can be neglected. The functions $u(q)$ are then separable into a product:

$$u(q) = \prod_{n=1}^{Q} w_n(q_n, v_n) \ , \tag{2.13}$$

of vibrational eigenfunction of the nth normal mode with v_n vibrational quanta, where Q=3N-6 (or 3N-5 for linear molecules) gives the number of normal vibrational mode for N nuclei. Using the orthogonality relation:

$$\int w_n w_m dq = \delta_{nm} \ , \tag{2.14}$$

of the functions $w_n(q_n)$, one obtains from eq. 2.12 and eq. 2.7:

$$\langle\alpha_{ij}\rangle_{ab} = \alpha_{ij}^0 + \sum_{n=1}^{Q} \left(\frac{\partial\alpha_{ij}}{\partial q_n}\right)_0 \int w_n(q_n, v_a)q_n w_n(q_n, v_b)dq_n \ . \tag{2.15}$$

The first term is a constant and responsible of the Rayleigh scattering. For nondegenerate vibrations the integrals in the second term vanish unless $v_a = v_b \pm 1$. In this cases its value is $[\frac{1}{2}(v_a + 1)]^{1/2}$ [79]. The basic intensity parameter of the vibrational Raman spectroscopy is the derivative $(\partial\alpha_{ij}/\partial q)$, which can be determined from the Raman spectra.

The intensity of a Raman line at a Stokes or anti-Stokes frequency $(\omega_0 \pm \omega_n)$ is determined by the population intensity $N_i(E_i)$ in the initial level E_i, by the intensity I_L of the incident pump laser, and by the Raman scattering cross section $\sigma_R(i \rightarrow f)$ for the Raman transition $E_i \rightarrow E_f$:

$$I_{Raman} = N_i(E_i)\sigma_R(i \rightarrow f)I_L \ . \tag{2.16}$$

At the thermal equilibrium the population density $N_i(E_i)$ follows the Boltzmann distribution:

$$N_i(E_i) = \frac{N}{Z} g_i e^{-E_i/kT} \quad , \tag{2.17}$$

with $N = \sum N_i$, the partition function $Z = \sum g_i e^{-E_i/kT}$, and g_i is the statistical weight.

In the case of the Stokes radiation, the initial state of the molecules may be the vibrational ground state, while for the emission of anti-stokes lines the molecules should have initial excitation energy. Due to the lower population density in these excited levels, the intensity of the anti-Stokes lines is lower by a factor:

$$\frac{I_{Stokes}}{I_{anti-Stokes}} = e^{(-\hbar \omega_n/kT)} \quad . \tag{2.18}$$

The scattering cross section depends on the matrix element of the polarizability tensor 2.15 and contains furthermore the ω^4 frequency dependence, and it can be written as follow [80]:

$$\sigma_R(i \rightarrow f) = \frac{8\pi \omega_S^4}{9\hbar c^4} \left| \sum_j \frac{\langle \alpha_{ij} \rangle \hat{e}_L \langle \alpha_{jf} \rangle \hat{e}_S}{(\omega_{ij} - \omega_L - i\gamma_j)} + \frac{\langle \alpha_{ji} \rangle \hat{e}_L \langle \alpha_{jf} \rangle \hat{e}_S}{(\omega_{jf} - \omega_L - i\gamma_j)} \right|^2 \quad , \tag{2.19}$$

where $\hat{e}_L$ and $\hat{e}_S$ are the unit vectors representing the polarization of the incident beam and the scattered light. The sum extends over all molecular levels j with homogeneous width γ_j accessible by single-photon transitions from the initial state i. We see from eq. 2.19 that the initial and the final states are connected by *two-photon* transitions which implies that both states have the same parity. For example, the vibrational transitions in homo-nuclear diatomic molecules, which are forbidden for single-photon infrared transition, are accessible to Raman transitions.

Raman scattering is a relatively weak process (typical cross section of 10^{-30}-10^{-25} $cm^2/molecule$). The number of photons Raman scattered is quite small. However there are several processes which can be used to enhance the sensitivity of a Raman measurement.

2.4   Raman techniques.

2.4.1   Resonance Raman scattering.

According to eq. 2.19 the Raman scattering cross section increases considerably if the laser frequency ω_L matches a transition frequency ω_{ij} of the molecule (**resonance Raman effect**) [81]. If the wavelength of the exciting laser is within the electronic spectrum of a molecule, the intensity of some Raman-active vibrations increases by a factor of $10^2 - 10^4$. This resonance enhancement or resonance Raman effect can be quite useful.

Metalloporphyrins, carotenoids and several other classes of biologically important molecules have strongly allowed electronic transitions in the visible. The spectrum of the chromophoric moiety is resonance enhanced and the one of the surrounding protein matrix is not. This allows the physical biochemist to probe the chromophoric site (often the active site) without spectral interference from the surrounding protein. The resonance Raman spectroscopy is also a major probe of the chemistry of fullerenes, polydiacetylenes and other "exotic" molecules which strongly absorb in the visible. Although many more molecules absorb in the ultraviolet, the high cost of lasers and optics for this spectral region have limited UV resonance Raman spectroscopy.

The vibrations whose Raman bands are resonance enhanced fall into two or three general classes. The most common case is Franck-Condon enhancement, in which a component of the normal coordinate of the vibration is in a direction along the molecule expands during an electronic excitation. The more the molecule expands along this axis when it absorbs light, the larger the enhancement factor. The easily visualized ring breathing (in-plane expansion) modes of porphyrins fall into this class. Vibrations which couple two electronic excited states are also resonance enhanced. This mechanism is called vibronic enhancement. In both cases enhancement factors roughly follow the intensities of the absorption spectrum.

Resonance enhancement does not begin at a sharply defined wavelength. In fact, enhancement of 5X-10X is commonly observed if the exciting laser is even within a few hundred wave numbers below the electronic transition of a molecule. This pre-resonance enhancement can be experimentally useful.
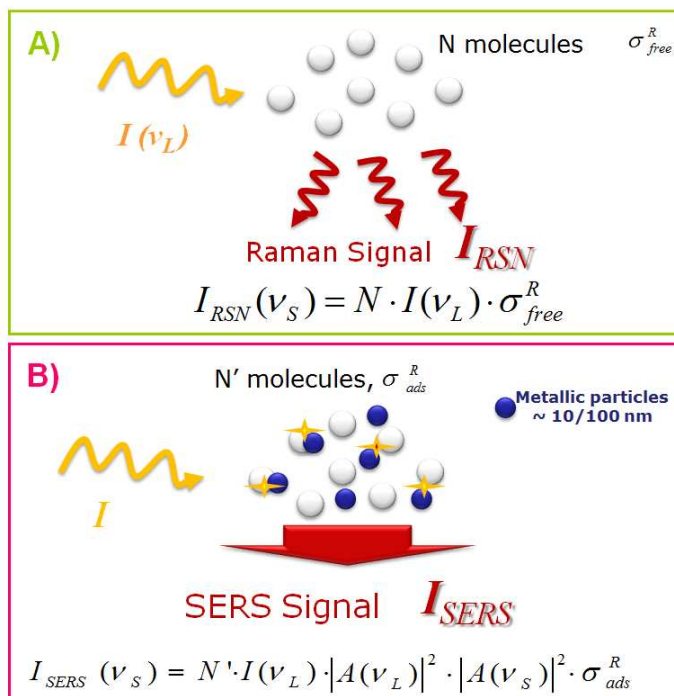
Figure 2.4: *Comparison of "normal" (top) and "surface-enhanced" (bottom) Raman scattering. For normal Raman scattering, the conversion of laser light I_L into Stokes scattered light I_{NRS} is proportional to the Raman cross section σ^R_{free}, the excitation laser intensity I_L, and the number of target molecules N in the probed volume. For "surface-enhanced": σ^R_{abs} describes the increased Raman cross section of the adsorbed molecule ("chemical" enhancement); $A(\nu_L)$ and $A(\nu_S)$ are the field enhancement factors at the laser and Stokes frequency, respectively; N' is the number of molecules involved in the SERS process.*

2.4.2   Surface Enhanced Raman scattering (SERS).

Surface Enhanced Raman scattering (SERS) [82] is a phenomenon which is observed when a molecule is absorbed onto, or is closed to a roughened metal surface. It was observed for the first time in 1974 [83], but only recently it has revealed to be effective to overcome the low-sensitivity problems inherent in Raman spectroscopy [84]. Within a few years, strongly enhanced Raman signals have been verified for many different molecules, which had been attached to the so-called "SERS-active substrates" [85, 86]. These SERS-active substrates are various metallic struc-

tures with sizes on the order of tens of nanometers. The most common types of
SERS-active substrates exhibiting the largest effects are colloidal silver or gold parti-
cles in the 10- 150 nm size range, silver or gold electrodes or evaporated films of these
metals (for a general overview on SERS, see refs [87,88]). It is generally agreed that
more than one effect contributes by many orders of magnitude to the observed total
enhancement. Figure 2.4 presents a schematic of "normal" and "surface-enhanced"
Raman scattering. In a normal Raman scattering, the total Stokes Raman signal I_{NRS}
is given by:

$$I_{NRS} = N\sigma^R_{free}I(\nu_L) \ , \tag{2.20}$$

i.e. it is proportional to the Raman cross section σ^R_{free}, the excitation laser inten-
sity $I(\nu_L)$, and the number of molecules N in the probed volume. Because of the
extremely small Raman cross sections, at least $\sim 10^8$ molecules are necessary to gen-
erate a measurable normal Raman scattering signal. In a SERS experiment (see Fig-
ure 2.4, bottom), the molecules are attached to a metallic nanostructure. The surface-
enhanced Stokes Raman signal I_{SERS} is:

$$I_{SERS} = N'\sigma^R_{ads}|A(\nu_L)|^2|A(\nu_S)|^2I(\nu_L) \ , \tag{2.21}$$

i.e. it is proportional to the Raman cross section of the adsorbed molecule σ^R_{ads}, the
excitation laser intensity $I(\nu_L)$, and the number of molecules which are involved in
the SERS process N'. N' can be smaller than the number of molecules in the probed
volume N.

The enhancement mechanisms are roughly divided into so-called "electromag-
netic" field enhancement and "chemical first-layer" effects [89]. Figure 2.5 shows a
simplified schematic diagram to understand the concept of electromagnetic SERS
enhancement. The metallic "nanostructure" is a small sphere with the complex di-
electric constant $\varepsilon(\nu)$ in a surrounding medium with a dielectric constant ε_0. The
diameter of the sphere ($2r$) is small compared to the wavelength of light (Rayleigh
limit). A molecule in the vicinity of the sphere (distance d) is exposed to a field EM,
which is the superposition of the incoming field E_0 and the field of a dipole E_{sp} in-
duced in the metal sphere. The field enhancement factor $A(\nu)$ is the ratio of the field
at the position of the molecule and the incoming field

$$A(\nu) = \frac{E_M}{E_0} \approx \frac{\varepsilon - \varepsilon_0}{\varepsilon + 2\varepsilon_0}\left(\frac{r}{r+d}\right)^3 \ . \tag{2.22}$$
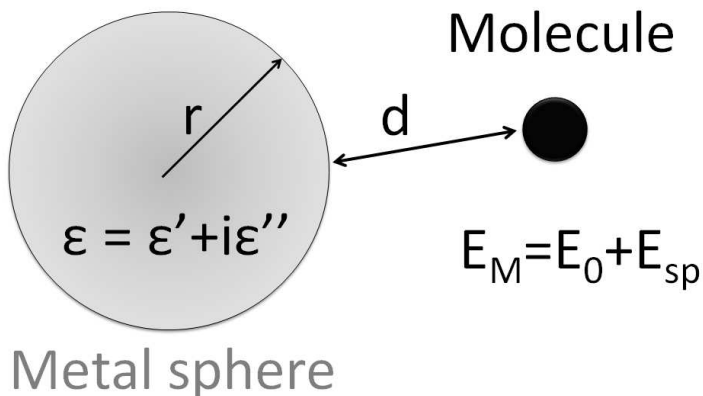
Figure 2.5: *Simple schematic diagram to understand the concept of electromagnetic SERS enhancement.*

$A(\nu)$ is particularly strong when the real part of $\varepsilon(\nu)$ is equal to $-2\varepsilon_0$. Additionally, for a strong electromagnetic enhancement, the imaginary part of the dielectric constant needs to be small. This conditions describe the resonant excitation of surface plasmons of the metal sphere. In such a way, the scattered Stokes or anti-Stokes field will be enhanced if it is in resonance with the surface plasmons of the metal sphere. Taking into account enhancing effects for the laser and the Stokes field, the electromagnetic enhancement factor for the Stokes signal power $G(\nu_S)$ can be written as

$$G(\nu_S) = |A(\nu_L)|^2 |A(\nu_S)|^2 \approx \left| \frac{\varepsilon(\nu_L) - \varepsilon_0}{\varepsilon(\nu_L) + 2\varepsilon_0} \right|^2 \left| \frac{\varepsilon(\nu_S) - \varepsilon_0}{\varepsilon(\nu_S) + 2\varepsilon_0} \right|^2 \left(\frac{r}{r+d} \right)^{12} . \quad (2.23)$$

This formula based on a very simple model already describes important properties and peculiarities of the electromagnetic SERS enhancement. It shows that the enhancement scales as the fourth power of the local field of the metallic nanostructure, and that it is particularly strong when excitation and scattered fields are in resonance with the surface plasmons. This is automatically the case of low-frequency Raman modes, and explains that the scattering powers of different Raman bands in a spectrum fall off with increasing vibrational energy. Electromagnetic SERS enhancement does not require direct contact between molecule and metal, but it strongly decreases with growing distance described by the decay of the field of a dipole over the dis-

tance $[1/d]^3$ to the fourth power, resulting in $[1/d]^{12}$. Maximum values of the electromagnetic enhancement for isolated single colloidal silver and gold spheroids are of the order of $10^6 - 10^7$ [90]. Theory predicts a stronger enhancement ($10^{11} - 10^{14}$) of electromagnetic fields for sharp features and large curvature regions, which may exist on silver and gold nanostructures [91].

In Figure 2.4 (bottom), chemical SERS enhancement is expressed as an increased Raman cross section σ_{ads}^R of the adsorbed molecule compared to the cross section in a normal Raman experiment σ_{free}^R. Possible electronic SERS mechanisms involve a resonance Raman effect due to a new metal-molecule charge-transfer electronic transition or a dynamic charge transfer between the metal and molecule, which can be described by the following four steps: (a) photon annihilation, excitation of an electron into a hot electron state, (b) transfer of the hot electron into the LUMO (Lowest Unoccupied Molecular Orbital) of the molecule, (c) transfer of the hot electron from the LUMO (with changed normal coordinates of some internal molecular vibrations) back to the metal, (d) return of the electron to its initial state and Stokes photon creation. "Roughness" seems to play an important role by providing pathways for the hot electrons to the molecule. The magnitude of chemical enhancement has been estimated to reach less than factors of 10-100.

2.5 Raman Tweezers

The Raman spectroscopy is one of the most powerful analytical techniques in physics, chemistry, biology and corresponding interdisciplinary branches of science [73, 92–94]. It is obvious that this technique may be applied when the sample to be analyzed is immobilized [3]. However, there is a large class of objects of micrometer sizes, in particular living cells (red blood cells, for instance) and aerosol particles, which need to be in a liquid or gaseous environment for their normal functionality. Brownian motion and motility (for some living cells), as well as fluxes in the surrounding medium, prohibit the direct use of the Raman analysis without combining it with an immobilization technique. One can use a pipette or apply known physical or chemical methods to immobilize living cell on planar surfaces. However, in many cases this may induce undesirable perturbations of chemical reactions in living cells. Chemical immobilization can change the chemical micro-environment of the living cell and may yield to other unknown effects. Surface effects become more important

as the size of the micro-object decreases, so it is crucial to protect the surface of a studied particle from any changes caused by the measurement procedures.

A very elegant approach to immobilize micro-sized samples in suspension consists of using radiation forces that an optical beam exerts on the studied sample (Optical Tweezers). The tight focus required by both micro-Raman spectroscopy and the optical trap makes combining the two techniques straightforward. The first communication on combining the two techniques was published in 1984 [95], when "a new Raman microprobe technique where micron-sized solid particles are trapped in stable optical potential wells using only the force of radiation pressure" was realized. The combination of Optical Tweezers with Raman Spectroscopy (Raman Tweezers) presents relevant advantages when characterizing objects in aqueous solution: a single, selected particle can be investigated free by surface interferences and in a regime where the Brownian motion is strongly reduced. As a matter of fact, it becomes possible to analyze the sample over time intervals of several hours [96] and to monitor its conformational changes caused by external agents or interaction with the environment [97, 98].The technique holds all the promise of Raman spectroscopy, including the potential to identify almost any biological molecule and disease [99], and adds to it both a greater level of control and analytical capability as well as the capability of observing a sample in its natural state [100]. As such, Raman Tweezers is likely to surpass Raman spectroscopy in use for biological analysis [12, 14, 17, 101].

Let us consider now the possible configurations of Raman Tweezers (RT) (figure 2.6). The simplest technique uses one microscope objective and one optical beam that at the same time traps a microparticle and excites its Raman spectra (figure 2.6(a)). This configuration has been widely exploited since the 1980s. Using two separate beams for trapping and Raman excitation (for example [102]) with a single objective has the advantage that the wavelength and the power of the trapping beam and the Raman beam can be adjusted independently to optimize the functionality (figure 2.6(b)). This technique also permits one to record resonant Raman spectra from a single trapped object. The size of the Raman beam and trapping beam may be varied independently with either an adjustable aperture or a telescope. The most universal Raman Tweezers systems use two separate beams for trapping and Raman excitation, and each of the beams is focused on the particle by a separate objective (figure 2.6(c)). Two counter-propagating optical beams can create a stable optical trap even with objectives with relatively small numerical apertures, because in this case the scattering
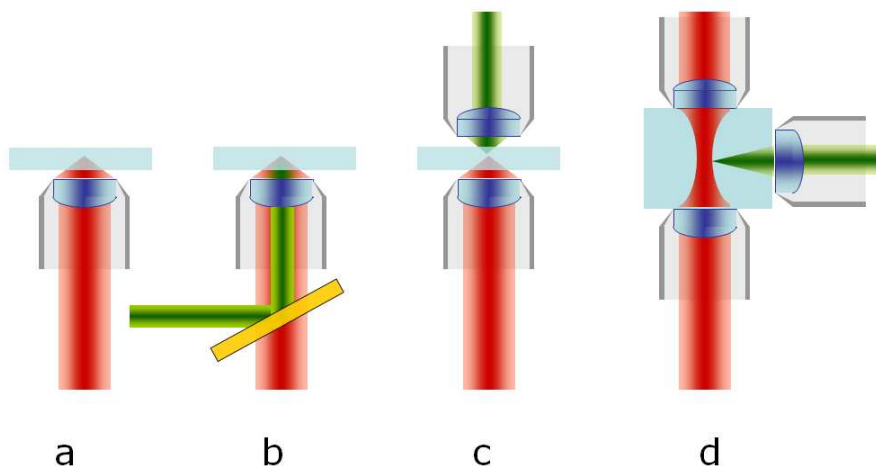
Figure 2.6: *Four main configurations of Raman Tweezers that are characterized by the propagation directions of the trapping beam(s) (red) and Raman excitation beam (green).*

radiation force of one beam is equal in value and opposite in sign to the scattering radiation force exerted by the second beam. Raman scattering is excited by a third beam focused on the trapped particle through an individual objective, which also collects Raman spectra (figure 2.6(d)). Recently, this variant of Raman Tweezers was realized in [103]. The dual-beam trap was created by two optical fibres and, due to their divergent light fields, offers the ability to hold and move large cellular objects with reduced prospects of photodamage.

2.6 Applications in Biology

One of the most promising and powerful applications of the Raman Tweezers is the study of single living cells [3, 16, 104, 105]. The biological cells contain complex mixtures of bio-molecules enclosed within the cell membranes. These bio-molecules

include the nucleic acid, the proteins, the polysaccharides and the lipids. Under-
standing various cellular processes requires identification of these molecules inside
the living cells. The Raman spectroscopy provides a convenient means of attain-
ing this information because of its ability to detect and identify molecules in a small
space. Valuable information about the composition, secondary structure and interac-
tions of DNA-protein complexes inside living cells can be attained from the position,
intensity and line width of the Raman peaks in the spectra. However, the Raman
spectra suffer from several drawbacks in studying single living cells, especially for
motile and floating cells in a liquid medium. This problem arises from the fact that
living cells may move away from the region of excitation because of Brownian diffu-
sion motion since relatively long acquisition times are required to obtain an adequate
Raman spectrum. The use of optical trapping can alleviate these problems and pro-
vide adequate time to acquire Raman spectra.

The first publication on using Raman Tweezers for living cells dates back to
2002 [10]. In their work, Ajito and Torimitsu, by combining the laser trapping tech-
nique with near-infrared Raman (NIR) spectroscopy, analyzed single cellular organelles
in the nanometer range. The samples were synaptosomes, nerve-ending particles
(about 500-700 nm in diameter) isolated from a neuron in a rat brain, dispersed in
the phosphate buffer solution. The NIR laser Raman trapping system trapped a sin-
gle synaptosome without photochemical damage and provided a Raman spectrum
of the sample with less fluorescence background.

In another study published almost simultaneously [8], Raman spectra of a single
yeast cells were obtained using low power trapping (2 mW) and high power Raman
excitation (20 mW during 5 s). The difference between the Raman spectra of living
and dead cells was demonstrated.

The first attempts to observe dynamical biochemical processes in optically trapped
living cells were made in [2, 11]. Real-time Raman spectra were recorded during a
heat-denaturation process, while the temperature of the surrounding medium was
increased.

Recently, it was demonstrated how a Raman Tweezers system may be used for
sorting cells and bacteria [15, 106, 107]. Furthermore, Xie et al. employed a Raman
Tweezers system to study cellular processes and for diagnosis of cellular disorders.
This kind of analysis is usually performed by comparing the relative intensity of the
different Raman features. To realize this issue, it is crucial to remove correctly the

background signal due to the environment. The problem of the background signal subtraction has been recently faced by Creely et al. [22]. They suggested to use a two-wavelength Raman Tweezers system, where a first laser is simultaneously used to trap a cell and to excite its Raman scattering, while a second laser is employed to move away the cell in order to acquire the reference spectrum.

In the next chapter, we introduce our experimental method which allows the acquisition of the Raman spectrum of a trapped object, free from any background contribution and which does not require any background subtraction procedure.

In many cases, determining where certain biochemical changes take place inside a cell may be just as desirable as learning when these changes occur. Raman images show the distribution of chemicals within a cell. Biomedical researchers who are familiar with imaging techniques can interpret these images more easily than spectra alone. In addition, such images contain more information than those obtained using conventional microscopy. However, in a single-beam trap a cell continues to move and rotate to a certain degree due to Brownian motion and organelle motility. During the acquisition time, one measures time-averaged Raman signals, but Raman imaging cannot be performed. A more stable configuration for trapping is realized by using multiple beams around the periphery of the cell [108]. This should not only allow to immobilize larger or asymmetric cells, but also distribute the trapping power more evenly throughout the volume, limiting the damage to the cell. Holographic Optical Tweezers (HOT) can be used to produce such multiple tweezing sites easily and rapidly and allow immobilization, manipulation or controlled rotation of trapped objects. To produce a Raman image using HOT the cell is trapped and scanned back and forth across the focus of the stationary excitation beam and in this way builds up an image of the entire cell, requiring no moving mechanical parts in the experiment. In this way a Raman image of a floating cell can be constructed [108].

2.7 Conclusion

The Raman spectroscopy has revealed a powerful tool for the microscopic analysis of organic and biological materials. When combined with the Optical Tweezers (Raman Tweezers), it allows investigating single, selected micrometric particles in their natural environment, therefore, reducing the unwanted interferences from the cover plate. A general problem affecting both the Raman spectrometers and the Ra-

man Tweezers systems is the background caused by the environment surrounding the sample under investigation. In next Chapter, I report on a novel method that allows acquiring Raman spectra of a single trapped particle free from any background contribution.

Part II

Method and Experimental Section

3

Raman Tweezers setup

For various single-cells experiments that will be presented in this thesis, we have built a Raman Tweezers setup. In this chapter, I will introduce this setup.

3.1 Introduction to the experimental setup

A sketch of the Raman Tweezers setup, assembled in the *Laser Spectroscopy and Optical Manipulation laboratory* of Prof. A. Sasso is shown in Figure 3.1. The system is essentially a homemade micro-Raman system (inverted configuration), equipped with a second laser for the trapping and manipulation of the sample [25, 26].
The combination of two laser beam, of different wavelength in the same microscope provides better sensitivity to a Raman Tweezers (RT) setup and helps to avoid incurring damage to biological sample [9]. The main advantage of this combined system is that an object in the trap can be kept stable for a long time. Thus it is possible to obtain the Raman spectrum of a living cell, selected out of a population, and study the biochemical processes occurring inside it for several hours.
To build the Raman Tweezers system three parts can be considered essentially: the
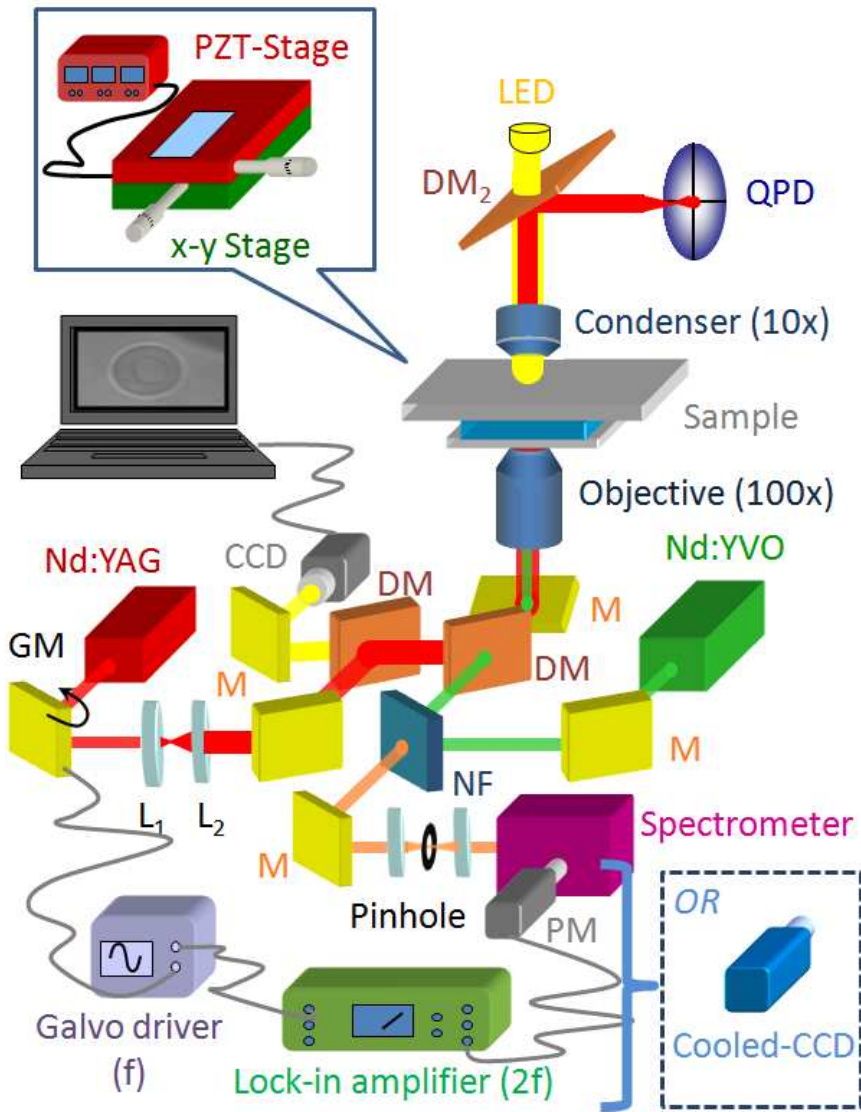
Figure 3.1: *Experimental setup of the combined Optical Tweezers and Raman Spectrometer: L, lens; M, mirror; DM, dichroic mirror; GM, galvomirror; NF, notch filter; PZT-stage, piezoelectric stage; QPD, quadrant photodiode.*

Raman spectrometer, the Optical Tweezers and the detection optics.
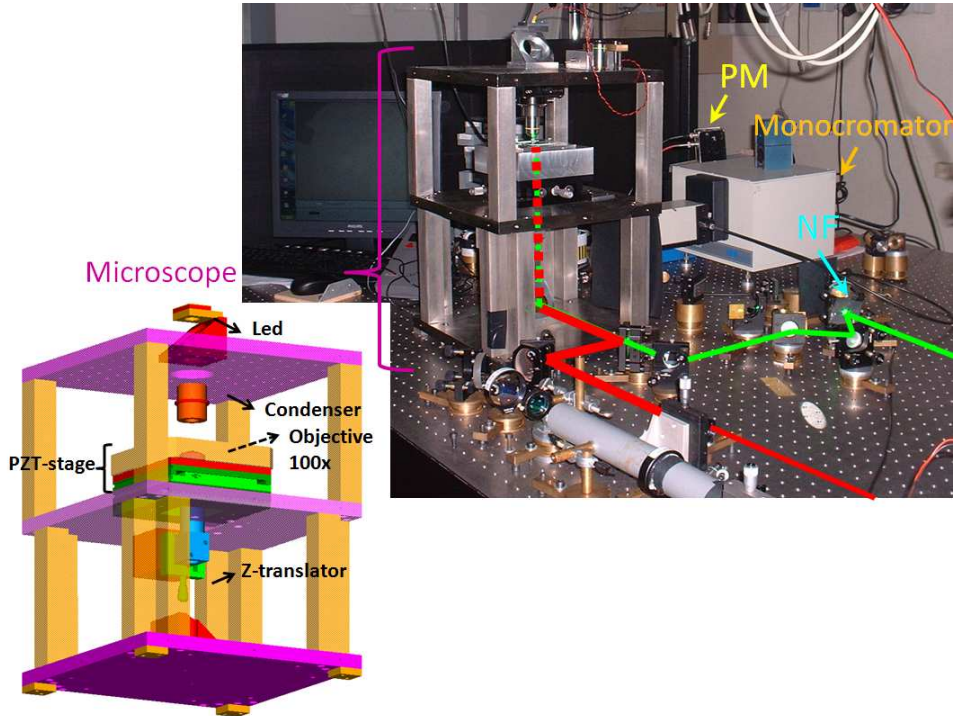
Figure 3.2: *Photograph of our Raman Tweezers system*

3.1.1 The Raman spectrometer
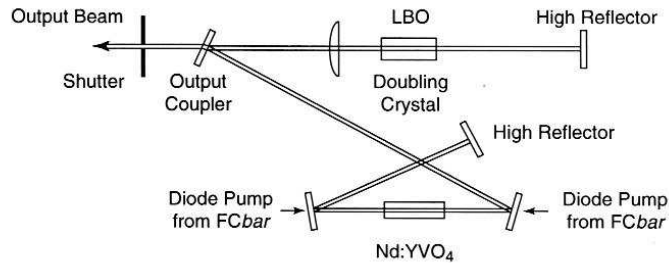
Figure 3.3: *Scheme of the Millennia XsJ laser head.*

The Raman probe is a frequency-doubled Nd-YVO laser (Millennia XsJ, Spectra Physics). The neodymium yttrium vanadate ($Nd : YVO_4$, Nd^{3+} ions doped in a yt-

trium vanadate crystalline matrix) laser crystal is the "driving engine" of the laser. The crystal is pumped by two 40 W fiber-coupled diode bar (FCbar) modules. The diode pump light is absorbed by the crystal and emitted as output at 1064 nm. This output radiation is resonated in the Millennia cavity and amplified through stimulated emission. The resulting 1064 nm light is converted to the visible ($\lambda = 532nm$) through frequency doubling or second harmonic generation in a lithium triborate nonlinear crystal (temperature-tuned LBO crystal), see Fig.3.3. The Millennia XsJ provides greater than 10 W of light, and exhibits extremely low noise performance with very high reliability, and a doubled beam that has a smooth intensity distribution and is near diffraction limited. Millennia XsJ Laser output characteristics are reported in Tab.3.1.

Table 3.1: *Millennia XsJ Laser output characteristics.*

Power	> 10 W
Wavelength	532 nm
Spatial Mode	TEM_{00}
Beam diameter at 1/e^2 points	2.3 mm
Bandwidth	< 10 GHz
Polarization	$>100{:}1$, vertical
Noise(10 Hz - 0.1 GHz)	$<0.08\%$ rms
Power stability	$\pm 1\%$

The radiation from the Raman laser is injected into an oil immersion 100X microscope objective (Olympus, $NA = 1.4$, infinity-corrected) through a dichroic mirror, reflecting near-IR radiation and being transparent to visible radiation. Scattered photons are collected by the same focusing objective; by going back along the incoming walk, this light passes through an holographic notch filter, which reflects the Rayleigh scattered radiation and transmits the Raman-shifted photons. The resulting filtered radiation passes through a pinhole (50 μm) and, finally, is focused onto the spectrometer entrance slit; this was a Jobin-Yvonne monochromator (TRIAX 180), equipped with a 1800 lines/mm grating (630-nm blaze wavelength). The photodetector is placed at the monochromator exit slit, set at an aperture of 50 μm.

The sample chamber is constituted by two 150 μm glass coverslips (Knittel Glasser, thickness no.1), sealed with parafilm stripes which also act as ~ 200 μm spacer (see
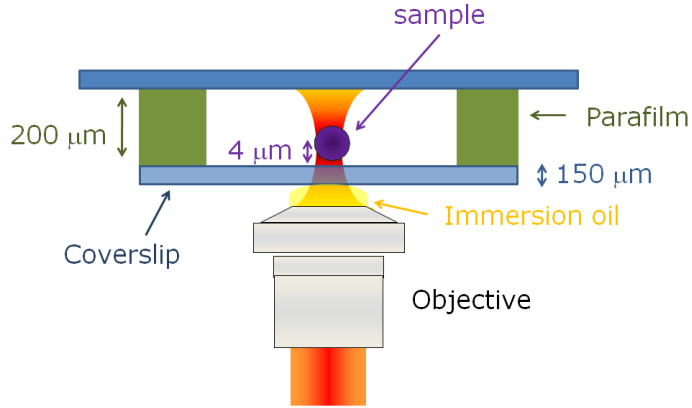
Figure 3.4: *Scheme of the sample holder.*

Fig.3.4). The chamber was mounted on a double translational stage: the first provides the coarse sample movement (micrometer translator Newport, HR-13, step size: 2 μm, travel: 13 mm), the second is a piezoelectric stage (Physik Instrumente I-517.3CL), with a nominal resolution of 2 nm.

The light from a green-filtered LED, focused on the sample by a 10X objective, is used to illuminate the sample; an image of the trapped cell is obtained by using a CCD camera, coupled to the microscope.

3.1.2 The Optical Tweezers

The trap laser beam is a Nd:YAG laser (Ventus, Laser Quantum), based on a YAG (yttrium aluminum garnet) crystal. This diode-pumped solid state laser emits light at $\lambda = 1.064\mu m$ with a maximum power of 3 W. Ventus Laser output characteristics are reported in Tab.3.2.

A telescope, formed by lenses L_1 ($f_1 = 10cm$) and L_2 ($f_2 = 30cm$) in Fig. 3.1, gives a linear magnification of:

$$M = \frac{f_2}{f_1} = 3 \tag{3.1}$$

Table 3.2: *Ventus Laser output characteristics.*

Power	3 W
Wavelength	1064 nm
Spatial Mode	TEM_{00}
Beam diameter at 1/e^2 points	2.5 mm
Bandwidth	< 80 GHz
Polarization	>200:1, horizontal
Noise(1 Hz - 0.1 GHz)	<1.5% rms
Power stability	±1%

As matter of fact, the laser beam diameter at the end of the telescope is around 10 mm, that allows overfilling of the objective input pupil and optimization of the trapping quality.
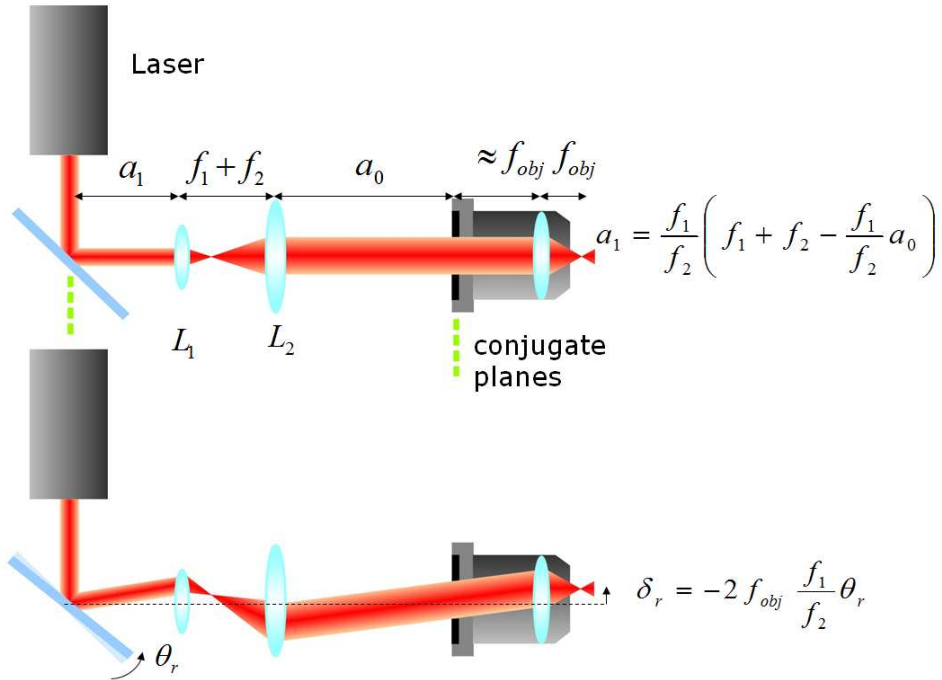
Figure 3.5: *Sketch of the experimental configuration of the spatial modulation of the optical trap position.*

Spatial modulation of the optical trap position is achieved by using a galvomirror (Cambridge Technology Inc., model 6220), driven by an external signal and placed at a distance from the telescope following the relation

$$a_1 = \frac{f_1}{f_2}\left(f_1 + f_2 - \frac{f_1}{f_2}a_0\right) \tag{3.2}$$

where a_0 is the distance between the objective pupil and lens L_2, see Fig. 3.5. According to ABCD law for Gaussian beam propagation, when Eq. 3.2 is satisfied, the objective pupil becomes a pivot point for the oscillating trap beam, so that a constant matching of the trap laser into the sample is achieved, whatever the incidence angle of the beam onto the objective input plane. When no signal is applied to the galvomirror, the trap beam is completely overlapped to the pump laser. As far as the voltage increases, the movement of the optical trap in the x-direction is given by:

$$\delta_r = -2f_{obj}\frac{f_1}{f_2}\theta_r \tag{3.3}$$

where θ_r denotes the tilting angle of the galvo-mirror.

3.1.3 The detection optics
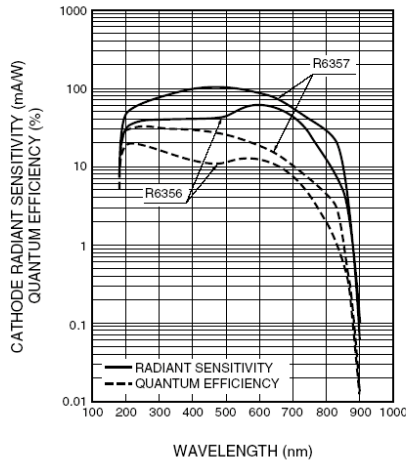
Figure 3.6: *Spectral response of Hamamatsu R6357 photomultiplier.*

The Raman radiation can be detected by using a photomultiplier (Phase-sensitive detection) or by using a cooled CCD camera.

 In phase-sensitive detection, the Raman radiation was revealed by exploiting a photomultiplier (Hamamatsu, model R6357), whose output signal is analyzed by using a lock-in amplifier. In such a case, the pinhole is not included. The photocathode material used in this photomultiplier is Multialkali (Na-K-Sb-Cs) and has a high, wide spectral response from UV to near-IR region. Figure 3.6 shows the spectral response of Hamamatsu, R6357 photomultiplier. The photomultiplier is placed at the monochromator exit slit, set at an aperture of 50 μm. A complete Raman spectrum of the trapped object is achieved by scanning the radiation wavelength coupled onto the output slit, by a micro-controlled grating rotation.
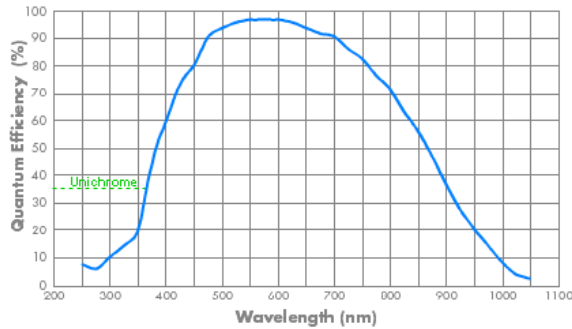
Figure 3.7: *Spectral response of Pixis CCD camera.*

 The inelastically scattered photons can be alternatively detected by using a front-illuminated charge-coupled device (Pixis 1024, Princeton Instruments, 1024x1024 pixels), thermoelectrically cooled at -70 ^oC and placed at the spectrometer exit. Thanks to the cooling technology, PIXIS cameras offer extremely low dark current. In Figure 3.7 it is reported the spectral response of Pixis CCD. The detector was interfaced to a personal computer, where spectra were stored and analyzed.

 The experimental setup was also completed by the position detector to measure the relative motion of the trapped bead within the trap. The trapping light, in fact, is reflected by dichroic mirror DM_2 and detected by the quadrant photodiode (QPD) placed in the condenser back focal plane, see Fig. 3.1.

3.2 Sample preparation

After building of Raman Tweezers set-up, in order to test and characterize the system we used polystyrene latex beads (SERVA Electrophoresis).
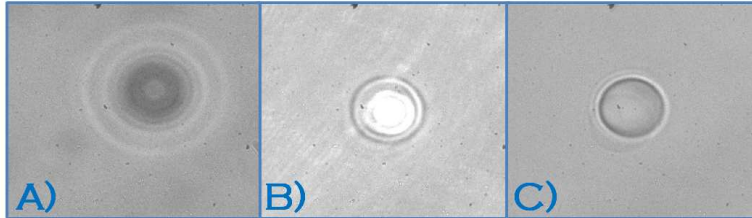
Figure 3.8: *A): a floating polystyrene bead of 4.25 μm. The particle is out of focus. B) The same bead trapped about 4 μm above the coverslip. The filter for trapping radiation is excluded. C) The same trapped polystyrene bead when the filter is put in.*

To start with, a polystyrene beads (4.25 μm-sized) was trapped and its Raman spectra recorded in real time for the alignment of the system (see Fig. 3.8). Polystyrene beads were diluted in distilled water (the pipette tips used for making the solutions were sterile). Few microliters of this solution were transferred in the home-made chamber.

Figure 3.9: *A trapped red blood cell: the RBC reaches a trapped position and floats slightly around it.*

Red Blood Cells (RBCs) were, instead, used as model biological organism in the Raman Tweezers experiments. Fresh blood was obtained by fingerprint needle prick from several voluntary donors. A drop of blood was then diluted in a physiological solution such that a single red blood cell (RBC) could be trapped without interference from other cells in the surrounding (see Fig. 3.9). In particular, blood

samples were prepared according to the following procedure: blood (5 μl) antico-agulated by K-EDTA, was diluted in 10 ml of isotonic aqueous NaCl solution and 0.5 ml of human albumin (used as membrane protection). The used thalassemic cells (α and β) were kindly provided by the consenting patients of Prof. B. Rotoli (Department of Biotechnology and Biomedicine of University of Naples "Federico II"). All β-thalassemic donors (n=6) showed typical pathological features such as re-duced MCV (red cell mean corpuscular volume) and elevated HbA2 electrophoresis fraction; serum ferritin was normal in all of them. Only one patient affected by α-thalassemia was treated. In fact, this kind of thalassemia is quite rare. Main blood parameters of α-thalassemia donor were: Hb 12.5 g/dl, RBC 4.600.000/ μL, MCV 83.7 fl, MCH 27.2 pg, MCHC 32.5 %, RDW-SD 39.1; Hb electrophoresis was normal and an alpha-thalassemia genomic pattern was found at molecular level $\alpha\alpha/\alpha-$;

4

Method and data analysis

In this chapter, I will describe Raman measurement methods based on standard confocal and "phase-sensitive" techniques. In addition, data processing and analysis will be also shown.

4.1   Standard confocal Raman microscopy

A widely used method to subtract the background contribution in Raman Tweezers experiments is based on *confocal microscopy* [109].

Confocal microscopy is a standard optical technique used to increase micrograph contrast and/or to reconstruct three-dimensional images by using a spatial pinhole to eliminate out-of-focus light or flare in specimens [110]. In fact, the pinhole aperture placed between the microscope objective and the image plane rejects the residual scattered rays originated from any out-of-focus points on the sample and functions as a spatial filter (see Figure 4.1). Confocal microscopy offers several advantages over conventional widefield optical microscopy, including the ability to control depth of field, elimination or reduction of background information away from the focal plane (that would lead to image degradation), and the capability to collect serial optical
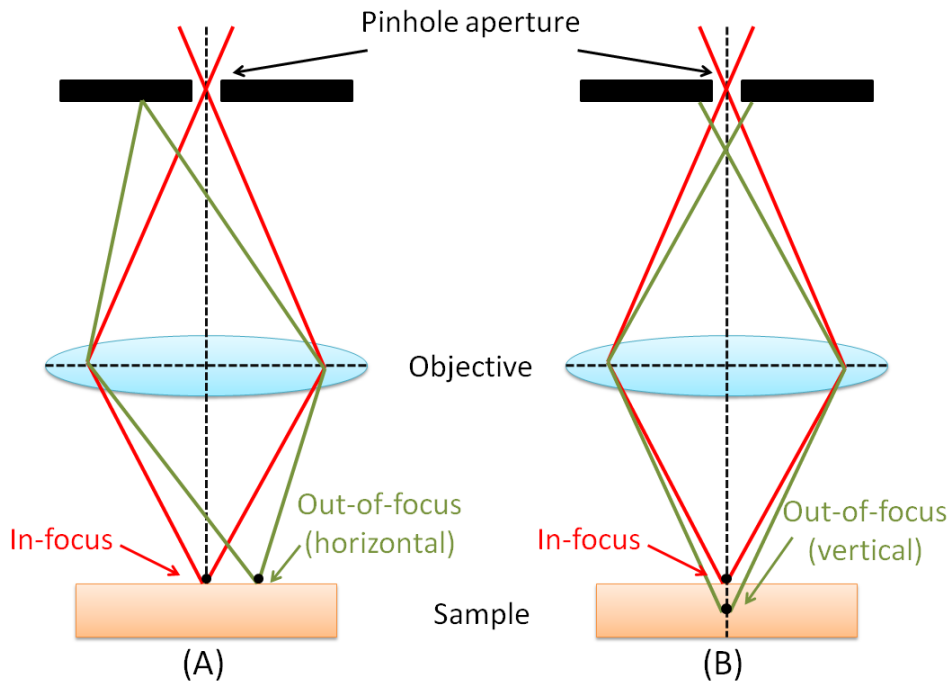
Figure 4.1: *Spatial filtering with the pinhole aperture of the horizontal (A) and vertical (B) out-of-focus rays.*

sections from thick specimens.

As with conventional microscopy, confocal microscopy has inherent resolution limitations due to diffraction. In particular it is assumed that the point source used produces a point of light on the specimen. In fact it appears in the focal plane as an Airy disk, whose size depends on the wavelength of the light source and the numerical aperture of the objective lens [111].

The optical resolution of a lens is determined by the size of the inner dark ring of its Airy disk. The diameter of the inner ring is related to the aperture of the lens. The smaller the aperture, the larger the Point Spread Function and the bigger the inner ring, thus the lower its optical resolution [112]. When single point resolution is concerned, the diameter of the inner ring, as shown in the figure 4.2, is used to define the resolution, thus called resolution element:

$$d_{airy} = \frac{1.22\lambda}{NA} \cdot M \cdot 3.6 \ , \tag{4.1}$$
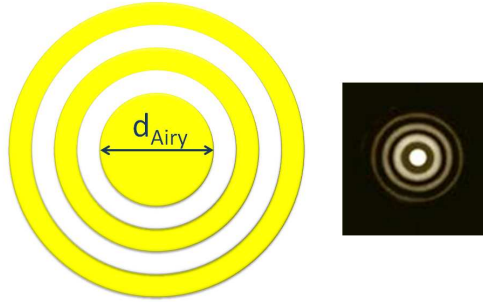
Figure 4.2: *The distribution pattern looks like a disc with a central high intensity spot and many concentric rings, a pattern called Airy disc. Airy pattern describes the light intensity distribution as a function of distance from the optical axis.*

where λ is the wavelength of emitted light (*532 nm*), NA is the objective numerical aperture (*1.4*) and M is the objective magnification (*100*).

When point-to-point resolution is concerned, the resolution is defined as the distance of the two points where the maximum of one point is just above the first minimum of the second point (Rayleigh criterion). The standard formula used for the lateral resolution, that is found in many optics and microscopy textbooks [113] is:

$$R_{lat} = \frac{0.61\lambda}{NA} \quad . \tag{4.2}$$

In our case, the expected lateral resolution is $R_{lat} = 0.23\mu m$. In confocal microscopy, due to its improved contrast, there is a slight gain in resolution but it is still diffraction limited. When pinhole has typical dimension < 0.25 Airy Unit, lateral resolution is calculated by:

$$R_{lat} = \frac{0.37\lambda}{NA} \quad . \tag{4.3}$$

By comparing eq. 4.2 with eq. 4.3, you can see that, in theory, a confocal system provides higher resolution than conventional system. It comes from the ratio of (*0.61/0.37*), roughly, about *1.6* times of conventional system. When pinhole is between *0.25-1* Airy Unit, a value between *0.37-0.61* is used to replace *0.37* in the formula 4.3.

The resolution formula 4.3 is useful for assessing resolution in the image plane, but not along the optical axis (z-axis) of the microscope, information that is critical to successful analysis by the deconvolution technique. Therefore, the axial Rayleigh criterion can be defined by taking the distance from the point of maximum intensity to the first point of minimum intensity of the central bright region along the z-axis. This value can be estimated using the following formula:

$$R_{axial} = \frac{2\lambda\eta}{(NA)^2} \quad , \tag{4.4}$$

where η is the refractive index of the medium between the objective and the sample ($\eta = 1.515$ for immersion oil and glass). In our case, the expected axial resolution is $R_{axial} = 0.82\mu m$. When pinhole is close to zero (typical dimension < 0.25 Airy Unit), the formula 4.4 can be replaced by [114]:

$$R_{axial} = \sqrt{\left(\frac{0.64\lambda}{\eta - \sqrt{\eta^2 - (NA)^2}}\right)^2 + \left(\frac{\sqrt{2}\eta PH}{NA}\right)^2} \quad , \tag{4.5}$$

where *PH* is the pinhole diameter (in Airy Units) divided by the magnification factor. When pinhole is between *0.25-1* Airy Unit, a value between *0.64-0.88* is used to replace *0.64* in the formula 4.5.

A practical demonstration of the micrograph contrast increase obtained by using a confocal microscope is shown in Fig. 4.3. Presented in Fig. 4.3 are the axial intensity distributions for a typical widefield (Figure 4.3(a)) and confocal (Figure 4.3(b)) fluorescence microscope. Note the dramatic reduction in intensity of the "wings" in the confocal distribution as a function of distance from the central maximum.
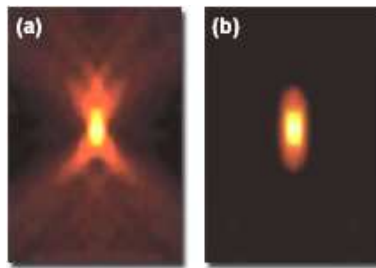
Figure 4.3: *The axial intensity distributions of a typical widefield (a) and confocal (b) fluorescence microscope.*

It is tempting to assume that making the pinhole as small as possible is the best choice. However, as the pinhole size is reduced, so it is the rate of photons that arrive at the detector from the specimen. This may lead to a reduced signal-to-noise ratio. To offset the weaker signal, more Raman scattering is needed from the specimen. This usually can be done by raising the intensity of the excitation light. But high intensities can damage the specimen. Moreover, it has been shown that optical sectioning does not improve considerably with the pinhole size below a limit that approximates the radius of the first zero of the Airy disk.

In our case the pinhole dimension is set to *50 μm* (*0.33* Airy Unit), and the expected axial and lateral resolution are:

$$R_{axial} = 0.57 \mu m \ , \tag{4.6}$$

$$R_{lat} = 0.18 \mu m \ . \tag{4.7}$$

The experimental results can deviate from the theoretical values, in such a case it becomes necessary to subtract the background contribution in Raman Tweezers experiments. A widespread method used to subtract the background is based on the acquisition of two spectra. In the first one, the sample is placed in the focus of the pump laser, in order to achieve the maximum excitation intensity. The sample is successively removed and the "blank" spectrum acquired. The final data are obtained by the background subtraction procedure [22, 115].

In particular, we have used this background-subtraction criterion to acquire the Raman spectrum of a trapped 4.25-μm-diameter polystyrene bead in aqueous solution. Off-line subtraction of these two spectra sometimes fails in giving the correct background-free signal, as will be widely illustrated in the next Chapter. To overcome this drawback, we have developed a new experimental method which allows the acquisition of the Raman spectrum of a trapped object, free from any background contribution and which does not require any background subtraction procedure [25].

4.2 Phase-sensitive method

As mentioned above, in ref. [25, 26] we demonstrated the possibility of getting Raman spectra of single optically trapped microparticles in the absence of background noise. Here, I briefly resume the basic idea of this method-denominated

phase-sensitive. It is based on the use of two collinear and copropagating laser beams: the first is devoted to trapping (trap laser), while a second one is used to excite the Raman transitions (pump laser). The trap laser periodically moves the trapped particle back and forth across the pump laser. The trap laser power is much stronger than the pump laser, so that the photonic force of the pump beam does not interfere with the harmonic oscillation of the trapped object. The back-scattered photons are detected by a photomultiplier, whose output signal is analyzed by using a lock-in amplifier.
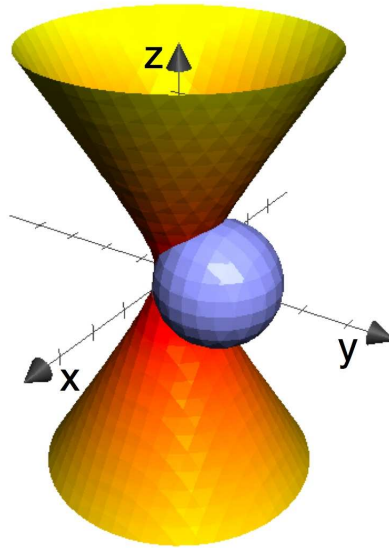
Figure 4.4: *Sketch of the experimental configuration of the phase-sensitive detection method. Z is the propagation axis of both pump and trap laser beams. The bead moves sinusoidally along the y-axis, crossing periodically the pump laser. The trap laser, used to move the bead, is not shown in this figure.*

The oscillation geometry is sketched in Figure 4.4, in which the sample is a dielectric bead of radius a placed close to the focal region of the pump laser. For the sake of clarity, the trap laser is not shown. The coordinate axis origin center O is placed at the beam-waist center. In a paraxial Gaussian beam description, the pump laser intensity is given by

$$I(r, z) = \left(\frac{2P}{\pi w(z)} \right) exp \left(- \frac{x^2 + y^2}{w^2(z)} \right) \quad , \tag{4.8}$$

where P is the laser power and $w(z)$ is the spot size given by

$$w(z) = w_0 \left[1 + \left(\frac{z}{z_0} \right)^2 \right]^{1/2} . \tag{4.9}$$

In the previous relation, w_0 is the diameter of the laser section at its beam waist and $z_0 = \pi w_0^2 / \lambda$ is the Rayleigh length (λ is the pump laser wavelength). In order to describe the Raman signal formation, we have developed a method based on a standard Monte Carlo simulation (see Appendix). By using it, we have calculated the time-dependent scattering signal from the trapped sample and from the solvent in which it is placed. The simulation assumes that the Raman signal is proportional to the illuminated part of the bead; each irradiated point of the bead is weighed by the pump laser profile given by eq. 4.8. Let us consider that the bead oscillates at a given frequency f along the y-axis following the law

$$y(t) = A \sin(2\pi f t) , \tag{4.10}$$

where A is the modulation amplitude.

When the bead oscillates across the pump laser, the Raman signal is also modulated. Figure 4.5-(a) reports the bead position as a function of time while Figure 4.5-(b) illustrates the behavior of the generated Raman signal (S_{Raman}). In particular, it is easy to understand that when the pump and the trap beams are completely overlapped (positions 1 and 3) S_{Raman} is maximum; on the contrary, it reaches a minimum when the modulation amplitude is A and $-A$ (positions 2 and 4). During each oscillation, the bead crosses the pump laser twice so that S_{Raman} results modulated at frequency $2f$. The peak-to-peak value of the oscillation appearing in Figure 4.5-(b) represents the phase-sensitive signal as processed by a lock-in amplifier. Finally, we report in Figure 4.5-(c) the Raman signal produced by the solvent (water in our case) where the bead is immersed (in our analysis the Raman cross section of solvent and bead are assumed equal). The solvent Raman signal increases when the bead moves away from the pump laser beam waist. Following the whole oscillation, it is found that the solvent Raman signal is 90° shifted with respect to that relative to the bead. This means that a phase-sensitive detection allows discrimination of the two Raman signals. In Figure 4.6, we report the behavior of S_{Raman} generated again by the Monte Carlo obtained in the same condition of Figure 4.5, but varying the modulation amplitude A between 0.4 and 2 μm.
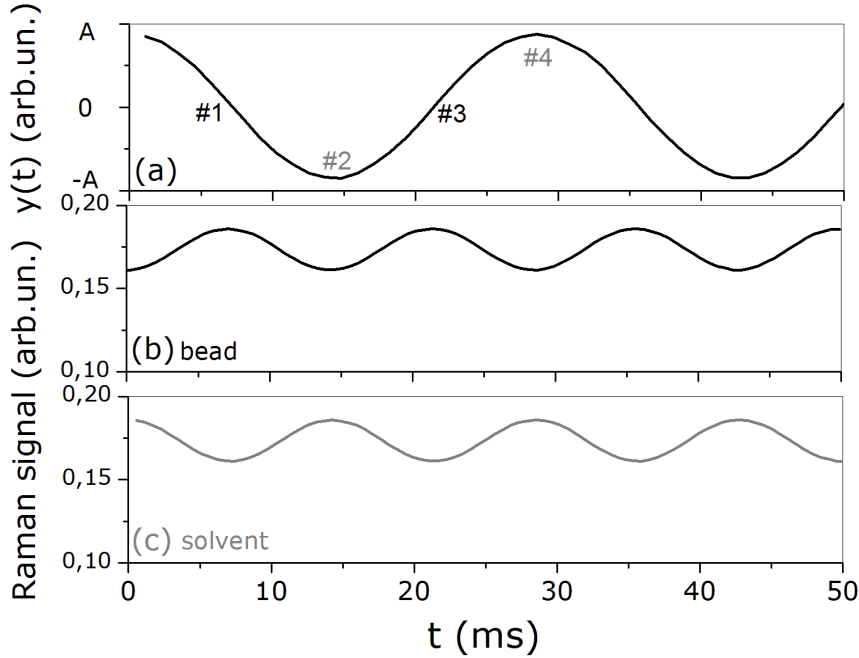
Figure 4.5: *(a) Bead position, as function of the time. Modulation frequency has been fixed at 33 Hz. (b) Raman signal originated by the trapped object. The reported values have been obtained by a Monte Carlo numerical simulation, calculated using the program Mathlab framework for a $1\mu m$-diameter bead crossing the Gaussian pump laser with a waist of 0.53 μm. (c) Calculated intensity of the Raman signal produced by the solvent volume periodically occupied by the bead.*

   As can be seen, the peak-to-peak value increases as A increases but it reaches a saturation for large modulation amplitude. For such values, the bead oscillates between two limit regions far away from the beam waist ($A > w_0$), and the maximum contrast is achieved.

   The main advantages of the trapping modulation method can be summarized as follows.

1. Background photons originated by the solvent surrounding the trapped particle, such as Raman and fluorescence scattering, are completely suppressed, including those coming from the volume occupying the particle, being 90° phase-shifted.
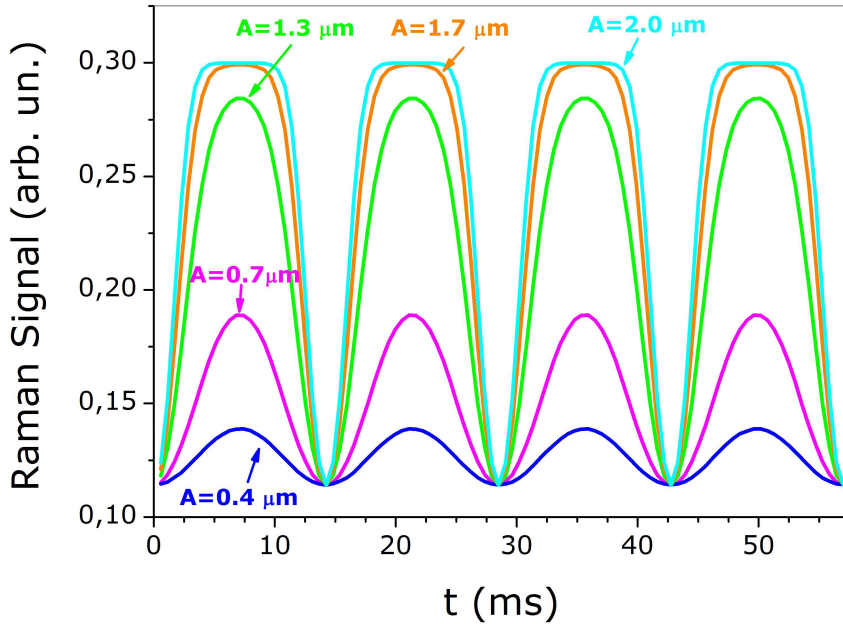
Figure 4.6: *Calculated Raman signal of a trapped bead as a function of the time obtained for modulation amplitudes ranging between 0.4 and 2.0 μm.*

2. Spurious stray-light contribution from the coverslip, not being modulated, is also suppressed by the lock-in filter. This avoids the use of a second Notch filter (normally present in micro- Raman systems).

3. The method is also suitable to investigate Raman response of the medium surrounding the trapped particle. Therefore, it is possible to scan the Raman pattern of the medium by translating the bead. From this point of view, the method exhibits an intrinsic spatial resolution that is comparable with confocal microscopy. The estimated spatial resolution is of the order of the bead volume, that is, a few femtoliters.

4. The particle under investigation is illuminated by the pump beam only for a short time, corresponding to the transit time across the pump laser waist. In this way, sample photodamage can be reduced.

It is interesting to note that the trapped bead could be set in oscillation considering

other different geometries. For instance, the centers of the trap and pump beams can be slightly translated from each other by a distance of the order of their spot sizes; in such way, two independent optical traps are created. By modulating the trap laser at a frequency f, the bead jumps periodically from one trap to the other one. In this case, S_{Raman} results modulated at the same frequency f. Holographic multitraps created by spatial light modulators could be another alternative to produce such oscillations [116].

4.3   Data processing and analysis

The Raman spectrum of the trapped object can be achieved by scanning the radiation wavelength coupled onto the output slit, by a micro-controlled grating rotation and collected by using the Photomultiplier. The obtained spectrum is displayed directly on the oscilloscope, saved as ASCII file and analyzed by using Origin 7.0 software.

The Raman spectrum of the trapped particle can be alternatively acquired by using the CCD camera (Pixis 1024). In this case, the standard software interface WinSpec is used to control and acquire data from CCD camera. After data acquisition halting, the image reported in Fig. 4.7 is displayed. Finally, the collected data are saved as ASCII files and analyzed by using the same Origin 7.0 software.

Figure 4.7: *Raman spectrum of a trapped polystyrene bead of 4.25 μm acquired by using the CCD camera and visualized using the WinSpec software. The power of the Raman probe on the sample is 2 mW, the acquisition time is set to 20 s with 1 accumulation.*

The Raman spectrum of the trapped polystyrene bead was used to precisely assign a wavenumber to each individual detector pixel. In fact, the polystyrene Raman
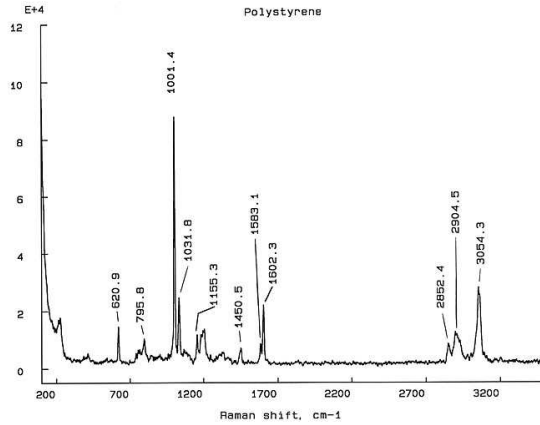
Figure 4.8: *Raman spectrum of polystyrene from McCreery group [117].*

spectrum is well known. In particular, there is an extensive collection of over 1000 Raman spectra compiled by Professor Richard L. McCreery's research group at The Ohio State University [117]. The spectra cover a wide range of compounds including polystyrene, see Fig. 4.8. For a typical experiment, the surface of the coverslip was first located by detecting the focus spot of the laser beam reflected from the surface of the glass coverslip [118]. Then the objective was moved at a height of 4 μm above the coverslip. At this distance, the optical aberrations are reduced and the Raman collection efficiency is maximized [26]. Finally, a polystyrene bead of 4.25 μm was trapped. Spectra were recorded each for 20 s exposure time. As shown in Fig. 4.9, calibration points distributed over the whole spectral region of interest were fitted by a straight line. In this way, the pixels were converted to the appropriate relative cm^{-1} values. The final spectral resolution was 2 cm^{-1}, as estimated from the polystyrene spectrum by measuring the FWHM of the 1001.4 cm^{-1} peak. In Fig. 4.10 is reported the Raman spectrum from a trapped polystyrene bead which was used for wavelength calibration of the system acquired by using the CCD camera.
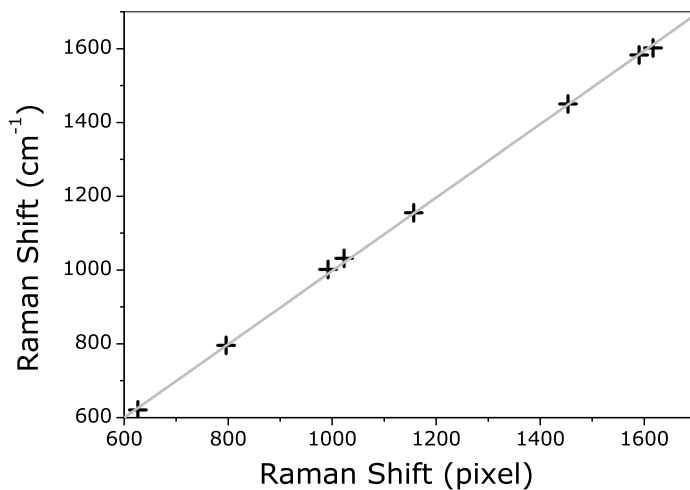
Figure 4.9: *Raman peaks position in pixel as a function of the wavenumber values [117]. A linear fit of the experimental data is also shown.*
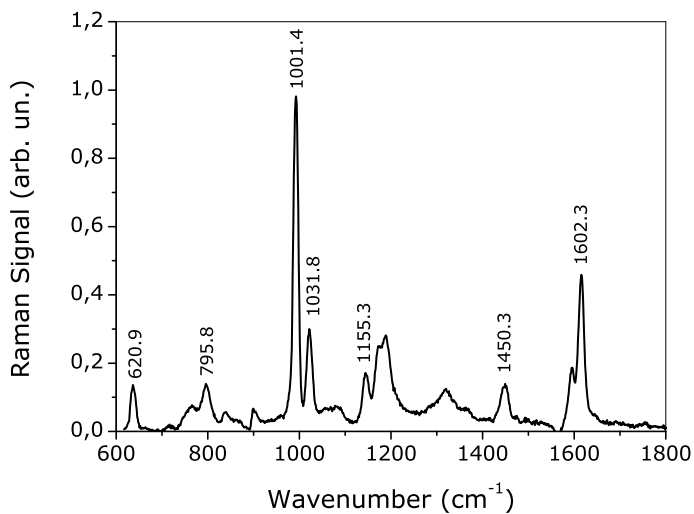
Figure 4.10: *Calibrated Raman spectrum from a trapped polystyrene bead. The acquisition time is 20 s. Laser power on the sample is 2 mW.*

Part III

Results and Discussion

5

Phase-sensitive detection: results

The purpose of the present chapter is to give a detailed description of the phase-sensitive method and to supply a systematic study concerning the formation of the Raman signal. In this chapter, I will show the dependence of the Raman signal of a trapped polystyrene bead on several parameters, such as the height from the coverslip surface, the bead size, the modulation amplitude, and the pump laser intensity. The obtained results establish a direct and practical approach for background suppression in the spectroscopic analysis of optical trapped microsized samples.

5.1 Introduction

Background noise due to the environment can represent a serious obstacle for Raman spectroscopic analysis, even in single-particle experiments. The main contributions to this signal are as follows:

1. the fluorescence of the solvent in which the trapped particles are immersed;

2. the fluorescence from the medium used for index matching between the micro-
   scope objective and the specimen;

3. the fluorescence from the coverslip itself;

4. the stray light of the pump laser, which is not completely suppressed by optical
   filters (Notch filters).

Generally, the use of near-IR lasers as pump laser can help to reduce the fluorescence
component, minimizing, at the same time, sample photodamage. Nevertheless, it
is possible to find many practical experimental situations in which the inelastic as
well as elastic scattering from the solvent can severely affect the reliability and re-
producibility of the measurements. This happens, for instance, when the solvent has
strong Raman-active bands that spectrally overlap with the sample Raman features.
In this case, reasonable but often distorted spectra are created using, either manual
or automatic, subtraction procedures [23]. This drawback is particularly important
when Raman spectroscopy is used to monitor the health state of single microorgan-
ism. In fact, the diagnosis of cellular disorders is often performed by monitoring the
relative intensities of selected Raman peaks; therefore, high accuracy in subtracting
the solvent contribution is required [2, 24]. The background subtraction is also crit-
ical when studying the diffusion of molecules into microsized particles, especially
for living organisms. This is a challenging issue in both biology and medicine, hav-
ing interesting applications related to the drug delivery problem. Recently, Bridges
et al. [119] investigated the penetration of solvents (acetonitrile) into a 75-μm-sized
polystyrene bead by using a confocal Raman system. The necessary spatial resolu-
tion was given, in that case, by the confocal configuration itself; in particular, the
authors estimated that more than 90% of the observed signal arises within a distance
from the focal plane of the order of the pump laser wavelength.

    During this thesis work, it has been demonstrated a new technique to acquire
Raman spectra of optically trapped particles [25, 26]. Our method presents two im-
portant advantages. First, Raman spectra do not require any background subtrac-
tion. In particular, both scattering and fluorescence from the solvent and spurious
stray light are completely suppressed thanks to a phase-sensitive detection scheme.
Therefore, only scattered photons coming from the trapped particle contribute to the
final Raman spectrum. The present chapter is focused on a full characterization of

this method. We supply a systematic study of the formation of the Raman signal and its dependence on several parameters, such as the height from the coverslip surface, the size of the bead, the amplitude of the spatial modulation of the trapped particle, and the pump laser intensity. The benefits of the application of phase-sensitive detection are explored. In addition, a model based on a Monte Carlo simulation provides theoretical estimation of the Raman signals, which are successfully compared with our experimental results.

5.2 Standard confocal microscopy and background-subtraction procedure

A widely employed method to subtract the background contribution in Raman Tweezers experiments is based on the acquisition of two spectra [22, 24, 120]. In the first one, the sample is placed in the focus of the pump laser, in order to achieve the maximum excitation intensity. The sample is successively removed and the "blank" spectrum acquired. Off-line subtraction of these two spectra gives the correct background-free signal. In particular, Creely *et al.* [22] recently suggested to use a two-wavelength RT system, where a first laser is simultaneously used to trap a cell and to excite its Raman scattering, while a second laser is employed to move away the cell in order to acquire the reference spectrum. As a matter of fact, this background acquisition procedure is based on two basic assumptions:

1. the scattering contribution coming from the solvent volume previously occupied by the cell (V_{cell}) is negligible;

2. no significant variation of the cell micro-environment occurs in the time interval between the acquisition of the two spectra.

Although the second assumption may be true for most practical applications, the first one may be not satisfied in several cases. Indeed, despite V_{cell} is usually smaller than the whole solvent volume irradiated by the Raman probe, it gives rise to a large number of scattered photons, since it is placed in the laser focus. These issues become particularly relevant in the investigation of cells in physiological solutions in the presence of nutritional supplements: in fact, amino acids in solution can exhibit many common Raman peaks with the cell itself.

To test this drawback, we used this background-subtraction criterion to acquire the Raman spectrum of a trapped 4.25-μm-diameter polystyrene bead in aqueous solution. To the purpose, the Raman signal passed through a pinhole (50 μm) and was detected by using a cooled CCD camera. This approach will be hereafter indicated as *standard confocal technique*.

In the spectral region chosen for this test (2700-4000 cm^{-1}), there are two prominent peaks, corresponding to C-H bond stretching sp^3 (2900 cm^{-1}) and sp^2 (3055 cm^{-1}) of the polystyrene polymer. In addition, two broad Raman peaks, corresponding to the symmetric (3420 cm^{-1}) and asymmetric (3630 cm^{-1}) water vibrational stretching lie in this region; the intensity of these peaks is comparable to that corresponding to polystyrene, giving rise to a quite strong background contribution.
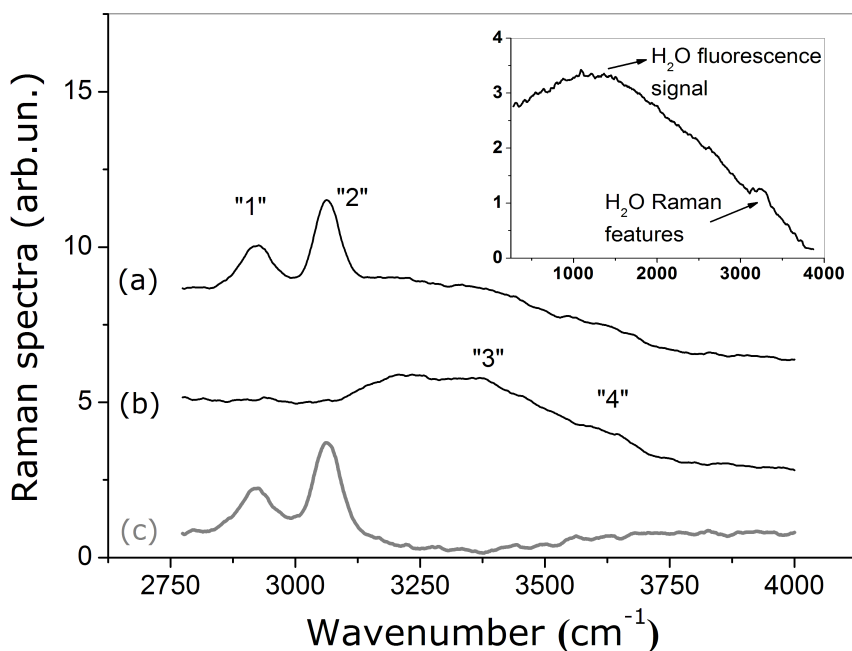
Figure 5.1: *(a): Raman signal of the trapped bead, as acquired by using the standard confocal method. The peaks 1 and 2 are due to polystyrene, while peaks 3 and 4 to water. (b): Reference spectrum. The features are due to water scattering contribution. (c): Difference between trace (a) and (b). The estimated resolution of all the spectra is 6 cm^{-1}. In the inset the reference spectrum has been shown in the range between 300 and 4000 cm^{-1}, where the water fluorescence contribution is clearly evident.*

In Fig. 5.1, curve (a), we report the Raman spectrum of the trapped bead recorded by using the CCD camera. The acquisition time is 20 s. The power of the trapping beam impinging on the sample is around 30 mW, while the Raman laser power is only 0.5 mW. The bead was trapped at a distance of 4 μm from the coverslip. The background contribution is ascribed to the solvent fluorescent contribution and to residual laser wing (see inset of Figure 5.1, where we show a bead-free Raman spectrum recorded over a wide spectral range). We removed the particle to record the control spectrum. The result is shown in Fig. 5.1,(b). The final background-subtracted spectrum is reported in Fig. 5.1,(c). As it can be seen, the difference spectrum is still affected by a not-flat background (see depression between 3100 and 3500 cm^{-1}). This is consistent with the fact that the scattering contribution arising from the water volume previously occupied by the bead is not negligible. Spectrum distortions due to solvent contribution become more evident when the bead is trapped well above the coverslip surface.
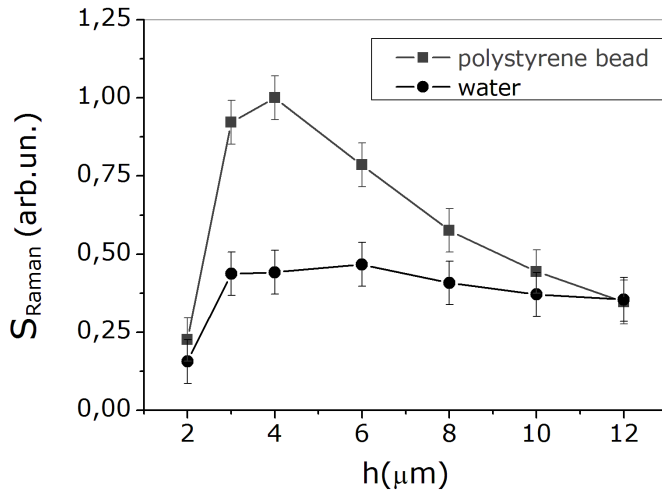
Figure 5.2: *Polystyrene (squares) and water (triangles) Raman signal S_{Raman} as a function of the bead levitation distance h from the coverslip.*

A quantitative investigation of this effect is shown in Fig. 5.2, where S_{Raman} values of both polystyrene (3055 cm^{-1}) and water (3420 cm^{-1}) peaks are plotted versus the trapping distance h from the coverslip surface (h = 2 μm corresponds to contact

position for a 4-μm-diameter bead). The two sets of data exhibit different behavior. The polystyrene peaks increase from the contact position up to 4 μm, where S_{Raman} reaches its maximum. S_{Raman} begins to fall off at larger distances. This is due to both the decrease of photon collection efficiency and optical aberrations, which lead to a broadening of the spot size (as will be discussed later on). Unlike the polystyrene peak behavior, the water peak decreases slowly, because aberrations and collection efficiency are partially compensated by a larger water volume probed by the pump beam. As a direct consequence, the effective spectrum resulting from background subtraction depends on the levitation distance h.

5.3   Phase-sensitive detection
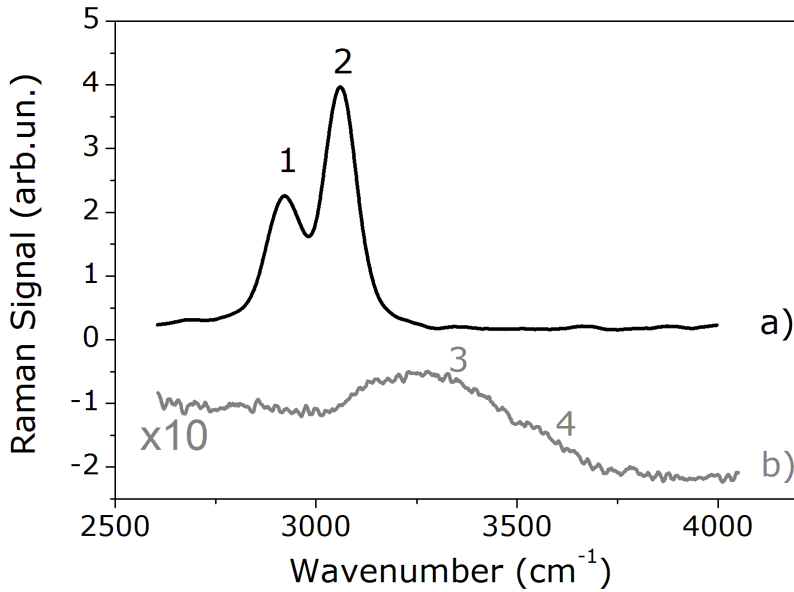
Figure 5.3: *Spectra acquired by modulating the bead position at f=15 Hz frequency and by detecting the scattering signal at 2f. Trace (a) corresponds to the signal acquired by choosing the detection phase in order to maximize the polystyrene Raman peaks, while in trace (b) the phase has been shifted by 90°. For the sake of clarity, this last signal has been vertically shifted and multiplied by a factor 10.*

The same spectral region is therefore investigated by modulating sinusoidally the bead position and detecting the signal by using a photomultiplier. The detected sig-
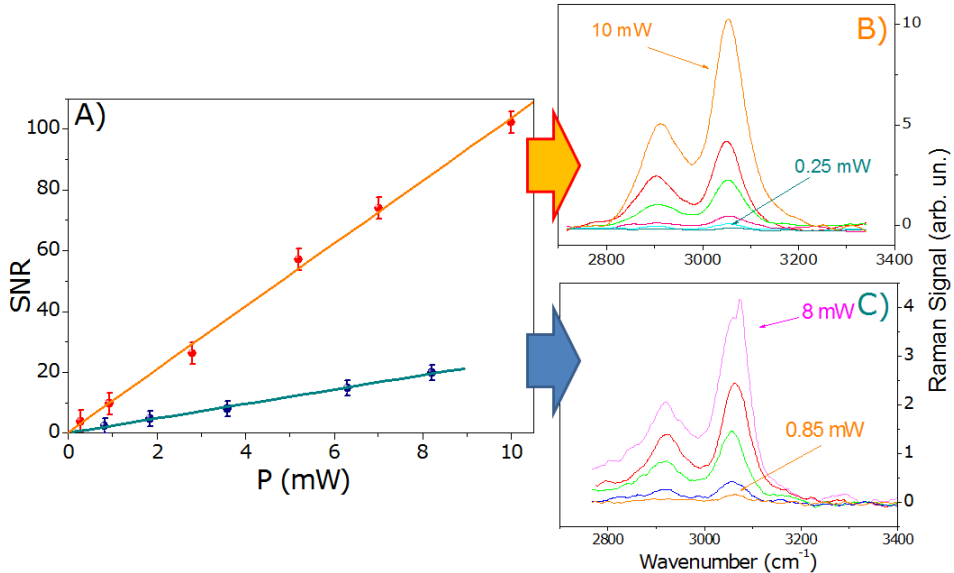
Figure 5.4: *(A): SNR of the polystyrene Raman peak at 3055 cm^{-1} as a function of the pump laser power acquired by using the phase-sensitive technique (red dots) and the standard confocal technique (blue dots). In the insets, we show the spectra recorded at different pump laser powers by phase-sensitive (B) and standard confocal (C) techniques.*

nal modulated at frequency 2f is finally processed by using a lock-in amplifier. The modulation frequency is adjusted by keeping the dragging force exerted on the bead by the fluid smaller than the trapping force. The Raman signal is acquired setting the modulation frequency f at 35 Hz. The maximum excursion A_{max} of the modulation is about 3 μm, that is larger than the bead radius. In Fig. 5.3, trace (a), we show the polystyrene Raman spectrum around 3050 cm^{-1}, optimized by changing the lock-in amplifier phase. The spectrum is acquired in the same experimental conditions (acquisition time, lock-in integration time, Raman probe power) as the spectrum of Fig. 5.1. The acquired spectrum is now background-free. In particular, it is also important to underline that the water Raman and fluorescence features are, in real time, completely removed. Actually, water peaks appear by acquiring the spectrum by shifting the lock-in detection phase by 90° (trace (b) in Fig. 5.3). The residual slope overlapped to the water spectrum may be due, in this case, to water fluorescence contribution. Comparing the spectrum (a) in Fig. 5.3 with the spectrum (c) in Fig.

5.1, we see that the phase-sensitive method not only removes the background, but it also presents a better signal-to-noise ratio (SNR). This results from the propagation of random noise in the subtraction procedure. In particular, form a multi-peaks fit of the experimental spectra it has been extrapolated the $SNR = I_{Raman}/N$, where I_{Raman} is the height of an assigned Raman peak and N is the noise fluctuations obtained by comparing the experimental data with the theoretical fit (residual). In order to estimate the sensitivity of the *standard confocal* and *phase-sensitive* techniques, we determined the SNR of one polystyrene peak (3055 cm^{-1}) as a function of the pump laser power. The results are shown in Fig. 5.4. By fitting the two straight lines of Fig. 5.4, we found that the slope of the *phase-sensitive* technique was 6 times greater than the *standard confocal* technique. It is also worth noticing that, since in the trapping modulation technique the sample is exposed to a shorter time, higher pump laser power can be employed, keeping low the thermal damage. This is particularly advantageous for biological material.

5.4   Phase-sensitive detection applied to immobilized particles

Generally, immobilization of living organisms on a coverslip may yield changes in the electrochemical potential across the cell membrane which, on the other side, affects cellular functions. Nevertheless, there are several practical situations (very heavy samples, low particle refraction index, etc.) in which optical levitation beside the surface becomes more problematic. In these cases, background-free spectra can still be achieved using phase-sensitive detection by directly modulating the stage where the specimen is placed. To test this method, the sample cell, consisting of 4.25-μm polystyrene beads suspended in water, was mounted over a piezoelectric stage. After ~1 h, several beads were found to have spontaneously adhered onto the surface. At this point, we applied a sinusoidal voltage signal to the piezoelectric stage. The amplitude was regulated to obtain an excursion larger than the bead radius while the frequency was 80 Hz. In Fig. 5.5(a), we report a typical Raman spectrum of one of these beads recorded by using the *standard confocal* technique; part (b) shows the same Raman spectrum obtained by setting in oscillation the PZT stage and detecting the *2f* component with the lock-in amplifier. As can also be noted, in
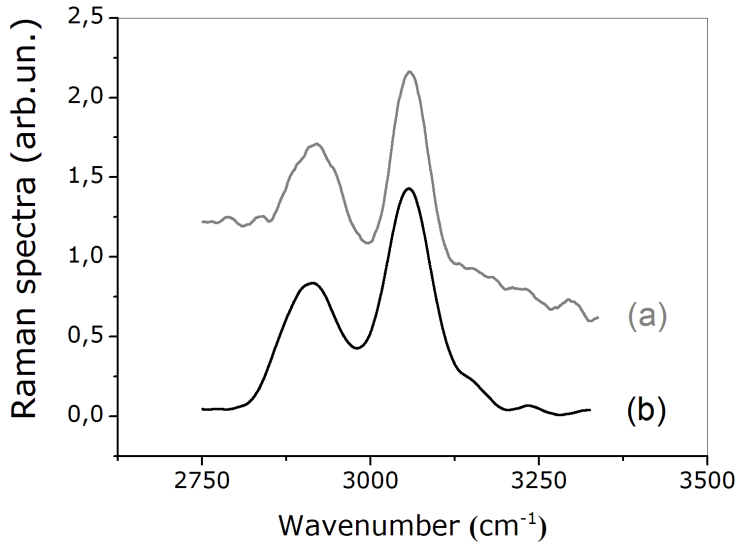
Figure 5.5: *(a) Raman spectrum of polystyrene bead attached on surface acquired by using the standard confocal technique. (b) Raman spectrum of the same sample acquired by modulating the sample holder at the frequency of 80 Hz.*

this case, when the sample is spatially modulated, the background is removed. Nevertheless, unlike trapped beads, the SNR is now slightly poorer. This could be due to intrinsic interference effects on the surface where the particle is attached. Stage modulation can also be useful when the medium where beads are embedded is particularly viscous and dragging force limits oscillations at too low a frequency.

5.5   Study of the formation of the Raman signal

In Fig. 5.6, we report the intensity of the polystyrene Raman peak at 3055 cm^{-1} as a function of the modulation amplitude A. The different sets of data, all obtained by using 2-μm-diameter beads, correspond to several heights from the coverslip, ranging from 3 to 12 μm. A common feature for all the experimental curves is the presence of two regions. In the first one, the signal increases almost linearly and then reaches a plateau. This trend can be easily understood: as the modulation amplitude
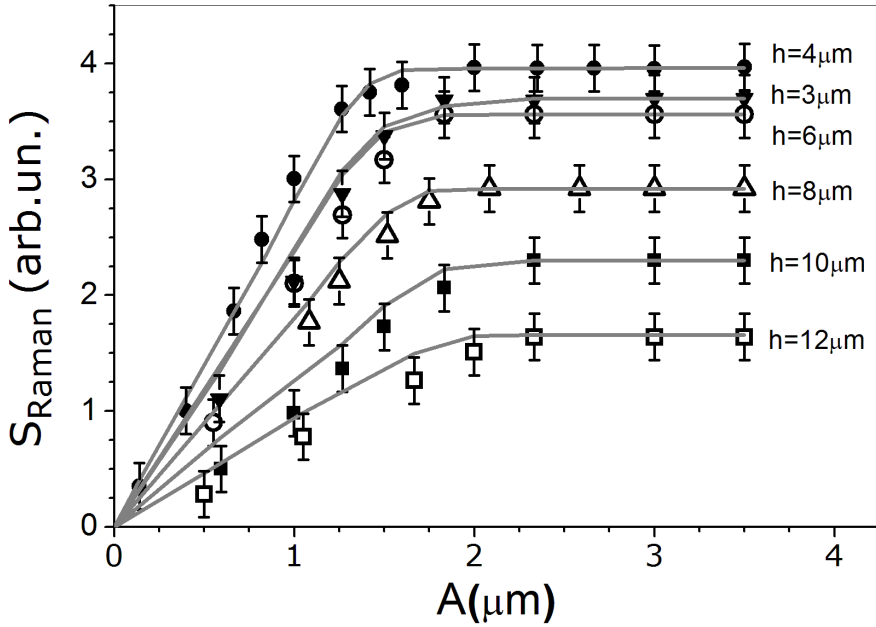
Figure 5.6: *Trends of the Raman signal S_{Raman} for the 3055 cm^{-1} polystyrene peak as a function of the modulation amplitude A. The different sets of data correspond to different bead levitation heights h from the coverslip. The continuous curves correspond to a numerical fit of the data, obtained by a Monte Carlo simulation.*

increases, a larger part of the bead volume is periodically illuminated by the pump laser, approaching the position in which the whole bead is completely shining. By further increasing A, S_{Raman} reaches a saturation plateau (S_{Raman}^{max}). As can be seen in Fig. 5.6, as the trapping height h increases the modulation amplitude value, in which is reached saturation plateau, also increased and at the same time, S_{Raman}^{max} decreases. Both trends can be attributed to a broadening of the pump laser spot size in the focal plane. In order to treat this phenomenon quantitatively, we have fitted the experimental curves with our Monte Carlo simulation. We considered the beam waist w_0 as a free parameter in a best-fit procedure. The fitting curves so obtained are drawn in Fig. 5.6 with continuous lines; these curves satisfactorily match the experimental data.

The w_0 values determined from the fits are plotted in Fig. 5.7 (dots). Apart from a
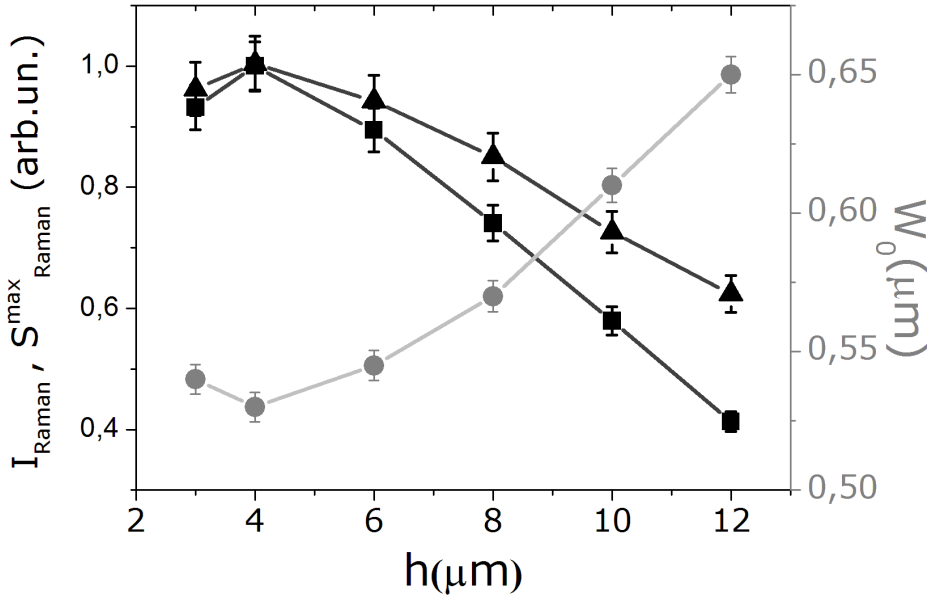
Figure 5.7: *(dots) Pump laser beam waist at the focal plane as a function of the height h from the coverslip, that has been estimated by the fit procedure of the curves of Fig. 5.6. (squares) Raman signal S_{Raman}^{max} for the 3055 cm^{-1} polystyrene peak. (triangles) Pump laser intensity I_{Raman} as calculated by eq. 5.1 in the text. I_{Raman} and S_{Raman}^{max} are normalized to the value at h=4 μm.*

slight narrowing effect, observed very close to the glass surface, the laser spot broadens as the penetration inside the sample increases. This dependence of w_0 on the beam penetration can be mainly ascribed to optical aberrations caused by the refractive index mismatch at the glass-water interface. This effect has been already observed in typical Optical Tweezers experiments where the quality of the trap deteriorates when trapping deep inside the sample [121, 122]. In particular, the force constant (trapping stiffness) decreases as a function of the axial position [123]. In Fig. 5.7 (squares), we also plot the behavior of S_{Raman}^{max} (as estimated from the plateau of Fig. 5.6) versus h. A direct explanation of this behavior can be given if we remember that the broadening of the laser spot diminishes the pump laser intensity I_{Raman}

and, hence the Raman signal. I_{Raman} can be directly calculated by the relation

$$I_{Raman} = \frac{P}{\pi(w_0^i)^2} \ ,$$

(5.1)

where w_0^i is the spot size as estimated from the fitting procedure. For comparison in Fig. 5.7, we report the values of I_{Raman} as estimated from eq. 5.1. Although the two behaviors look quite similar, the discrepancy demonstrates that the decreasing of the Raman signal cannot be explained only in terms of the diminishing of I_{Raman}; further effects, such as the collection efficiency, could have some role in this phenomenon.

5.6   Spatial resolution
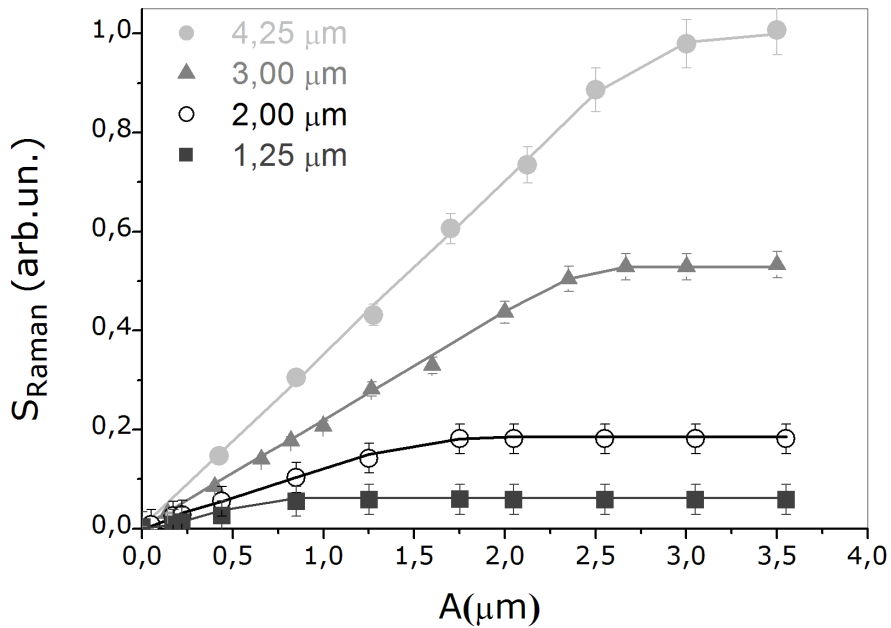
Figure 5.8: *Raman signal S_{Raman} (3055 cm^{-1}) versus the modulation amplitude A. The different sets of data correspond to different bead diameters: 1.25, 2.00, 3.00, and 4.25 μm. The continuous curves correspond to a numerical fit of the data, obtained with a Monte Carlo simulation.*

As already discussed above, the trapping modulation technique allows to spatially select the Raman signal of the solvent in a small region surrounding the mod-

ulated trapped bead. We have investigated this feature by analyzing a series of polystyrene beads of different sizes (1.25-4.25 μm). In Fig. 5.8, we report S_{Raman} of the polystyrene Raman peak as a function of the modulation amplitude, at a fixed levitation height (h = 4 μm); the experimental data were again compared with the theoretical values determined from our Monte Carlo simulation algorithm. Also, in this case, experimental data fit the theoretical curves quite well. The smaller the bead, the smaller is the modulation amplitude that we need to reach S_{Raman}^{max}. In particular, for a 1-μm bead, this occurs for A = 0.53 μm. Under these experimental conditions, the 90° shifted lock-in output provides the maximum Raman signal of a solvent volume of

$$V_{phase-sensitive} = \frac{4}{3}\pi(A)^3 = 0.62 \pm 0.05 fl \ .$$ (5.2)

This spatial resolution is comparable to that obtainable with a Raman confocal system, as shown in the next section. In addition, a three-dimensional mapping of the sample could be reconstructed by scanning the position of the trapped bead. This three-dimensional spatial resolution makes our method suitable for spatial investigation of an inhomogeneous medium.

Finally, we return to Fig. 5.8 to discuss the dependence of the maximum Raman signal S_{Raman}^{max} on bead size. As expected, S_{Raman}^{max} does not scale as the bead volume as depicted in Fig. 5.9, where S_{Raman}^{max} is plotted versus a^3. The deviation from the straight line $y = a^3$ (see dashed line in Fig. 5.9) is simply due to the fact that the pump laser only partially illuminates the bead volume. Again, a Monte Carlo simulation gives good agreement with experimental data (see continuous line in Fig. 5.9).

5.7   Resolution of the standard confocal Raman microscopy

In this section, the small-volume sampling capabilities of standard confocal Raman microscopy are evaluated by acquiring depth profiles of single, surface attached, 4.25-μm polystyrene beads in water. In particular, the sensitivity and spatial selectivity for confocal microscopy is compared with that obtained with our phase-sensitive method.

To test this issue, it has been measured the Raman signal from a discontinuous medium (polystyrene/water). By choosing a single 4.25-μm polystyrene bead, it is possible to consider almost plane the surface of polystyrene bead. In such a way,
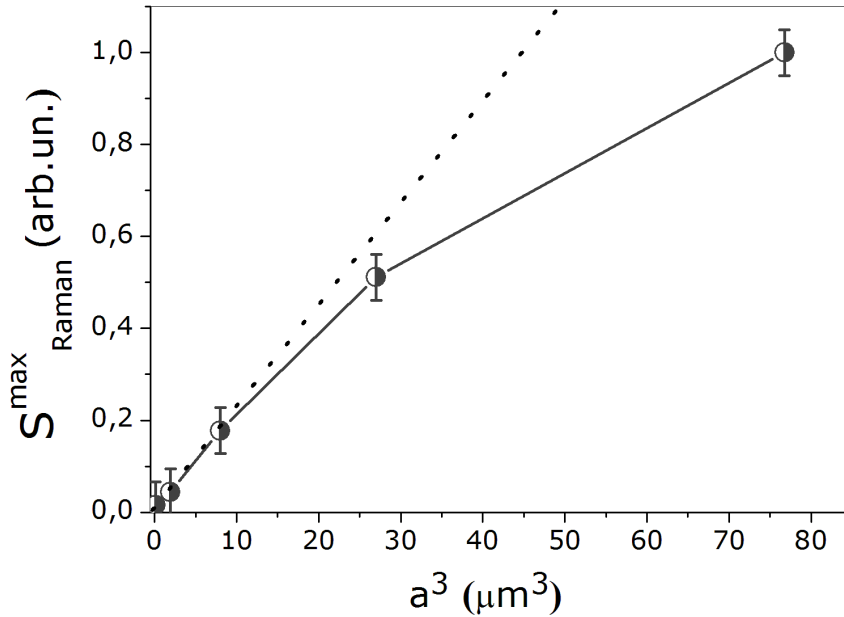
Figure 5.9: *Raman signal S_{Raman}^{max} as a function of a^3. The dashed line corresponds to the straight line $y = a^3$.*

it has been reconstructed the axial resolution by acquiring Raman spectra in 0.5 μm steps in z direction starting at the coverslip surface and scanning through the particle into the solution. Spectra were acquired with 20-s integrations to provide an adequate signal-to-noise ratio. The same procedure has been repeated by focalizing the spot laser in the center of the particle and by scanning the Raman probe in the x-y plane, to obtain information on radial resolution. Measurement of the axial resolution for confocal Raman method is reported in Fig. 5.10, where it is shown the intensity of polystyrene peak at 1004 cm^{-1} as function the position of the laser focus from bottom to top of the particle. The Raman intensity was normalized to the highest number of counts observed along any scan. The intensity reaches a maximum at a depth of $\sim$ 2 μm and falls off very slowly with distance from the coverslip (see the scan range between 2-8 μm in Fig. 5.10). This falloff in the intensity is due to a decrease in collection efficiency of the objective as the focal plane moves into the sample. Spatial resolution was calculated as the distance corresponding to the in-
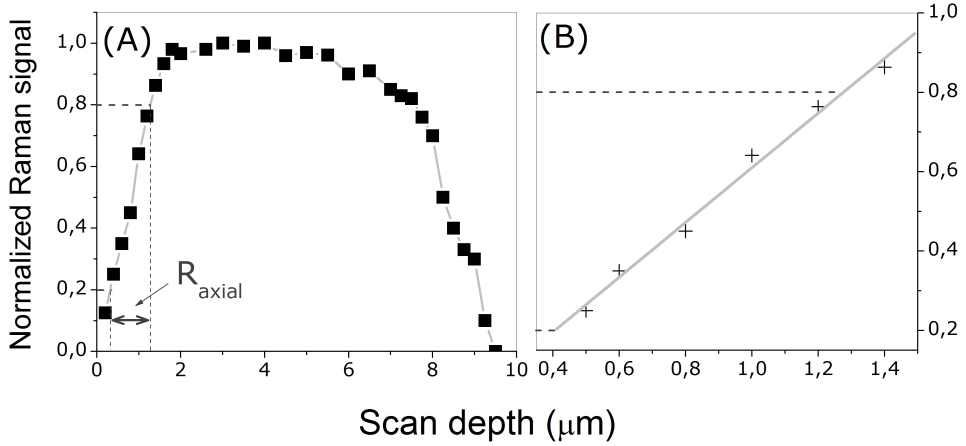
Figure 5.10: *(A)Normalized polystyrene Raman scattering at 1004 cm^{-1} versus position of the focus above the coverslip surface (or scan depth). (B) Zoom on the region between 0.4-1.5 μm. By way of a linear fit of the experimental data, it is possible to estimate the distance corresponding to the increase of the Raman signal from 20% to 80%.*

creasing of the Raman signal from 20% to 80% (see Fig. 5.10, (B)). The resulting axial resolution is:

$$R_{axial} = 0.89 \pm 0.05 \mu m \ , \tag{5.3}$$

which slightly deviates from the expected value in eq. 4.5.

The results concerning radial resolution are reported in Fig. 5.11. In such a case, the intensity of Raman peak at 1004 cm^{-1} reaches a maximum at a position of ~ 1 μm from the bead surface. By fitting the experimental data and by calculating the distance corresponding to the increasing of the Raman signal from 20% to 80%, the obtained radial resolution is:

$$R_{radial} = 0.36 \pm 0.03 \mu m \ . \tag{5.4}$$

As for the axial resolution, the obtained experimental radial resolution is greater than the expected value in eq. 4.3. Therefore, the experimental confocal volume is given by:

$$V_{confocal} = (\pi)^{3/2} \cdot R_{radial}^2 \cdot R_{axial} = 0.64 \pm 0.04 fl \ , \tag{5.5}$$
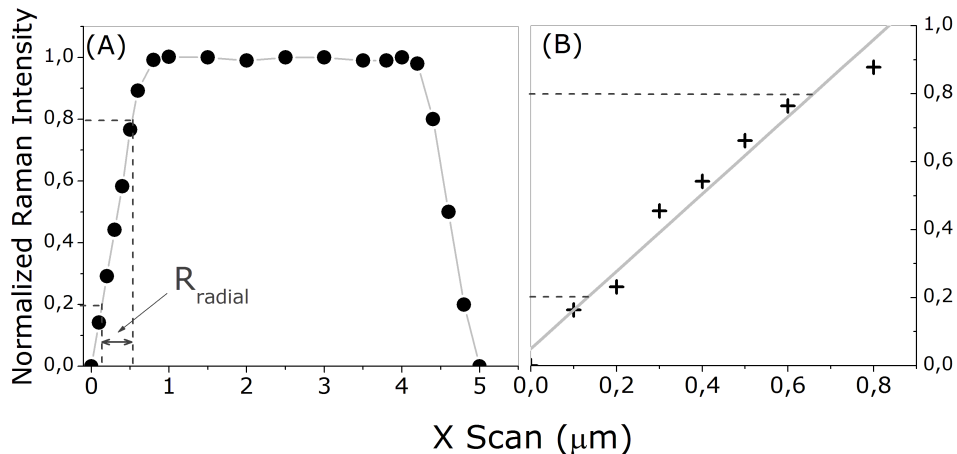
Figure 5.11: *(A) Normalized polystyrene Raman scattering at 1004 cm^{-1} versus the position of the focus along the x-y plane (or x depth). (B) Zoom on the region between 0-1 μm.*

which is comparable with that obtained by using the phase-sensitive detection in eq. 5.2.

5.8   Conclusions

We have demonstrated the use of Raman Tweezers combined with a phase-sensitive detection scheme. Within this approach, the background due to the scattering of the environment is completely removed. The sensitivity enhancement was used to record Raman spectra of single polystyrene microbeads suspended in aqueous solution. This chapter has been mainly devoted to a systematic characterization of the technique. We have described in detail the formation of the Raman signal and its dependence on several parameters, such as the height from the coverslip surface, the size of the bead, the amplitude of the spatial modulation of the trapped particle, and the pump laser intensity. In addition, a model based on a Monte Carlo simulation has provided a theoretical estimation of the Raman intensities, which are in good agreement with our experimental results. Finally, a comparison with standard confocal Raman microscopy has been also shown.

Our results demonstrate that this method may find valuable applications in rapid

sensing of biological samples in aqueous solutions.

6

Spectroscopical characterization of normal and thalassemic red blood cells

In this chapter, I will demonstrate the capability of the developed Raman Tweezers system to characterize biological sample. In particular, the effects of thalassemia, a blood disease quite diffuse in the Mediterranean sea region, will be investigated at single cell level. By resonant excitation of hemoglobin Raman bands, it will be examined the oxygenation capability of normal and thalassemic erythrocytes. Moreover, the response to photo-induced oxidative stress of diseased cells with respect to the normal ones will be analyzed.

6.1   Introduction

Erythrocytes, also referred as red blood cells (RBCs), perform the most important blood duty and play an essential role in human respiratory function. They can be schematized as a vesicle (cell membrane) in which is enclosed a viscous solution of hemoglobin (Hb). Hemoglobin is the oxygen-carrying metalloprotein of the RBCs, and is a protein made up of four polypeptide subunits (two alpha and two beta
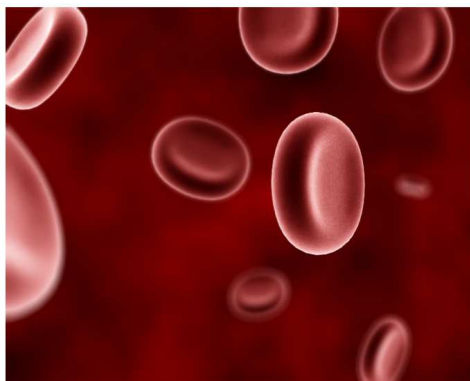
Figure 6.1: *Human red blood cells.*

chains), as seen in Fig. 6.2.   Each subunit is composed of a protein chain tightly
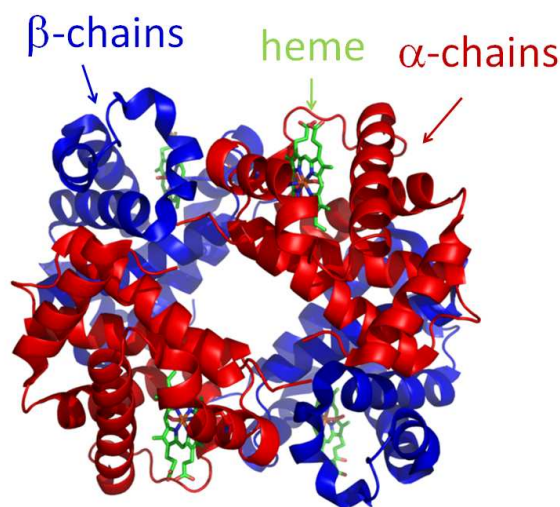
Figure 6.2: *Structure of the human hemoglobin. The protein's α and β subunits are in red and blue,respectively, and the iron-containing heme groups in green.*

associated with a prosteic *heme* group. Each protein chain arranges into a set of alpha-helix structural segments connected together in a globin fold arrangement, so called because this arrangement is the same folding motif used in other heme/globin proteins such as myoglobin. This folding pattern contains a pocket which strongly binds

the heme group.   A heme group consists of an iron (Fe) ion (charged atom) held
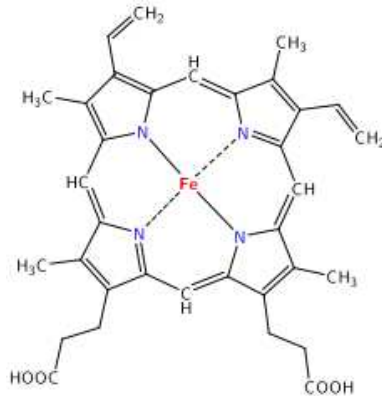
Figure 6.3: *Heme group consists of an iron ion held in a heterocyclic ring.*

in a heterocyclic ring, known as a porphyrin (see Fig. 6.3). The iron ion, which is the site of oxygen binding, coordinates with the four nitrogens in the center of the ring, which all lie in one plane. The iron is also bound strongly to the globular protein via the imidazole ring of the F8 histidine residue below the porphyrin ring.
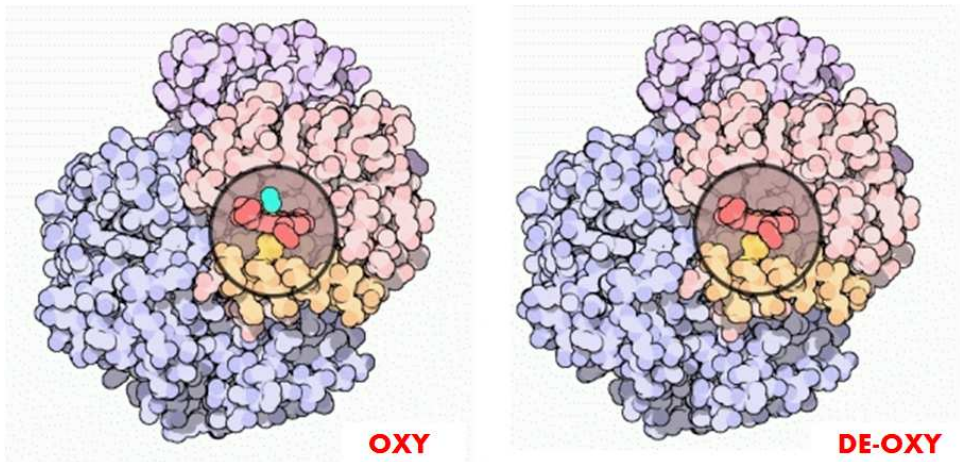
Figure 6.4: *Binding and release of ligands induces a conformational (structural) change in hemoglobin. Here, the binding and release of oxygen illustrates the structural differences between oxy- and deoxy-hemoglobin, respectively. Only one of the four heme groups has been shown.*

When oxygen binds to the iron center (see Fig. 6.4), it causes contraction of the iron atom, and causes it to move back into the center of the porphyrin ring plane. At the same time, binding and release of oxygen induces a conformational (structural) change in the porphyrin ring plane itself.

The high symmetry and the chromophoric structure of the heme result in strong enhancement of the Raman Scattering using laser wavelengths close to the heme electronic absorption bands [9, 18, 124, 125] (see Fig. 6.5). The occurrence of resonance
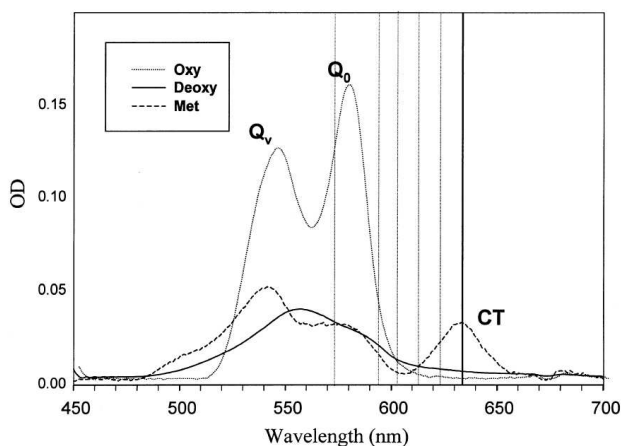
Figure 6.5: *Visible absorption spectra of living erythrocytes recorded in the oxy, deoxy and met states showing the major visible electronic transition bands and the excitation wavelengths used in this study [18].*

Raman scattering (RRS) from the Hb prostheic group allows the investigation of Hb within erythrocytes without interference by other RBC component scattering [19–21]. This is a quite interesting issue for the characterization of Hb-related blood diseases, such as thalassemias.

Thalassemia is a disease of RBC inherited as a semidominant trait, quite diffuse in the populations of the Mediterranean sea. This geographical association was responsible for its naming: Thalassa ($\Theta\acute{\alpha}\lambda\alpha\sigma\sigma\alpha$) is Greek for the sea, Haema ($\alpha\iota\mu\alpha$) is Greek for blood. In thalassemia, the genetic defect results in reduced rate of synthesis of one of the globin chains that make up hemoglobin. Reduced synthesis of one of the globin chains can cause the formation of abnormal haemoglobin molecules, and this in turn causes the anemia which is the characteristic presenting symptom of the

thalassemias.

The thalassemias are classified according to which chain of the hemoglobin molecule is affected. In α-thalassemia, production of the α globin chain is affected, while in β-thalassemia production of the β globin chain is affected. As a consequence, α/β chain ratio is imbalanced, leading to an excess of the normal chain, which may be more injurious to the cell than the defect of the affected chain. Indeed, free globin chains bind to the cell membrane, damaging it and rendering the cell more vulnerable to mechanical injuries. β-thalassemia is the most common of this disease; its incidence can be as high as 1 in 10 in some Mediterranean areas.

In this chapter we present the results of the characterization of RBC from (n=6) β-thalassemic and (n=1) α-thalassemic patients obtained by using an OT system integrated with a Raman probe [126–128]. In particular, we compare the Raman spectra of single thalassemic RBCs (t-RBCs) with those obtained from healthy subjects, relating the observed differences to the analyzed disease. We also investigate photo-induced effects caused by the laser radiations used for both trapping and Raman excitation.

6.2 Resonance Raman spectroscopy of trapped erythrocytes

Fig. 6.6 shows a typical Raman spectrum, between 1100 and 1750 cm^{-1}, of a single optically trapped functional erythrocyte from a healthy volunteer. It was obtained with an excitation power of 0.2 mW and an integration time of 10 s. The contribution due to the buffer solution, taken by removing the RBC from the trap, was subtracted. No averaging was performed, in order to minimize the exposure time to the Raman probe and, hence, to reduce photo-induced effects. The obtained Raman bands are due to the resonantly enhanced hemoglobin contribution; in particular, enhancement of the inelastic scattering comes from the coupling of Raman excitation with the porphyrin macrocycle Q band. Although the relative intensity of the different Raman bands are strongly affected by the excitation wavelength [19], numerous spectral features can be clearly identified, according to their spectral positions. Band assignment, reported in Table 6.1, follows the work by Abe *et al.* [129] and Hu *et al.* [130] and the successive work of Wood *et al.* [19]. For a better estimation of both spectral position and intensity of the observed Raman features, the spectral region between 1100 and 1750 cm^{-1} was fitted with 14 Lorentzian profiles, each corresponding to an expected
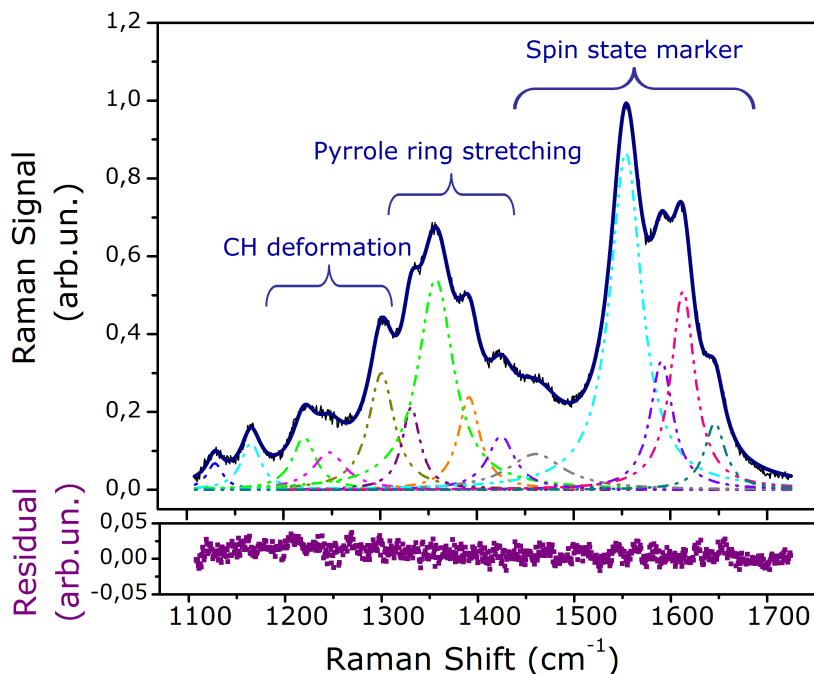
Figure 6.6: *Upper part: Typical Raman spectrum of an healthy RBC, obtained with an integration time of 10 s. The solid line corresponds to a fit with 14 Lorentzian profiles, while the dashed lines indicate the deconvoluted curves. Lower part: Residual obtained as the difference between the experimental and the best-fit spectrum.*

Raman feature [19]. All parameters (intensity, spectral position and width) were allowed to vary in the fitting procedure. The 14 deconvoluted profiles are reported as dashed lines in Fig. 6.6, while the envelope of this curves is shown with a solid line. As it is possible to see from the residual, calculated as the difference between the experimental and fitted spectra and shown in the lower part of Fig. 6.6, the Lorentzian profiles approximate quite well the experimental data.

The spectrum exhibit numerous bands associated with the porphyrin macrocycle and proteinaceous component of Hb molecule and can be divided in essentially three region.

***Core size or spin state marker band* region (1500-1650 cm^{-1}).** The *core size (or spin state marker band)* region (1500-1650 cm^{-1}) is comprised of four principal bands appearing at 1548, 1588, 1604, and 1640 cm^{-1} assigned to ν_{11}, ν_{37}, ν_{19}, and ν_{10} re-

spectively. As a matter of fact, the ν_{37} and ν_{10} bands provide information about the Hb oxidation state: when the Fe atom in the porphyrin heterocyclic ring is linked to oxygen, it is in the low spin state (S=1/2), while in the deoxygenated heme, Iron is in the up spin state (S=2). In these two cases, the porphyrin ring exhibits different symmetries, so that the strength and the spectral position of its vibrations are sensitive to the oxygenation condition.

Pyrrole ring stretching **region (1300-1400 cm^{-1}).** The region between 1300 and 1400 cm^{-1} contains three principal modes assigned to pyrrole ring stretching vibrations with different phasing [130]. These include ν_{41} (1336 cm^{-1}), ν_4 (1356 cm^{-1}) and ν_{20} (1397 cm^{-1}).

Methine C-H deformation **region (1200-1300 cm^{-1}).** The *methine C-H deformation* region (1200-1300 cm^{-1}) consists of two bands assigned to ν_{13} or ν_{42} (1228 cm^{-1}) and ν_{21} (1301 cm^{-1}).

6.3 Resonant Raman characterization of normal and thalassemic RBCs

The prominent Raman features occur in the spectral region between 1500 and 1650 cm^{-1}, which corresponds to the *core size or spin state marker band* region. These strong bands, as highlighted in the last section, provide information on the oxygenation state of the hemoglobin. This issue has been also pointed out by Wood *et al.* [19] in their investigation on the wavelength dependence of human erythrocyte Raman bands. In particular, the authors found that some Raman peaks were absent in deoxygenated RBC, while others shown a valuable energy shift (see Table 6.1). This evidence constitutes the starting point in the interpretation of the erythrocyte Raman spectrum from thalassemic patients.

Figure 6.7 compares the Raman spectrum of a healthy RBC and that corresponding to heterozygous α or β-thalassemic cells. It is possible to highlight some interesting differences. First of all, Raman bands characteristic of oxygenated Hb (oxyHb) are depressed in the α-thalassemic RBC spectrum and are vanishingly small for the β-thalassemic ones. For instance, the ν_{10} band, clearly visible in the spectrum of normal

Table 6.1: *Assignment and spectral position (cm^{-1}) of the Hb Raman bands observed in our work [126]. For comparison, we also report the bands observed by Wood* et al. *[19] for both oxy- and deoxy-Hb with excitation at 514 nm.*

Band Assignment [129]	Local coordinate [130]	Hb 532 nm [126]	Oxy Hb 514 nm [19]	Deoxy Hb 514 nm [19]
ν_{10}	$\nu(C_\alpha C_m)_{asym}$	1640	1638	Absent
ν_{19}	$\nu(C_\alpha C_m)_{asym}$	1604	1604	1604
ν_{37}	$\nu(C_\alpha C_m)_{asym}$	1588	1585	1580
ν_{11}	$\nu(C_\beta C_\beta)$	1548	1547	1546
-CH$_2$(scissor)	-CH$_2$(scissor)	1467	1471	1471
ν_{28}	$\nu(C_\alpha C_m)_{asym}$	1430	1430	1425
ν_{20}	$\nu(pyr quarter - ring)$	1397	1397	1394
ν_4^d	$\nu(pyr half - ring)_{sym}$	1356	1356	1356
ν_{41}	$\nu(pyr half - ring)_{sym}$	1336	1336	1336
ν_{21}	$\delta(C_m H)$	1301	1301	1301
ν_{13}		1248	1245	Absent
ν_{13} or ν_{42}	$\delta(C_m H)$	1223	1228	1220
ν_{30}	$\nu(pyr half - ring)_{asym}$	1170	1171	1172
ν_{22}	$\nu(pyr half - ring)_{asym}$	1131	1134	1124
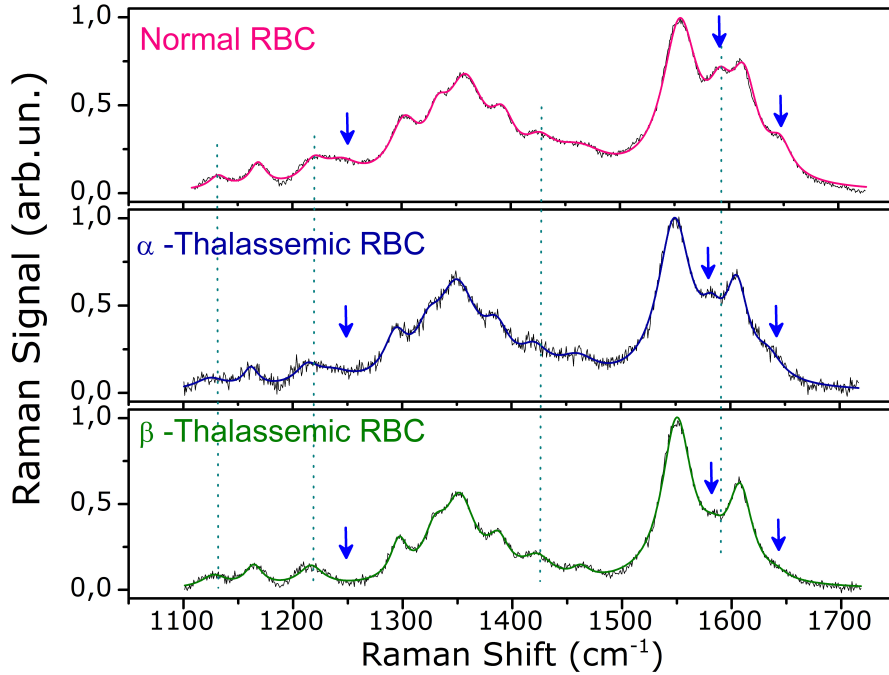
Figure 6.7: *Comparison between the Raman spectra of normal, α and β-thalassemic RBC. The arrows indicate the spectral features affected by intensity changes, while the dashed lines give evidence of the observed energy shift.*

RBC, can be resolved in the spectrum of thalassemic RBCs only after deconvolution from the stronger ν_{19} band by the fitting procedure.

A quantitative analysis of this effect is shown in Fig. 6.8, where we compare the intensity of selected Raman features (ν_{37}, ν_{10} and ν_{13} bands), normalized to the ν_{11} band intensity, for healthy and thalassemic cells. Moreover, numerous Raman bands, affected by oxygenation condition, are energy-shifted (see Table 6.2). Both experimental outcomes clearly mirrors a lower efficiency of t-RBC in carrying out their natural role, namely oxygen transportation from lungs to all the organism.

To test the reproducibility of these results, we performed a statistical analysis on RBCs, collected from normal individuals and heterozygous thalassemic patients. For each sample we performed the Raman analysis described above, estimating the ratio between the intensity of the ν_{37} and that of the ν_{11} bands ($R = I_{\nu_{37}}/I_{\nu_{11}}$).

In Fig. 6.9 we report the statistical distributions, relative to 300 spectra, of the ratio
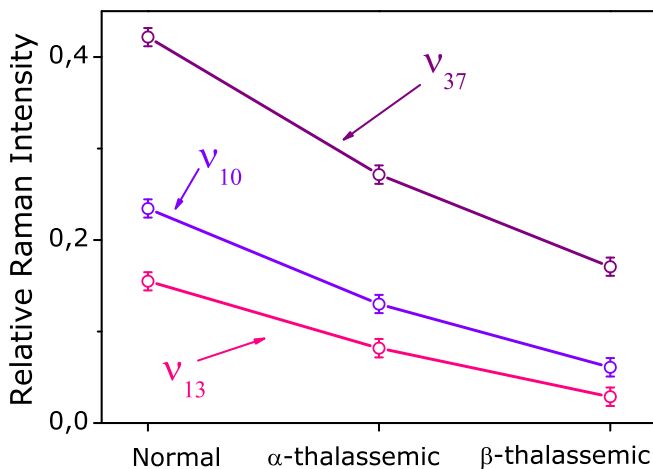
Figure 6.8: *Trends of the relative intensity for selected Raman peaks (ν_{37}, ν_{10} and ν_{13}) corresponding to the three types of cells (see text for details).*

Table 6.2: *Observed wavenumber (cm^{-1}) relative to 4 Raman peaks for normal, α-thalassemic and β-thalassemic RBCs.*

Band Assignment	Normal	α-thalassemic	β-thalassemic
ν_{37}	1588	1580	1581
ν_{28}	1430	1425	1426
ν_{13} or ν_{42}	1223	1214	1215
ν_{22}	1131	1122	1125

R for normal and thalassemic cells. Overlapped to them, we also show the fits with a Gaussian curve. From Fig. 6.9, it is clear that the distributions are well separated; more precisely, they are not overlapping within two standard deviations. For definitive assertions of the effect of thalassemia on the Raman spectrum, more statistical analysis is required. At this purpose, in cooperation with the Haematology Unit of our University (Prof. B. Rotoli), we have analyzed a statistically significant number (n=6) of donors affected by β-thalassemia. It was not possible to make the same kind of analysis regarding α-thalassemia, because this variation of the disease is quite rare.
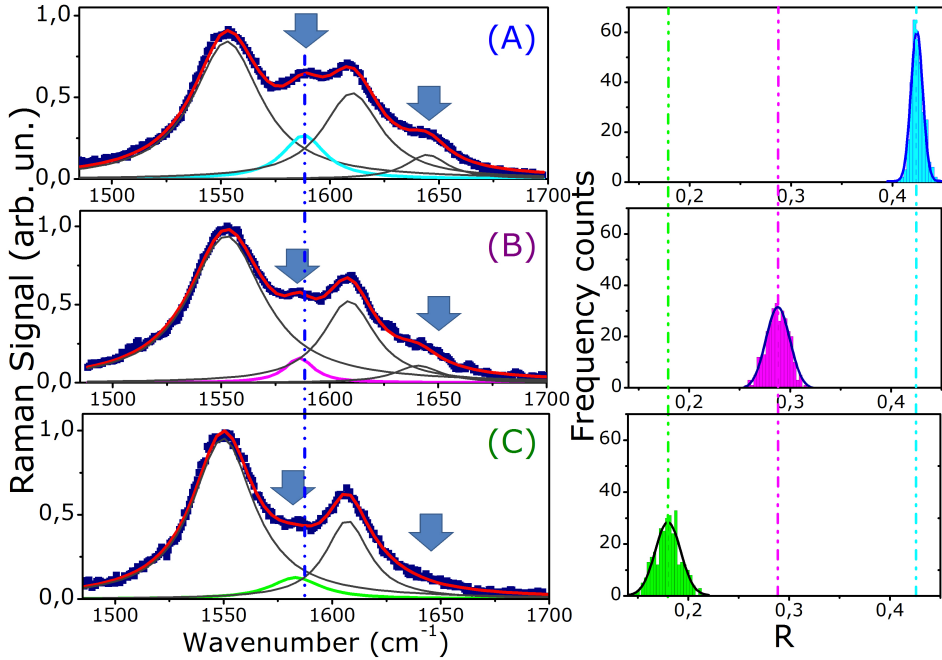
Figure 6.9: *Comparison between the Raman spectra (in the spin state marker band region) and statistical distributions of the ratio $R = I_{\nu_{37}}/I_{\nu_{11}}$ of normal(A), α-(B) and β-thalassemic RBC (C). The arrows indicate the spectral features affected by intensity changes, while the broken lines highlight the observed energy shift.*

However, the aim of the present work is demonstrate that Raman Tweezers are able to provide an unequivocal evidence of differences between healthy and thalassemic red blood cells.

In Fig. 6.10, part A), we report the statistical distributions of the ratio R corresponding to a normal and a beta-thalassemic donor (each distribution is relative to 300 spectra). This analysis was repeated for 6 volunteers for each kind of cells (see Fig. 6.10, part B)). From this investigation, two interesting features emerge. First of all, the distributions are again well separated; more precisely, they are not overlapping within three standard deviations, as evidenced by the horizontal bars, which show the weighted-mean and the standard deviation for the normal and the thalassemic cells [126]. In addition, all t-RBCs distributions present a much wider spread around their mean values with respect to that of healthy RBCs. The wider dis-
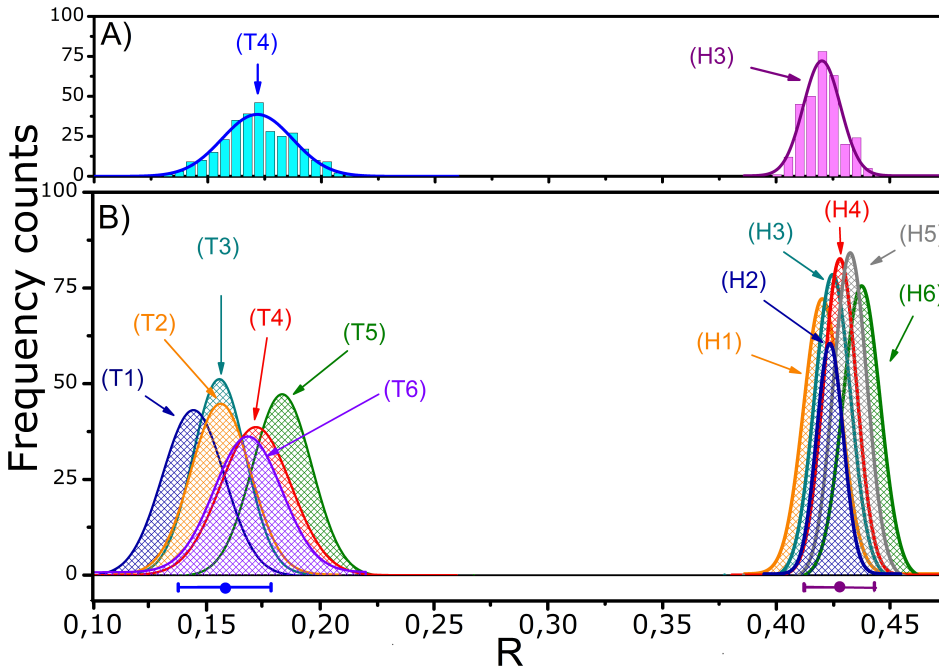
Figure 6.10: *A: Statistical distributions of the ratio $R = I_{\nu_{37}}/I_{\nu_{11}}$ obtained by analyzing 300 RBCs from a single normal (pink histogram) and β-thalassemic (blue histogram) donor. The fit of these distributions with Gaussian profile is also shown. B: Gaussian profiles obtained by fitting the experimental distributions relative to 6 normal (Hi) and 6 β-thalassemic (Ti) volunteers. The weighted-mean and the standard deviation for the two kinds of cells are evidenced by horizontal bars.*

tribution found for diseased RBCs clearly mirror the higher heterogeneity of beta-thalassemic RBCs, which can be also observed in the dimension and shape of these erythrocytes.

We think that these experimental outcomes provide an interesting starting point to explore the application of a Raman Tweezers system in the clinical diagnosis of Hb-related blood disorders.

6.4   RBCs and photo-oxidation

During our experiments a particular care was put in order to reduce photo damages induced by the trap and Raman lasers. Indeed, more generally, when biological
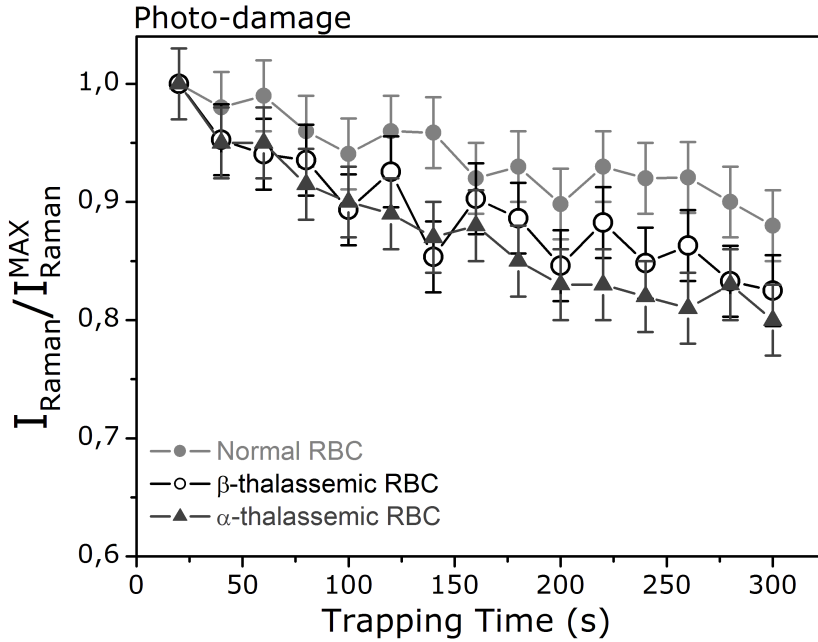
Figure 6.11: *Intensity of the Raman ν_{11} band, as a function of the exposure time to the trapping radiation for normal (●), β-thalassemic (○) and α-thalassemic (△) RBCs. The intensity values are normalized to the value at t=20 s.*

samples are exposed to laser radiation it is important to be aware of possible photo-induced effects. These last have been investigated for normal RBC exposed to visible and IR radiation [19]. In general, it has been established [19] that exposure to high-power radiation in the green region leads to protein denaturation and Hb transfer into the metHb state, in which the oxygen is irreversibly bound to the heme. In our study we extended this investigation to thalassemic erythrocytes. We first analyzed the effects of exposure of both normal and thalassemic RBC to radiation at 1064 nm, which corresponds to the wavelength of our trapping laser. At this purpose, a single erythrocyte was placed in the optical trap for different time intervals, ranging between 20 and 300 s; at the end of each interval, we monitored RBC vitality by recording its Raman spectrum for 3 s. To avoid the superposition of effects induced by the Raman probe, the RBC was changed after each measurement. The power of the IR beam was taken fixed at 15 mW, while the Raman probe power was 0.2 mW.
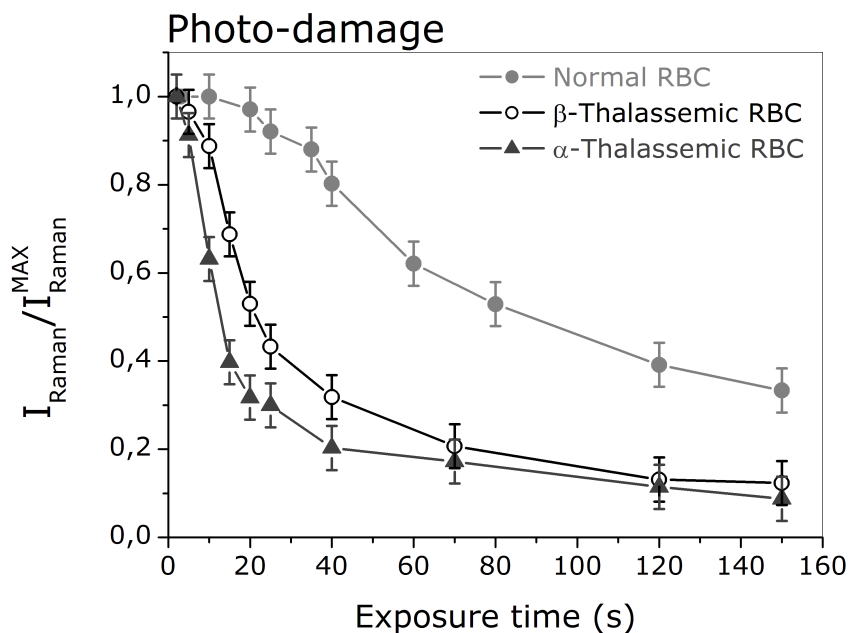
Figure 6.12: *Intensity of the Raman ν_{11} band, as a function of the exposure-time to the Raman probe for normal (●), β-thalassemic (○) and α-thalassemic (△) RBCs. The intensity values are normalized to the value at t=3 s.*

In Fig. 6.11 we report the intensity of the ν_{11} peak at 1548 cm^{-1}, normalized at the maximum value (I_{Raman}^{MAX}), for healthy, α-thalassemic and β-thalassemic RBC. The latter Raman feature is the stronger one for the three kinds of cells and its relative intensity is not affected by Hb met transition. For each trapping time we repeated ten measurements using distinct cells. The points plotted in Fig. 6.11 represent the average values while the error bars are the standard deviations. As it can be seen, the normalized Raman intensity changes by 12 % for normal cells and 18 % for the thalassemic ones on a period of 300 s. In addition, we observed that the relative intensities of the different peaks in the Raman spectra were not affected. This indicates that, at power level used in our experiment, the photo-damage by IR laser trapping is quite low.

The photo-induced effects at 532 nm are, instead, much stronger. Figure 6.12 shows the intensity of the same Raman feature (ν_{11}) as a function of exposure time to the
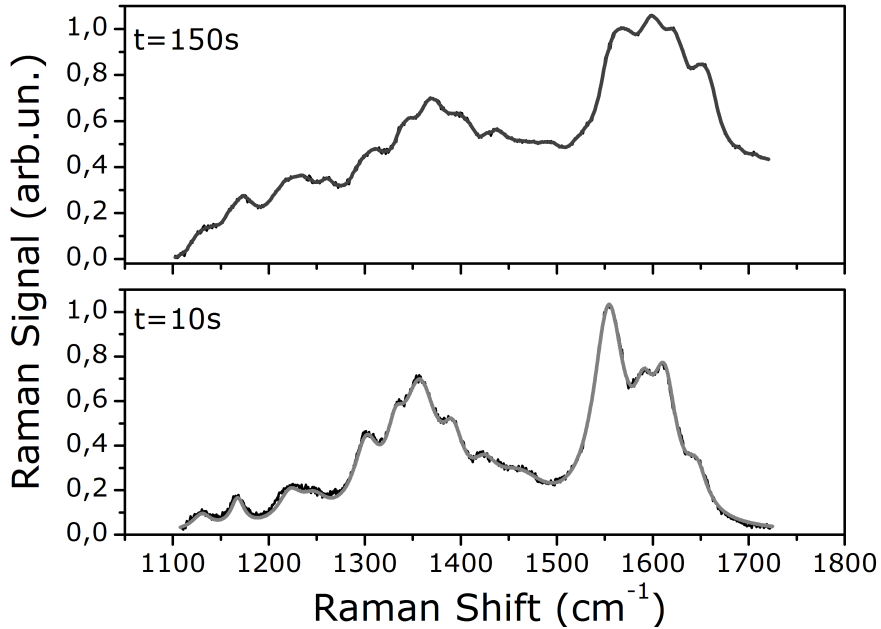
Figure 6.13: *The Raman spectra of a normal RBC exposed to 532 nm radiation for 10 and 150 s. Solid lines are the best fit lineshape convolutions.*

Raman probe, at a power of 0.3 mW (the trapping laser power was kept at 15 mW). Again, the measurements were done trapping one fresh cell and exposing it to 532 nm radiation for a time varying from 3 to 150 s. As for Fig. 6.11, the measurements were normalized to the intensity of the maximum Raman signal, observed at t=3 s.

As it can be observed in Fig. 6.12, the photo-damage is different for the three kinds of cells. For an exposure time of about 80 s, the reduction of the Raman signal is ∼50 % for normal cells and ∼80 % for α- and β-thalassemic cells. Therefore, our investigation shows that thalassemic RBCs are more sensitive to photo-oxydation.

This result confirms a more general trend of thalassemic RBCs to be sensitive to oxidant stress [131, 132]. From a medical point of view, this may be attributed to an excessive oxidation of the unstable free globin chains and the subsequent release of oxygen radicals, that might damage the cell membrane [133]. This information has to be taken into account in all optical analysis of t-RBCs.

Another evidence of the photo-damage is represented by the modification of the

whole Raman spectrum. In Fig. 6.13 are compared the spectra for normal RBC obtained at 10 and 150 s exposure time, respectively. Both spectra were normalized to the highest Raman peak. As it can be seen, for long exposure a background appears and the relative bands intensities are modified. In particular, cellular photo-damage leads to spectral changing in the spin-sensitive region, where an increase of the Raman ν_{37} band is observed, indicating irreversible Hb transition to the met state. Similar effects have been already reported for healthy erythrocytes exposed to radiation at 514 nm and they have been attributed to protein denaturation, resulting in heme aggregation within the cell [124].

6.5   Conclusions

This chapter reports the characterization of heterozygous thalassemic red blood cells, at single cell level, by using a Raman Tweezers system. The study has been performed by analyzing the resonantly enhanced inelastic photons scattering from hemoglobin. Some significant difference in the functionality of these cells with respect to normal erythrocytes have been highlighted. In particular, the oxygenation capability of Hb has revealed to be reduced in thalassemic RBCs. The two types of cells also present a different response to photo-induced oxidative stress. Our results confirm medical predictions regarding thalassemia, such as the reduced oxygenation capability of t-RBCs. Moreover they provide an interesting starting point to explore the application of a Raman Tweezers system in the analysis of others blood disorders. Unlike the traditional diagnostic tools, our approach is able to provide with the same apparatus both chemical and mechanical properties (as demonstrated in the next chapters), even at single RBC level. That allows to extol heterogeneity, which is instead hidden by bulk-based techniques.

7

Raman imaging of single erythrocytes

In this chapter, I will show how Raman analysis can be used to draw hemoglobin distribution inside single erythrocytes. In particular, the experimental outcomes reveal the characteristic anomaly (target shape) occurring in thalassemia. The obtained results in vivo *show the potential of our technique as a diagnostic tool for other hemopathies.*

7.1 Introduction

In the last section, it has been demonstrated how a RT system becomes an incredibly powerful diagnostic tool for cellular sorting and monitoring drug-therapy effects at single cell level. In particular it serves to study cellular processes as they progress. This capability of immediate and detailed analysis has potentially great applications in medicine allowing for quick diagnosis of diseases. As such, Raman tweezers could prove to be an effective analytical tool not only for research purposes, but also as a clinical protocol [126–128].

In many cases it may not be just desirable to have time resolved information about biochemical changes taking place inside a cell but also to have information about

where these changes are occurring. *Raman imaging or mapping* of cells plots the concentration of various bio-chemicals as a function of position [108]. The Raman cell images can be more easily interpreted than spectra alone by biomedical researchers already familiar with microscopy. The data are acquired either by scanning the laser back and forth across the sample or by scanning the sample across the laser beam, and taking the Raman spectrum at each point [134]. The values of the intensity at a certain peak or peaks are plotted as a function of position. These images provide more information than conventional microscopy images alone as they contain information on all cell components and different cell components can be visualized by post-processing of data. So far, single living cells and subcellular compartments can be molecularly examined rapidly, non-invasively, and without the use of external markers or fluorescent dyes. This novel technique has great potential in medical applications (even for *in vivo* applications), tissue engineering, for determining where assignment biochemical transformations occur inside a cell with spatial resolution of a few nanometers. Indeed, Raman chemical imaging has been used in cell biology, to detect the differences between normal and diseased cells.

In this chapter we present an application of Raman imaging when we reconstruct the hemoglobin distribution within a single Red Blood Cell (RBC). We demonstrate that it can be useful for early diagnoses of hematic diseases such as thalassemia.

7.2   Experimental method

Raman imaging can yield spatially resolved biochemical information from living cells. To realize this goal, in particular, to acquire space-resolved spectra, it is necessary to immobilize the cells. In our work, in order to overcome this problem the use of two double-trap systems is proposed and implemented, and data are shown for spatially resolved Raman spectroscopy of a live RBC in suspension.

Raman Imaging in the equatorial plane of a RBC was performed by scanning the trapped cell through the Raman probe (see Fig. 7.1) [128]. At this purpose, two double-trap systems were created by applying a square voltage signal at a frequency of 1 kHz to two galvomirrors (Cambridge Technology Incorporated, mod. 6220), placed on the optical path of the trapping beam. In such a way, the four optical traps share the beam power and their relative distance was controlled by the voltage signal amplitude. These two double-trap systems allow to fix the cell in four points. Finally,
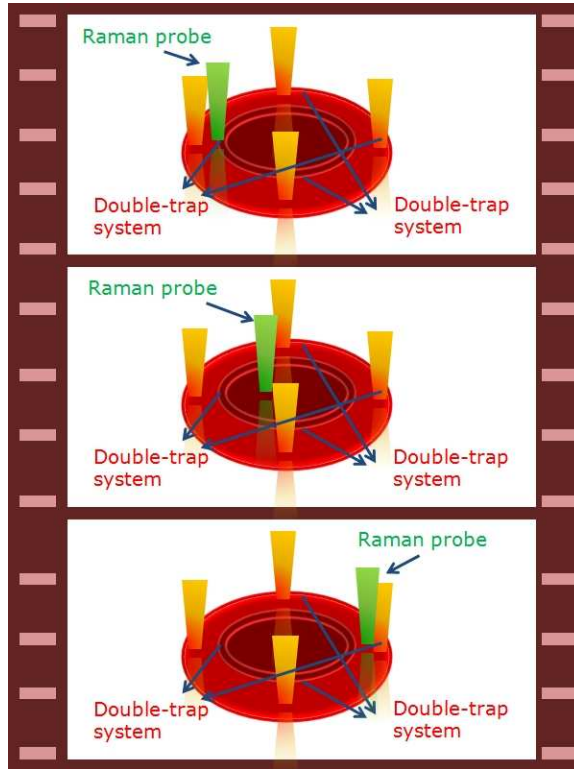
Figure 7.1: *Scheme of the experimental method: the two double-trap systems fix the RBC in four points and by applying an offset signal to the galvo-drivers it is possible to scan the sample across the Raman probe.*

by simply applying an offset signal to the galvomirrors drivers it is possible to scan the RBC through the excitation probe.

In such a way, the trapping laser was used to move a living cell back and forth across the focus of the laser beam for Raman excitation and a spectrum was recorded at each position. The cell was not observed to rotate during the duration of our experiments. For each image a band of interest was selected and the intensity plotted as a function of position.
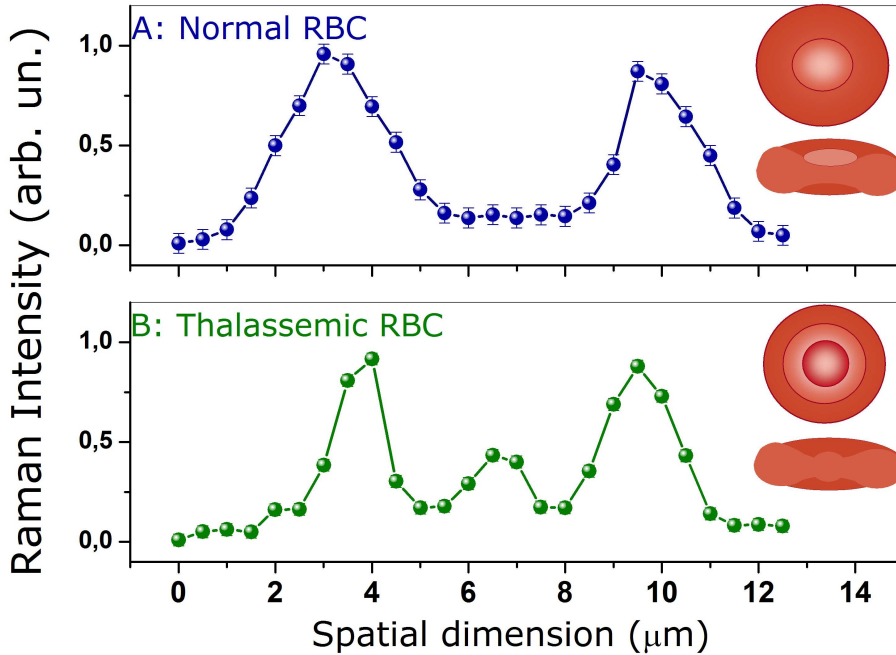
Figure 7.2: *Normalized intensity of Hb ν_{37} peak along a diameter of the equatorial plane of a normal and thalassemic RBC. The error bars are obtained by the fitting procedure of the Raman spectrum. In the insets, their characteristic shape is shown.*

7.3   Raman imaging of normal and thalassemic cells

An observable trait in different hematological diseases, including thalassemia, is related to the Hb distribution inside the cell. Although several experimental techniques provide the morphology of single cells, only few of them are able to reconstruct the distribution of an assigned protein within the cell itself.

In particular, during recent years optical phase-based and fluorescence techniques have advanced considerably [135]. However, this last techniques requires staining with specific fluorophores, such as GFP, which, in some cases, can affect the normal cellular function. On the contrary, Raman imaging allows the investigation of the distribution of a given protein, such as haemoglobin, within cells, avoiding the use of fluorescent labels. So far, we have investigated the Hb distribution inside both normal- and t-RBCs.
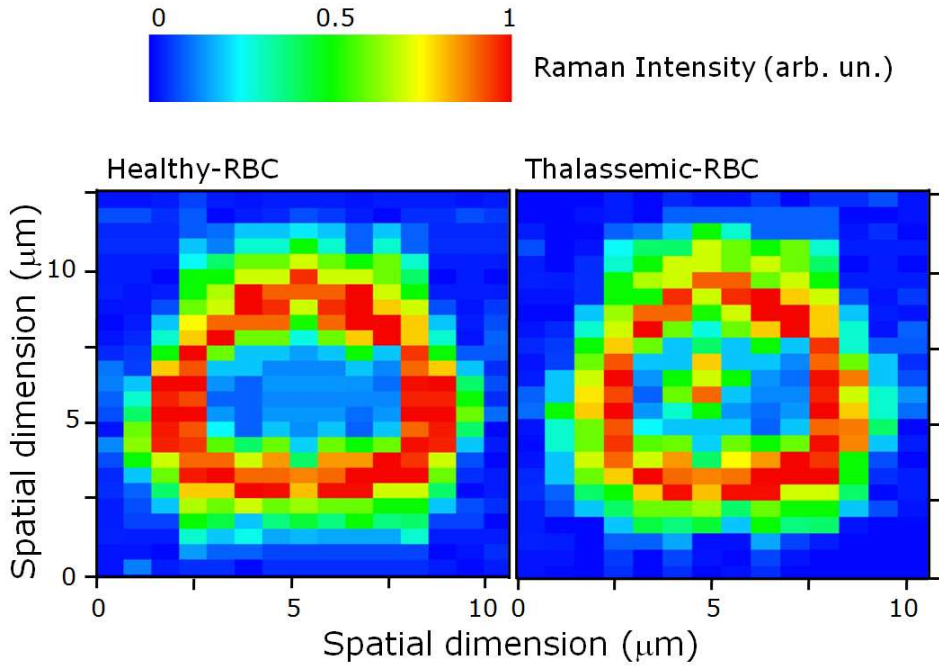
Figure 7.3: *Hb distribution in the equatorial plane of a thalassemic and a healthy RBC.*

At this purpose, by scanning the sample through the Raman probe focus, we were able to reconstruct the Hb distribution within a single erythrocyte. In figures 7.2 we show the distribution obtained along a diameter of the equatorial plane for two different RBCs. It was reconstructed by monitoring the ν_{37} peak intensity. The sample was scanned with a spatial step of 0.5 μm. For an easier comparison, the two distributions were normalized to their maximum value.

Figure 7.3 shows two separate Raman images of a healthy and a thalassemic cell. The Raman image obtained for a normal RBC, reflecting the Hb distribution within the cell, presents the classical ring-shape. No Hb-Raman signal can be detected in the cell center. An erythrocyte with this normal Hb distribution is ordinary referred as *discocyte*. This distribution is modified in diseased cell. In particular, for a statistically significant number of thalassemic RBCs ($\sim 15\%$), it is possible to detect Hb also in the middle of the RBC, so that the obtained RBC Raman image resembles a target shape. These RBCs are referred as *target* RBCs or *codocytes*. This effect is associated

with a reduced RBC size.
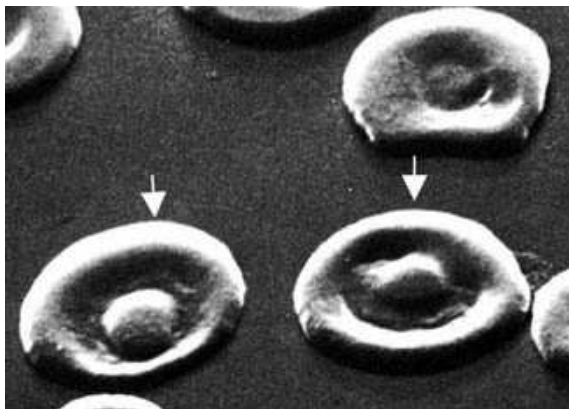
Figure 7.4: *Scanning electron micrograph of blood smear with two target cells or codocytes (white arrows).*

The anomalous Hb distribution here found may be seen also in patients with obstructive liver disease, iron deficiency or post-splenectomy [136].

7.4   Conclusion

This initial study demonstrates the feasibility of Raman imaging using double-trap systems to immobilize and manipulate the cells relative to the exciting beam. Raman imaging was used to reconstruct the hemoglobin distribution inside single erythrocytes. The obtained results show that a RT system may be used for rapid and non-invasive cellular sorting and pave the way for the development of new diagnostic tools for both research and clinical applications.

<div align="right">**8**</div>

Mechanical characterization of healthy and diseased red blood cells

A double-trap system, termed optical stretcher is used to deform objects. In particular in this chapter, I will show how an optical stretcher can be used to measure the elastic properties of red blood cells membrane, with the sensitivity necessary to distinguish even between healthy and diseased one.

8.1 Introduction

The deformation capability of RBC is mainly due to the elasticity of its membrane. The inner fluid of the RBC is purely viscous and has no elasticity. The RBC membrane is made of a lipidic bilayer, covering a protein network essentially composed of spectrin tetrameres linked by actin and protein 4.1 to form complex junctions (see Fig. 8.1). These are the principal component of the cytoskeleton that underlies the RBC membrane accounting for its biconcave shape and its flexibility.

The mechanical properties of such structure has been largely investigated from
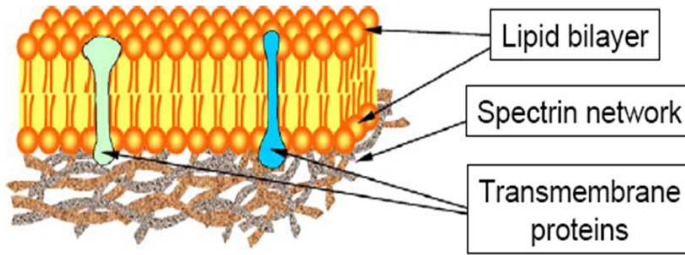
Figure 8.1: *Sketch of the RBCs membrane.*

both theoretical [133, 137, 138] and experimental [139–141] points of view. In the first case, the studies were devoted to develop, through computational simulations, reliable models for the architecture of the spectrin network, able to simulate the erythrocyte mechanical properties. In the second case, the investigations relied on the measurement of cellular distortion in response to an applied mechanical stress. This issue has been addressed by using many different experimental techniques, including mainly micropipette aspiration [142]. This last is based on the creation of a protrusion from the cellular membrane, which is drawn into the pipette. The relation between the protrusion extension and the pressure gives the shear elastic modulus. Recently, Hénon *et al.* [141] have measured this parameter for normal human erythrocytes by using an Optical Tweezers system: in this case, calibrated forces were applied via small silica beads bound to the RBC membrane. The necessity to use such beads arises from the need to exert known forces, in order to obtain an absolute measurement of the RBC shear modulus. Indeed, an absolute force calibration requires trapping of objects of well known shape, size, and composition. Similar measurements have been also performed by Lenormand *et al.* [140] on the free spectrin skeleton, extracted from the membrane of a RBC .

In the present section, it is reported on the mechanical response of t-RBCs compared to healthy ones. It is important to underline that, although thalassemic syndromes concern mainly a genetic defect in hemoglobin synthesis, precipitation of free globin chains leads to various membrane dysfunctions [143]. This is also proven by the presence of defects in morphology and shape of RBC affected by this disease.

8.2 Experimental method
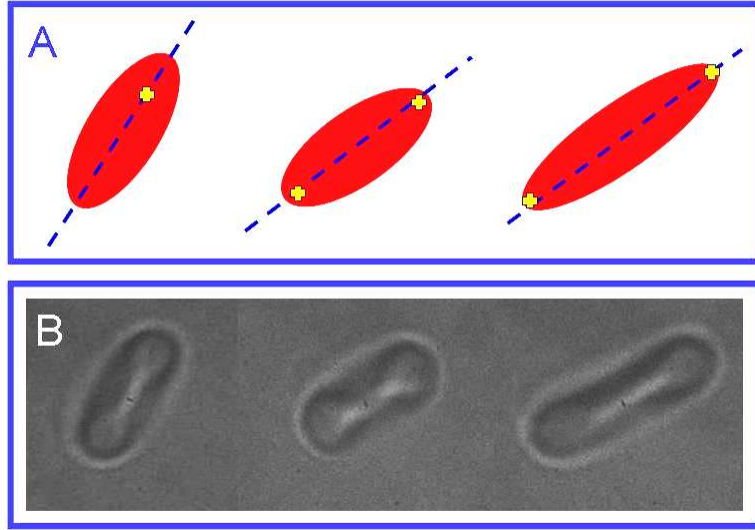
Figure 8.2: *A: Sketch of the stretching procedure used for the present investigation. B: Same frames of a video recorded during the stretching of a normal RBC.*

For the mechanical characterization of RBCs, a double-trap system was created by applying a square voltage signal at a frequency of 1 kHz to a galvomirror (Cambridge Technology Incorporated, mod. 6220), placed on the optical path of the trapping beam. In such a way, the two optical traps shared the beam power and their relative distance was controlled by the voltage signal amplitude.

A sketch of our stretching mechanism is illustrated in Fig. 8.2-A, while in the part B of the same figure some frames of a recorded video are shown. When the voltage applied to the galvomirror is zero, we have a conventional single trap: the RBC reaches a trapped position and floats slightly around it. As the distance between the two traps is increased, the RBC firstly starts orientating along the axis passing through the center of the two traps. After the RBC is fully aligned, it begins to be

stretched.

For a given trapping laser power P, we apply an increased stress to the membrane by slowly incrementing the distance between the two traps. The cell becomes elongated, and its diameter D increases in the direction of the applied force. RBC elongation $(D - D_0)$ was extracted by hand, using an image software (NIH ImageJ). In particular, we recorded 20 images for each erythrocyte elongation. From each image we estimated the major axis of the RBC shape and computed the average length over all the 20 frames. The final accuracy of D is ~ 200 nm.
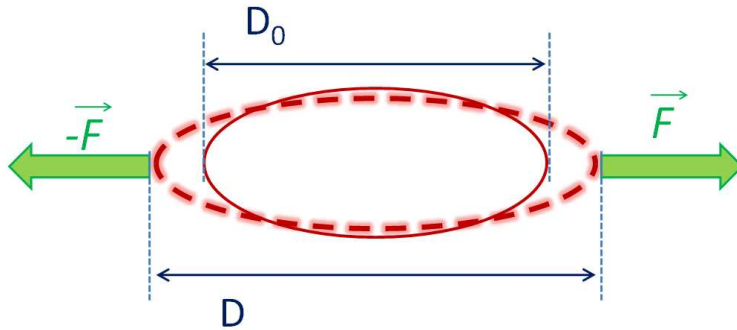
Figure 8.3: *Representation of the elongation of a red blood cell as a consequence of two diametrically opposite applied forces F.*

By varying the laser power P, we collect a set of images of the same cells submitted to different forces, as shown, for instance in Fig. 8.2. If the measurements are quickly repeated, no hysteresis behavior of the shape is observed after the power P is increased and decreased. Actually, when the cell is trapped for several minutes at high power (P>100 mW), some membrane stiffening is observed, and the cell elasticity is affected. Thus we make sure that all of the manipulations on the same cell take place in less than 15 min.

In the small deformation regime of the RBC membrane, which has a constant area in a first approximation, it is possible to demonstrate that [141]:

$$D - D_0 = \frac{F}{k} \qquad (8.1)$$

where $(D - D_0)$ is the diameter elongation, F is the applied force (see Fig. 8.3) and k is the elastic shear modulus of the membrane.

The force exerted on a trapped object depends on its size and shape, and on the refractive indices of the object and the surrounding medium. It is proportional to the incident laser power. However, it is difficult to calculate *ab initio* the restoring force. Furthermore, because of the optical aberrations of the objective, the exact shape of the trap is not well known. Thus a preliminary force calibration is necessary. Due to the comparative character of this investigation, it is not necessary to estimate the calibration *F(P)*. In addition, it is not indispensable to exert the mechanical stretching by using microbeads as handles. Of course, this simplifies the measurement procedure, avoiding the difficulty to obtain RBCs with microbeads adherent to the membrane in a proper relative position [140].

8.3 Response to applied stretching for normal and thalassemic RBCs
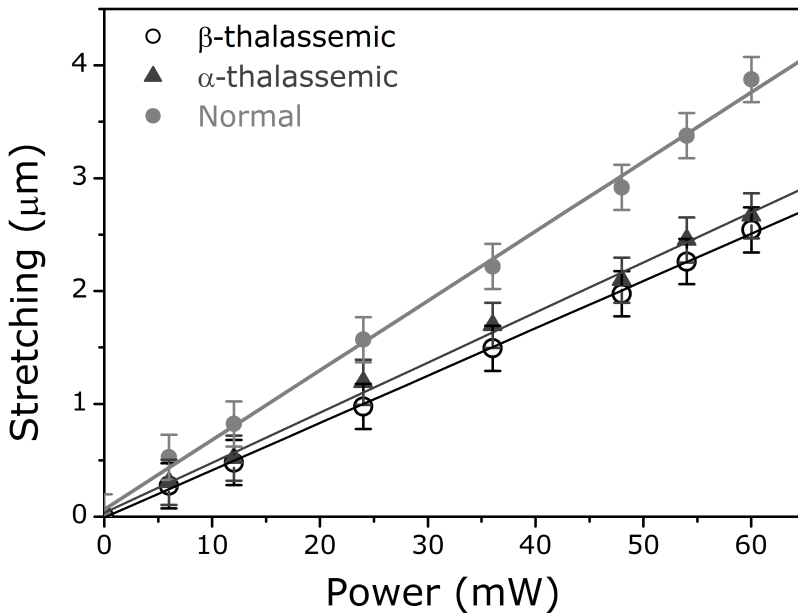
Figure 8.4: *Response to applied stretching for normal and abnormal RBCs.*

Our investigation was performed by stretching single erythrocytes by using a double Optical Tweezers system.

In Fig. 8.4 we report the RBC elongation as a function of the trapping beam power for healthy and thalassemic RBCs. Each value results from an average of 25 measurements performed on different cells. The error bars correspond to the standard deviation. The data plotted in Fig. 8.4 reveal a quite different mechanical response of normal cell with respect to t-RBCs. From a linear fit of the experimental data, it was possible to estimate the ratio of the shear modulus k for the three kinds of cells. These results were: k_n/k_α=0.71±0.06 and k_n/k_β=0.68±0.05.

If we assume k_n=2.5±0.4 pN/μm, as found by Hénon *et al.* [141], we obtain k_α=3.5±0.8 pN/μm for α-thalassemia and k_β=3.7±0.9 pN/μm for β-thalassemia. Previous measurements on β-thalassemic cells, performed with standard micropipette aspiration, brought out an elastic shear modulus in beta-thalassemia 33 % [144] higher than the normal one, against the 48% found here.

Some consideration can be done to explain this difference. First of all, as already pointed out in the ref. [141], since the two methods (double-trap and micropipette) do not operate in the same deformation regime, they are not expected to lead to the same result. Moreover, in micropipette aspiration measurements the friction force between the cellular membrane and the glass pipette wall may have a significant role in force balance.

Finally, in more than 10 % of the total measurements in β thalassemic cells, we observed an evident damage to RBCs by applying strong deformation. In such cases, the stretching caused a membrane fragmentation and a consequent cell death. In all the other cases, the vitality of normal cells was not affected, as also proved by Raman measurements performed before and after application of the mechanical stress.

8.4   Conclusion

In this chapter, it has been showed that Optical Tweezers are a powerful tool not only for manipulating cells, but also for applying forces in the *pN* range. Measuring the induced deformation allows researchers to investigate cell elastic properties. As such, a new determination of the membrane shear modulus *k* at small deformations for normal and thalassemic erythrocytes has been obtained. In particular, the membrane shear modulus for thalassemic erythrocytes have revealed to be higher than 40

% with respect to healthy cells. These results confirm medical predictions regarding thalassemia, such as higher rigidity of RBCs. Moreover they provide an interesting starting point to explore the application of a Raman Tweezers system in the analysis of others blood disorders. Unlike the traditional diagnostic tools, our approach is able to provide with the same apparatus both chemical and mechanical properties, even at single RBC level.

9
Conclusion

Raman Tweezers has revealed an extremely powerful analytical tool that provides physicist, chemist and biologists with a fingerprint of the agent they are studying and whose immense future applications are only now being fully understood. The technique holds all the promise of Raman spectroscopy, including the potential to identify almost any biological molecule and disease, and adds to it both a greater level of control and analytical capability as well as the capability of observing a sample in its natural state. As demonstrated in this work, Raman Tweezers is likely to surpass Raman spectroscopy in use for biological analysis.

However, even in single-particle experiments, background noise due to the environment can represent a serious obstacle for Raman spectroscopic analysis. In this thesis, it has been introduced a novel experimental method (*phase-sensitive*) which allows the acquisition of the Raman spectrum of a trapped object, free from any background contribution and which does not require any background subtraction procedure. In particular, the *phase-sensitive* method has been used to record Raman spectra of single polystyrene microbeads suspended in aqueous solution. In this work, it is reported a systematic characterization of the technique: it has been described in

detail the formation of the Raman signal and its dependence on several parameters, such as the height from the coverslip surface, the size of the bead, the amplitude of the spatial modulation of the trapped particle, and the pump laser intensity. The obtained results demonstrate that this method may find valuable applications in rapid sensing of biological samples in aqueous solutions.

The developed Raman Tweezers system has been used to characterize heterozygous red blood cells (RBCs), at single cell level. The study has been performed by analyzing the resonantly enhanced inelastic photons scattering from hemoglobin. Moreover, it has been investigated the cellular response to mechanical stress, by using a double-trap system (*optical stretcher*). In particular, in this work, it has been reported the results on the characterization of erythrocyte from normal and thalassemic volunteers. Some significant difference in the functionality of the thalassemic cells with respect to normal erythrocytes have been highlighted. In particular, the oxygenation capability of Hb has revealed to be reduced in thalassemic RBCs. The two kinds of cells also present a different response to photo-induced oxidative stress. The developed experimental technique has allowed to reconstruct, in addition, the distribution of Hb within the cell itself, avoiding the use of fluorescent labels. It has been, finally, measured the membrane shear modulus for thalassemic erythrocytes, which have revealed to be higher than 40 % with respect to healthy cells.

The results, shown in this thesis, confirm medical predictions regarding thalassemia, such as the reduced oxygenation capability of t-RBCs and their higher rigidity. Moreover they provide an interesting starting point to explore the application of a Raman Tweezers system in the analysis of others blood disorders. Unlike the traditional diagnostic tools, the applied approach is able to provide with the same apparatus both chemical and mechanical properties, even at single RBC level. That allows to extol heterogeneity, which is instead hidden by bulk-based techniques. The advantages of the Raman Tweezers system, developed in this thesis work, include the following:

- only a pinprick of blood is required for the analysis;

- the diagnosis is rapid, taking only a few seconds to acquire the RBC Raman spectrum;

- no staining or fixing to glass substrate is required, allowing RBCs analysis in

physiologically-relevant conditions;

- information on oxygenation state of the RBC can be obtained, at single cell level;

- both chemical and mechanical properties can be provided with same set-up.

As matter of fact, in vivo Raman micro-spectroscopy analysis combined with the use of Optical Tweezers offers enormous potential in the diagnosis and treatment of red blood cells disorders including thalassemia. It is up to biologists, however, to realize the full scope and magnitude of these applications and to press for the development of this seemingly unrelated technology in biomedicine.

Bibliography

[1] J. R. Baena; and B. Lendl, "Raman spectroscopy in chemical bioanalysis," *Curr. Opin. Chem. Biol.*, vol. 8, pp. 534–539, 2004.

[2] C. Xie; C. Goodman; M. A. Dinno; and Y.-Q. Li, "Real-time Raman spectroscopy of optically trapped living cells and organells," *Opt. Express*, vol. 12, pp. 6208–6214, 2004.

[3] K. Ramser; E. J. Bjerneld; C. Fant; and M. Kall, "Importance of substrate and photo-induced effects in Raman spectroscopy of single functional erythrocytes," *J. Biomed. Opt.*, vol. 8, pp. 173–178, 2003.

[4] A. Ashkin, "Acceleration and trapping of particles by radiation pressure," *Phys. Rev. Lett.*, vol. 24, pp. 156–159, 1970.

[5] A. Ashkin, "Trapping of atoms by resonance radiation pressure," *Phys. Rev. Lett.*, vol. 40, pp. 729–732, 1978.

[6] A. Ashkin; and J. M. Dziedzic, "Optical trapping and manipulation of viruses and bacteria," *Science*, vol. 2335, pp. 1517–1520, 1987.

[7] A. Ashkin; J. M. Dziedzic; and T. Yamane, "Optical trapping and manipulation of single cells using infrared laser beams," *Nature*, vol. 330, pp. 769–771, 1987.

[8] C. Xie; M. A. Dinno; and Y.-Q. Li, "Near-infrared raman spectroscopy of single optically trapped biological cells," *Opt. Lett.*, vol. 27, pp. 249–251, 2002.

[9] K. Ramser; K. Logg; M. Gokr; M. Kll; and D. Hanstorpn, "Resonance Raman spectroscopy of optically trapped functional erythrocytes," *J. Biomed. Opt.*, vol. 9, pp. 593Ű600, 2004.

[10] K. Ajito; and K. Torimitsu, "Laser trapping and Raman spectroscopy of single cellular organelles in the nanometric range," *Lab on Chip* , vol. 2, pp. 11–14, 2002.

[11] C. Xie; Y.-Q. Li; W. Tang; and R. J. Newton, "Study of dynamical process of heat denaturation in optically trapped single microorganisms by near-infrared Raman spectroscopy," *J. Appl. Phys.*, vol. 94, pp. 6138–6142, 2003.

[12] J. M. Sanderson; and A. D. Ward, "Analysis of liposomal membrane composition using Raman tweezers," *Chem Commun (Camb)*, vol. 7, pp. 1120–1121, 2004.

[13] L. Mitchem; J. Buajarern; A. D. Ward; J. P. Reid, "A Strategy for Characterising the Mixing State of Immiscible Aerosol Components and the Formation of Multiphase Aerosol Particles Through Coagulation," *J. Phys. Chem. B*, vol. 110, pp. 13700–13703, 2006.

[14] J. W. Chan; A. P. Esposito; C. E. Talley; C. W. Hollars; S. M. Lane; and T. Huser, "Reagentless identification of single bacterial spores in aqueous solution by confocal laser tweezers Raman spectroscopy," *Anal. Chem.*, vol. 76, pp. 599–603, 2004.

[15] D. P. Cherney; T. E. Bridges; and J. M. Harris, "Optical Trapping of Unilamellar Phospholipid Vesicles: Investigation of the Effect of Optical Forces on the Lipid Membrane Shape by Confocal-Raman Microscopy," *Anal. Chem.*, vol. 76, pp. 4920–4928, 2004.

[16] J. L. Deng; Q. Wei; M. H. Zhang; Y. Z. Wang; and Y.-Q. Li, "Study of the Effect of Alcohol on Single Human Red Blood Cells Using Near-infrared Laser Tweezers Raman Spectroscopy," *J. Raman Spectrosc.*, vol. 36, pp. 257–261, 2005.

[17] M. D. Mannie; T. McConnell; C. A. Xie; and Y.Q. Li, "Activation-dependent phases of T cells distinguished by use of optical tweezers and near infrared Raman spectroscopy," *J. Immunol. Methods*, vol. 297, pp. 53–60, 2005.

[18] B. R. Wood; B. Tait; and D. McNaughton, "Micro-Raman characterization of the R to T state transition of haemoglobin within a single living erythrocyte," *Biochim. Biophys. Acta.*, vol. 1539, pp. 58–70, 2001.

[19] B. R. Wood; and D. McNaughton, "Raman excitation wavelength investigation of single red blood cell in vivo," *J. Raman Spectrosc.*, vol. 33, pp. 517–523, 2002.

[20] K. Ramser; J. Enger; M. Gokr; D. Hanstorp; K. Logg; and M. Kll, "A microfluidic system enabling Raman measurements of the oxygenation cycle in single optically trapped red blood cells," *Lab. Chip*, vol. 5, pp. 431–436, 2005.

[21] I. P. Torres Filho; J. Terner; R. N. Pittman; L. G. Somera; and K. R. Ward, "Hemoglobin oxygen saturation measurements using resonance Raman intravital microscopy," *Am. J. Physiol. Heart Circ. Physiol.*, vol. 289, pp. 488–495, 2004.

[22] C. M. Creely; G. P. Singh; and D. Petrov, "Dual wavelength optical tweezers for confocal Raman spectroscopy," *Opt. Commun.*, vol. 245, pp. 465–470, 2005.

[23] M. J. Pelletier; and R. Altkorn, "Raman Sensitivity Enhancement for Aqueous Protein Samples Using a Liquid-Core Optical-Fiber Cell," *Anal. Chem.*, vol. 73, pp. 1393–1397, 2001.

[24] R. L. Mc Creery, "Raman Spectroscopy for Chemical Analysis, 3rd ed.," *John Wiley & Sons: New York*, 2000.

[25] G. Rusciano; A. C. De Luca; G. Pesce; and A. Sasso, "Phase-sensitive detection in Raman Tweezers," *Appl. Phys. Lett.*, vol. 89, pp. 261116–9, 2006.

[26] G. Rusciano; A. C. De Luca; G. Pesce; and A. Sasso, "Enhancing Raman Tweezers by Phase-Sensitive Detection," *Anal. Chem.*, vol. 79, pp. 3708–3715, 2007.

[27] A. Ashkin; and J. M. Dziedzic, "Optical levitation by radiation pressure," *Appl. Phys. Lett.*, vol. 19, pp. 283–285, 1971.

[28] K. Baldwin, "1997 Nobel Prize in physics goes to atom coolers," *Photonics Sci. News*, vol. 3, pp. 6, 1997.

[29] A. Ashkin; J. M. Dziedzic; J. E. Bjorkholm; and S. Chu, "Observation of a single-beam gradient force optical trap for dielectric particles," *Opt. Lett.*, vol. 11, pp. 288–290, 1986.

[30] T. Mayer; S. M. Barns; P. Rossnagel; R. Huber; S. Burggraf; and K. O. Stetter, "Isolation of a hyperthermophilic archaeum predicted by in situ RNA analysis," *Nature*, vol. 376, pp. 57–58, 1995.

[31] A. Ashkin, "Hystory of optical trapping and manipulation of small-neutral particle, atoms and molecules," *IEEE J. Sel. Top. Quantum Electron.*, vol. 6, pp. 841–856, 2000.

[32] A. Ashkin, "Forces of a single-beam gradient laser trap on a dielectric sphere in the ray optics regime," *Biophys. J.*, vol. 61, pp. 569–582, 1992.

[33] K. Svoboda; and S. M. Block, "Biological applications of optical forces," *Ann. Rev. Biophys. Struc.*, vol. 23, pp. 247–285, 1994.

[34] M. Kerker, "The scattering of light and other electromagnetic radiation," *New York, NY: Academic*, 1969.

[35] J. P. Barton; D. R. Alexander; and S. A. Schaub, "Internal and near-surphace electromagnetic fields for a spherical particle irradiated by a focused laser beam," *J. Appl. Phys.*, vol. 64, pp. 1632–1639, 1988.

[36] W. H. Wright; G. J. Sonek; and M. W. Berns, "Radiation trapping forces on microspheres with optical tweezers," *Appl. Phys. Lett.*, vol. 63, pp. 715–717, 1993.

[37] F. Gittes; and C. F. Scmidt, "Interference model for back-focal-plane displacement detection in optical tweezers," *Opt. Lett.*, vol. 23, pp. 7–9, 1998.

[38] W. M. Lee; P. J. Reece; R. F. Marchington; N. K. Metzger; and K. Dholakia, "Construction and calibration of an optical trap on a fluorescence optical microscope," *Nature Protocols*, vol. 2, pp. 3226–3238, 2007.

[39] A. Buosciolo; G. Pesce; and A. Sasso, "New calibration method for position detector for simultaneous measurements of force constants and local viscosity in optical tweezers," *Opt. Commun.*, vol. 230, pp. 357–368, 2003.

[40] D. G. Grier; and Y. Roichman, "Holographic optical trapping," *Appl. Opt.*, vol. 45, pp. 880–887, 2006.

[41] C. Hertlein; L. Helden; A. Gambassi; S. Dietrich; and C. Bechinger, "Direct measurement of critical Casimir forces," *Nature*, vol. 451, pp. 171–175, 2008.

[42] D. C. Benito; D. M. Carberry; S. H. Simpson; G. M. Gibson; M. J. Padgett; J. G. Rarity; M. J. Miles; and S. Hanna, "Constructing 3D crystal templates for photonic band gap materials using holographic optical tweezers," *Opt. Express*, vol. 175, pp. 13005–13015, 2008.

[43] C. Selhuber-Unkel; I. Zins; O. Schubert; C. Soennichsen; and L.B. Oddersheder, "Quantitative optical trapping of single gold nanorods," *Nano Lett.*, vol. 8, pp. 2998–3003, 2008.

[44] T. M. Hansen; S. N. S. Reihani; L. Oddershede; and M. Sørensen, "Correlation between mechanical strength of RNA pseudoknots and ribosomal frameshifting," *PNAS*, vol. 104, pp. 5830–5835, 2007.

[45] J. S. Dam; I. R. Perch-Nielsen; D. Palima; and J. Glückstad, "Three-dimensional imaging in three-dimensional optical multi-beam micromanipulation," *Opt. Express*, vol. 16, pp. 7244–7250, 2008.

[46] P. Galajda and; P. Ormos, "Complex micromachines produced and driven by light," *Appl. Phys. Lett.*, vol. 78, pp. 249–251, 2001.

[47] J. van Mameren; M. Modesti; R. Kanaar; C. Wyman; G.J.L. Wuite; and E.J.G. Petermans, "Dissecting elastic heterogeneity along DNA molecules coated partly with Rad51 using concurrent fluorescence microscopy and optical tweezers," *Biophys. J.*, vol. 91, pp. L78–L80, 2006.

[48] P. Jakl; T. Cizmar; M. Sery; and P. Zemanek, "Static optical sorting in a laser interference field," *Appl. Phys. Lett.*, vol. 92, pp. 1611101–3, 2008.

[49] F. Merenda; J. Rohner; J. M. Fournier; and R. P. Salathè, "Miniaturized high-NA focusing-mirror multiple optical tweezers," *Opt. Express*, vol. 15, pp. 6075–6086, 2007.

[50] G. Volpe; and D. V. Petrov, "Torque detection using Brownian fluctuations," *Phys. Rev. Lett.*, vol. 97, pp. 210603–210606, 2006.

[51] I. M. Tolic-Nørrelykke; L. Sacconi; C. Stringari; I. Raabel; and F. S. Pavone, "Nuclear and division plane positioning revealed by optical micromanipulation," *Curr. Biol.*, vol. 15, pp. 1212–1216, 2005.

[52] J. Baumgartl; M. Mazilu; and K. Dholakia, "Optically mediated particle clearing using Airy wavepackets," *Nature Photonics*, vol. 10, pp. 1–2, 2008.

[53] A. Ashkin; K. Sch*ü*tze; J. M. Dziedzic; U. Euteneuer; and M. Schliwa, "Force generation of organelle transport measured in vivo by an infrered laser trap," *Nature*, vol. 348, pp. 346–348, 1990.

[54] O. Vafa; T. Ord; R. H. Asch; Y. Tadir; W. H. Wright; and M. W. Berns, "Micromanip-ulation of sperm by a laser generated optical trap," *Fertility & Sterility*, vol. 52, pp. 870–873, 1989.

[55] S. M. Block; L. S. B. Goldstein; and B. J. Schnapp, "Bead movement by single kinesis molecules studied with optical tweezers," *Nature*, vol. 348, pp. 348–352, 1990.

[56] K. Svoboda; C. F. Schmidt; B. J. Schnapp; and S. M. Block, "Direct observation of kinesin stepping by optical trapping interferometry," *Nature*, vol. 365, pp. 721–727, 1993.

[57] K. Svoboda; and S. M. Block, "Force and velocity measured for single kinesin molecules," *Cell*, vol. 77, pp. 773–784, 1994.

[58] R. M. Simmons; J. T. Finer; and J. A. Spudich, "Single myosin molecule mechanics: piconewtons forces and nanometer steps," *Nature*, vol. 368, pp. 113–119, 1994.

[59] C. Cecconi; E. A. Shank; C. Bustamante; and S. Marqusee, "Direct observation of the three-state folding of a single protein molecule," *Science*, vol. 309, pp. 2057–2060, 2005.

[60] D. Collin; F. Ritort; C. Jarzynski; S. B. Smith; I. Tinoco; and C. Bustamante, "Verification of the Crooks fluctuation theorem and recovery of RNA folding free energies," *Nature*, vol. 437, pp. 231–234, 2005.

[61] P. T. X. Li; D. Collin; S. B. Smith; C. Bustamante; and I. Tinoco, "Proving the mechan-ical folding kinetics of TAR RNA by hopping, force-jump and force-ramp methods," *Biophys. J.*, vol. 90, pp. 250–260, 2006.

[62] K. Svoboda; R. Landick; S. M. Block; H. Yin; M. D. Wang; and J. Gelles, "Transcription against an applied force," *Science*, vol. 270, pp. 1653–1657, 1995.

[63] S. H*è*non; G. Lennomard; A. Richeta; and F. Gallet, "A new determination of the shear modulus of the human erythrocyte membrane using optical tweezers," *Biophys. J.*, vol. 76, pp. 1145–1151, 1999.

[64] M. W. Berns; K. Konig; Y. Liu; G. J. Sonek; and B. J. Tromberg, "Two-photon fluorescence excitation in continuous-wave infrared optical tweezers," *Opt. Lett.*, vol. 20, pp. 2246–2248, 1995.

[65] N. Kitamura; H.-B. Kim; S. Habuchi; and M. Chiba, "Space- and time-resolved spectroscopic analyses in micrometre dimensions," *Trends Anal. Chem.*, vol. 18, pp. 675–684, 1999.

[66] C. V. Raman; and K. S. Krishnan, "A New Type of Secondary Radiation," *Nature*, vol. 121, pp. 501–502, 1928.

[67] G. Landsberg; and L. Mandelstam, "A novel effect of light scattering in crystals," *Naturwissenchaften*, vol. 16, pp. 557–558, 1928.

[68] T. G. Spiro, "Resonance Raman spectroscopy as a probe of heme protein structure and dynamics," *Adv. Protein Chem.*, vol. 37, pp. 111, 1985.

[69] H. Kataoka; S. Maeda; and C. Hirose, "Effects of Laser Linewidth on the Coherent Anti-Stokes Raman Spectroscopy Spectral Profile," *Appl. Spectrosc.*, vol. 36, pp. 565, 1982.

[70] M. Braiman; and R. Mathies, "Resonance Raman spectra of bacteriorhodopsin's primary photoproduct: evidence for a distorted 13-cis retinal chromophore," *PNAS*, vol. 79, pp. 403, 1982.

[71] A. Mahadevan-Jansen; and R. R. Richards-Kortum, "Raman spectroscopy for the detection of cancers and precancers," *J. Biomed. Opt.*, vol. 1, pp. 31, 1996.

[72] J. Duguid; V. A. Bloomfield; J. Benevides; and G. J. Thomas, "Raman spectroscopy of DNA-metal complexes. I. Interactions and conformational effects of the divalent cations: Mg, Ca, Sr, Ba, Mn, Co, Ni, Cu, Pd, and Cd," *Biophys. J.*, vol. 65, pp. 1916, 1993.

[73] G. J. Puppels; F. F. M. de Mul; C. Otto; J. Greve; M. Robert-Nicoud; D. J. Arndt-Jovin; and T. M. Jovin, "Studying single living cells and chromosomes by confocal Raman microspectroscopy," *Nature*, vol. 347, pp. 301, 1990.

[74] M. G. Shim; B. C. Wilson; E. Marple; and M. Wach, "Study of Fiber-Optic Probes for in Vivo Medical Raman Spectroscopy," *Appl. Spectrosc.*, vol. 53, pp. 619, 1999.

[75] A. Jorio; R. Saito; J. H. Hafner; C. M. Lieber; M. Hunter; T. McClure; G. Dresselhaus; and M. S. Dresselhaus, "Structural (n,m) Determination of Isolated Single-Wall Carbon Nanotubes by Resonant Raman Scattering," *Phys. Rev. Lett.*, vol. 86, pp. 1118, 2001.

[76] S. Walker; and H. Straw, "Spectroscopy2: Ultra-violet, vVisible, Infra-red and Raman spectroscopy," *London: Chapman & Hall*, 1962.

[77] W. Demtröder, "Laser spectroscopy," *Springer*, 1996.

[78] R. Loudon, "The quantum theory of light," *Clarendon press-Oxford*, 1997.

[79] G. Herzberg, "Molecular Spectra and Molecular structure," *van Nostrand Reinhold, New York*, 1945.

[80] A. Weber, "Raman spectroscopy of gases and liquids," *Topics Curr. Phys., Springer*, vol. 11, 1979.

[81] S. A. Asher, "UV resonace Raman studies of molecular structures and dynamics," *Ann. Rev. Phys. Chem.*, vol. 39, pp. 537–588, 1988.

[82] I. Itzkan; R. R. Dasari; K. Kneipp; H. Kneipp; and M. S. Feld, "Ultrasensitive Chemical Analysis by Raman Spectroscopy," *Chem. Rev.*, vol. 99, pp. 2957–2975, 1999.

[83] A. J. McQuillan; M. Fleishman; and P. J. Hendra, " Raman spectra of pyridine adsorbed at a silver electrode," *J. Chem. Phys. Lett.*, vol. 26, pp. 163–168, 1974.

[84] K. Kneipp; L. T. Perelman; I. Itzkan; R. R. Dasari; H. Kneipp; Y. Wang; and M. S. Feld, "Single Molecule Detection Using Surface-Enhanced Raman Scattering (SERS)," *Phys. Rev. Lett.*, vol. 78, pp. 1667–1670, 1996.

[85] V. B. Kartha; R. Manoharan; G. Deinum; I.Itzkan; R. R. Dasari; K. Kneipp; H. Kneipp; and M. S. Feld, "Detection and identification of a single DNA base molecule using surface-enhanced Raman scattering (SERS)," *Phys. Rev. E*, vol. 57, pp. R6281–R6284, 1998.

[86] I.Itzkan; R. R. Dasari; K. Kneipp; H. Kneipp; and M. S. Feld, "Surface-enhanced non-linear Raman scattering at the single- molecule level," *Chem. Phys.*, vol. 247, pp. 155–162, 1999.

[87] Otto A., "Theory of first layer and single molecule surface enhanced Raman scattering (SERS)," *Phys. Stat. Sol. (a)*, vol. 188, pp. 1455–1458, 2001.

[88] M. Moskovits, "Surface-enhanced Raman spectroscopy: a brief retrospective," *J. Raman. Spectrosc.*, vol. 36, pp. 485–496, 2005.

[89] I. Itzkan; R. R. Dasari; K. Kneipp; H. Kneipp; and M. S. Feld, "Surface-enhanced Raman scattering and biophysics," *J. Phys.: Condens. Matter*, vol. 14, pp. R597–R624, 2002.

[90] D. S. Wang; and M. Kerker, "Enhanced Raman scattering by. molecules at the surface of colloidal spheroids," *Phys. Rev. B*, vol. 24, pp. 1777–1790, 1981.

[91] M. Kall; H. X. Xu; J. Aizpurua; and P. Apell, "Electromagnetic contributions to single-molecule sensitivity in surface-enhanced Raman scattering," *Phys. Rev. E*, vol. 62, pp. 4318–4324, 2000.

[92] C. Otto; N. M. Sijtsema; and J. Greve, "Confocal Raman microspectroscopy of the activation of single neutrophilic granulocytes," *Eur. Biophys. J.*, vol. 27, pp. 582–589, 1998.

[93] L. P. Choo-Smith; H. G. Edwards; H. P. Endtz; J. M. Kros; F. Heule; H. Barr; J. S. Jr Robinson; H. A. Bruining; and G. J. Puppels, "Medical applications of Raman spectroscopy: from proof of principle to clinical implementation," *Biopolymers*, vol. 67, pp. 1–9, 2002.

[94] G. J. Puppels; H. S. Garritsen; G. M. Segers-Nolten; F. F. de Mul; and J. Greve, "Raman microspectroscopic approach to the study of human granulocytes," *Biophys. J.*, vol. 60, pp. 1046–1050, 1991.

[95] R. Thurn; and W. Kiefer, "Raman-microsampling technique applying optical levitation by radiation pressure," *Appl. Spectrosc.*, vol. 38, pp. 78–86, 1984.

[96] M. A. Dinno; Y. Q. Li; W. Tang; R. J. Newton; C. Xie; J. Mace; and P. J. Gemperline, "Identification of single bacterial cells in aqueous solution using confocal laser tweezers Raman spectroscopy," *Anal. Chem.*, vol. 77, pp. 4390–4397, 2005.

[97] K. Ajito, "Combined Near-Infrared Raman microprobe and laser Ttrapping system: application to the analysis of a single organic microdroplet in water," *Appl. Spectrosc.*, vol. 52, pp. 339–342, 1998.

[98] K. Ajito; C. Han; and K. Torimitsu, "Detection of glutamate in optically trapped single nerve terminals by Raman spectroscopy," *Anal. Chem.*, vol. 76, pp. 2506–2510, 2004.

[99] J. W. Chan; D. S. Taylor; S. M. Lane; T. Zwerdling; J. Tuscano; and T. Huser, "Nondestructive identification of individual leukemia cells by laser trapping Raman spectroscopy," *Anal. Chem.*, vol. 80, pp. 2180–2187, 2008.

[100] A. Y. Lau; L. P. Lee; and J. W. Chan, "An integrated optofluidic platform for Raman-activated cell sorting," *Lab Chip*, vol. 8, pp. 1116–1120, 2008.

[101] M. P. Houlne; C. M. Sjostrom; R. H. Uibel; J. A. Kleimeyer; and J. M. Harris, "Confocal Raman microscopy for monitoring chemical reactions on single optically trapped, solid-phase support particles," *Anal. Chem.*, vol. 74, pp. 4311–4319, 2002.

[102] P. Rosch; M. Schmitt; R. Petry; W. Kiefer; M. Lankers; R. Gessner; C. Winter; and J. Popp, "Identification of biotic and abiotic particles by using a combination of optical tweezers ans in sutu Raman spectroscopy," *Chem. Phys. Chem.*, vol. 5, pp. 1159–1170, 2004.

[103] D. Smith; M. Mazilu; L. Paterson; A. Riches; C. S. Herrington; W. Sibbett; P. R. T. Jess; V. Garces-Chavez; and K. Dholakia, "Dual beam fibre trap for Raman microspectrocopy of single cells," *Opt. Express*, vol. 14, pp. 5759–5791, 2006.

[104] K. E. Hamden; B. A. Bryan; P. W. Ford; C. Xie; Y.-Q. Li; and S. M. Akula, "Spectroscopic analysis of Kaposi's sarcoma-associated herpesvirus infected cells by Raman tweezers," *J. Virol. Methods*, vol. 129, pp. 145–151, 2005.

[105] C. A. Xie; and Y.-Q. Li, "Confocal micro-Raman spectroscopy of single biological cells using optical trapping and shifted excitation difference techniques," *J. Appl. Phys.*, vol. 93, pp. 2982–2986, 2003.

[106] C. Xie; D. Chen; and Y.-Q. Li, "Raman sorting and identification of single living microorganisms with optical tweezers," *Opt. Lett.*, vol. 30, pp. 1800–1802, 2005.

[107] J. F. Ojeda; C. Xie; Y. Q. Li; F. E. Bertrand; J. Wiley; and T. J. McConnel, "Chromosomal analysis and identification based on optical tweezers and Raman spectroscopy," *Opt. Express*, vol. 14, pp. 5385–5393, 2006.

[108] C. M. Creely; G. Volpe; G. P. Singh; M. Soler; and D. Petrov, "Raman imaging of floating cells," *Opt. Express*, vol. 13, pp. 6105–6110, 2005.

[109] C. Xie; J. Mace; M. A. Dinno; Y. Q. Li; W. Tang; R. J. Newton; and P. J. Gemperline, "Identification of Single Bacterial Cells in Aqueous Solution Using Confocal Laser Tweezers Raman Spectroscopy," *Anal. Chem.*, vol. 77, pp. 4390–4397, 2005.

[110] M. Minsky, "Memoir on inventing the confocal microscope," *Scanning*, vol. 10, pp. 128–138, 1988.

[111] D. Semwogerere; and E. R. Weeks, "Confocal microscopy," *Encyclopedia of Biomaterials and Biomedical Engineering, Taylor and Francis*, 2005.

[112] R. H. Webb, "Confocal optical microscopy," *Rep. Prog. Phys.*, vol. 59, pp. 427–471, 1996.

[113] T. E. Bridges; M. P. Houlne; and J. M. Harris, "Spatially Resolved Analysis of Small Particles by Confocal Raman Microscopy: Depth Profiling and Optical Trapping," *Anal. Chem.*, vol. 76, pp. 576–584, 2004.

[114] B. Richards; and E. Wolf, "Electromagnetic diffraction in optical systems II. Structure of the image field in an aplanatic system," *Proc. R. Soc. A*, vol. 253, pp. 358–379, 1959.

[115] K. A. Rubinson; and J. F. Rubinson, "Contemporary instrumental analysis," *Upper Saddle River, NJ: Prentice Hall*, 2000.

[116] J. E. Curtis; B. A. Koss; and D. G. Grier, "Dynamic holographic optical tweezers," *Opt. Commun.*, vol. 207, pp. 169–175, 2002.

[117] R. L. Mc Creery, "Raman Shift Frequency Standards: Polystyrene," *http://www.chemistry.ohio-state.edu/~rmccreer/freqcorr/images/poly.html*.

[118] S. Inou*é*; and K. R. Spring, "Video Microscopy," *Plenum Press: New York*, 1997.

[119] T. E. Bridges; M. P. Houlne; and J. M. Harris, "Measuring Diffusion of Molecules into Individual Polymer Particles by Confocal Raman Microscopy," *An. Chem.*, vol. 78, pp. 2121–2129, 2006.

[120] K. A. Rubinson; and J. F. Rubinson, "Contemporary Instrumental Analysisy," *Prentice Hall: Upper Saddle River, NJ*, 2000.

[121] E. L. Theofanidou; W. J. Wilson; and J. Hossack, "Spherical aberration correction for optical tweezers," *Opt. Commun.*, vol. 236, pp. 145–150, 2004.

[122] A. Rohrbach; and E. H. K. Stelzer, "Trapping forces, force constants, and potential depths for dielectric spheres in the presence of spherical aberrations," *Appl. Opt.*, vol. 41, pp. 2494–2507, 2002.

[123] E. L. Florin; A. Pralle; E. H. K. Stelzer; J. K. H. Horber, "Local viscosity probed by photonic force microscopy ," *Appl. Phys. A*, vol. 66, pp. S71–S73, 1998.

[124] B. R. Wood; P. Caspers; G. J. Pupples; S. Pandiancherri; and D. McNaughton, "Resonance Raman Spectroscopy of red blood cell using near-infrared laser excitation," *Anal. Bioanal. Chem.*, vol. 387, pp. 1691–1703, 2007.

[125] H. Brunner; A. Mayer; and H. Sussnerr, "Resonance Raman Scattering on the heam group of the oxy- and deoxyhaemogloin," *J. Mol. Biol.*, vol. 70, pp. 153–156, 1972.

[126] A. C. De Luca; G. Rusciano; R. Ciancia; V. Martinelli; G. Pesce; B. Rotoli; L. Selvaggi; and A. Sasso, "Spectroscopical and mechanical characterization of normal and thalassemic red blood cells by Raman Tweezers," *Opt. Express*, vol. 16, pp. 7943–7957, 2008.

[127] A. C. De Luca; G. Rusciano; R. Ciancia; V. Martinelli; G. Pesce; B. Rotoli; and A. Sasso, "Resonance Raman spectroscopy and mechanics of single red blood cell manipulated by optical tweezers," *Haematologica*, vol. 92, pp. 174–175, 2007.

[128] A. C. De Luca; and G. Rusciano, "Monitoring cellular disease by Raman Tweezers," *Nuovo Cimento B*, vol. 122B, pp. 731–738, 2008.

[129] M. Abe; T. Kitagawa; and Y. Kyogoku, "Resonance Raman spectra of octaethylporphyrinato-Ni(II) and mesodeuterated and 15N substituted derivatives. II. A normal coordinate analysis," *J. Chem. Phys.*, vol. 69, pp. 4526–4531, 1978.

[130] S. Hu; K. M. Smith; and T. G. Spiro, "Assignment of protoheme resonance Raman spectrum by heme labeling in myoglobin," *J. Am. Chem. Soc.*, vol. 118, pp. 12638–12646, 1996.

[131] I. Kahane; A. Shifter; and E. A. Rachmilewitz, "Cross linking of red blood cells membrane proteins induced by oxidative stress in beta-thalassemia," *FEBS Lett.*, vol. 85, pp. 267–270, 1978.

[132] E. A. Rachmilewitz; B. M. Lubin; and S. B. Shohet, "Lipid membrane peroxidation in beta-thalassemia," *Blood*, vol. 47, pp. 495–505, 1976.

[133] E. Shinar; E. A. Rachmilewitz; and S. E. Lux, "Differing erythrocyte membrane skeletal protein defects in alpha and beta thalassemia," *J. Clin. Invest.*, vol. 83, pp. 404–410, 1989.

[134] N. Uzunbajakava; A. Lenferink; Y. Kraan; B.Willekens; G. Vrensen; J. Greve; and C. Otto, "Nonresonant Raman imaging of protein distribution in single human cells," *Biopolymers*, vol. 72, pp. 1–9, 2001.

[135] Y. Park; G. Popescu; K. Badizadegan; R. R. Dasari; and M. S. Feld, "Diffraction phase and fluorescence microscopy," *Opt. Express*, vol. 14, pp. 8263–8268, 2006.

[136] B. Williams, "Hematology, sixth edition," *McGraw-Hill, New York*, 2001.

[137] S.K. Boey; D. H. Boal; and D. E. Discher, "Simulations of the erythrocyte cytoskeleton at large deformation I. Microscopic models," *Biophys. J.*, vol. 75, pp. 1573–1583, 1998.

[138] D. E. Discher; D. H. Boal; and S.K. Boey, "Simulations of the erythrocyte cytoskeleton at large deformation. II. Micropipette aspiration," *Biophys. J.*, vol. 75, pp. 1584–1597, 1998.

[139] J. Li; M. Dao; C. T. Lim; and S. Suresh, "Spectrin-level modeling of the cytoskeleton and optical tweezers stretching of the erythrocyte," *Biophys. J.*, vol. 88, pp. 3707–3719, 2005.

[140] G. Lenormand; S. Hénon; A. Richert; and F. Galleth, "Direct measurement of the area expansion and shear moduli of the human red blood cell membrane skeleton," *Biophys. J.*, vol. 81, pp. 43–56, 2001.

[141] S. Hénon; G. Lenormand; A. Richert; and F. Gallet, "A new determination of the shear modulus of the human erythrocyte membrane using optical tweezers," *Biophys. J.*, vol. 76, pp. 1145–1151, 1999.

[142] E. A. Evans, "A new membrane concept applied to the analysis of fluid shear- and micropipette-deformed red blood cells," *Biophys. J.*, vol. 13, pp. 941–954, 1973.

[143] D. J. Weatherall; and J. B. Clegg, "Thalassemia revisited," *Cell*, vol. 29, pp. 7–9, 1982.

[144] G. Athanasiou; N. Zoubos; and Y. Missirlis, "Erytrhrocyte membrane deformability in patients with thalassemia syndromes," *Nouv. Rev. Fr. Hematol.*, vol. 33, pp. 15–20, 1991.

Part IV

List of Publications

Publications related to the work described in this thesis

1. G. Rusciano, <u>A. C. De Luca</u>, G. Pesce and Sasso A. "Phase-sensitive detection in Raman Tweezers" *Appl. Phys. Lett.* **89**, 261116 (2006).

Abstract:

We discuss on a method to acquire the Raman spectrum of a single optically trapped particle. The method makes use of two laser beams: one laser traps the particle and moves it back and forth in a plane perpendicular to the laser beam propagation; a second laser acts as Raman probe and it is fixed in space. The Raman spectrum is obtained by phase detecting the back-scattered Raman photons using a lock-in amplifier. Within this approach, the background due to the scattering of the environment is completely removed. We apply this method to 4.25 μm-diameter polystyrene beads in aqueous solution.

2. G. Rusciano, <u>A. C. De Luca</u>, G. Pesce and Sasso A. "Enhancing Raman Tweezers by Phase-Sensitive Detection" *Anal. Chem.* **79**, 3708 (2007).

Abstract:

Raman spectroscopy has become a powerful tool for microscopic analysis of organic and biological materials. When combined with optical tweezers (Raman tweezers), it allows investigating single, selected micrometric particles in their natural environment, therefore, reducing unwanted interferences from the cover plate. A general problem affecting both Raman spectrometers and Raman tweezers systems is the background caused by the environment surrounding the sample under investigation.

In this paper, we report on a novel method that allows acquiring Raman spectra of a single trapped particle (polystyrene microspheres) free from any background contribution. The method is based on the use of two collinear and copropagating laser beams: the first is devoted to trapping (trap laser), while the second one is used to excite the Raman transitions (pump laser). The trap

laser moves the trapped particle periodically, by means of a galvomirror, back and forth across the pump laser. The back-scattered photons are analyzed by a spectrometer and detected by a photomultiplier; finally, the resulting signal is sent to a lock-in amplifier for phasesensitive detection. The purpose of the present work is to give a detailed description of our method and to supply a systematic study concerning the formation of the Raman signal. We trap polystyrene beads and study the dependence of the Raman signal on several parameters, such as height from the coverslip surface, the bead size, the modulation amplitude, and the pump laser intensity. Our results establish a direct and practical approach for background suppression in the spectroscopic analysis of optical trapped microsized samples.

3. A. C. De Luca, G. Rusciano, R. Ciancia, V. Martinelli, G. Pesce, B. Rotoli and A. Sasso "Resonance Raman spectroscopy and mechanics of single red blood cell manipulated by optical tweezers" *Haematologica* **92**, 174 (2007).

Abstract:

The analysis of single cell in a physiological environment is a challenging topic for many biomedical applications. Optical Tweezers (OT) have revealed to be a quite useful tool to monitor address this issue. Based on the use of a strongly focused laser beam, they allow trapping and manipulation of microsized objects in absence of mechanical contact.

An interesting aspect of optical tweezers is that they can be integrated and combined with different imaging systems and spectroscopic techniques. Among this, vibrational Raman spectroscopy, i.e. inelastic light scattered from vibrational modes, is an attractive optical method, providing direct access to the identity and relative concentration of molecules. We have developed a Raman tweezers system to characterize red blood cells (RBCs) from both healthy and beta-thalassemic volunteers. The obtained results are quite promising for the development of new clinical protocols for the diagnosis of Thalassaemia.

4. <u>A. C. De Luca</u>, G. Rusciano, R. Ciancia, V. Martinelli, G. Pesce, B. Rotoli and A. Sasso "Spectroscopical and Mechanical Characterization of Normal and Thalassemic Red Blood Cells by Raman Tweezers" *Opt. Express* **16**, 7943 (2008).

Abstract:

In this work, the effects of thalassemia, a blood disease quite diffuse in the Mediterranean sea region, have been investigated at single cell level using a Raman Tweezers system. By resonant excitation of hemoglobin Raman bands, we have examined the oxygenation capability of β-thalassemic erythrocytes. A reduction of this fundamental erythrocyte function has been found. The measurements have been performed on a significant number of red blood cells; the relative statistical analysis is presented. Moreover, the response to photo-induced oxidative stress of diseased cells with respect to the normal ones has been analyzed. Finally, the deformability of thalassemic erythrocytes has been quantified by measuring the membrane shear modulus by using a double-trap system: the measurements have revealed an increase in membrane rigidity of more than 40%, giving evidence that the genetic defect associated to thalassemia, which manly relies on hemoglobin structure, also strongly affects the erythrocyte mechanical properties. Our results demonstrate that the developed set-up may have potential for the monitoring of blood diseases and their response to drug therapies.

- Also included in the *Virtual Journal of Biomedical Optics* 3, n.6 (2008).
- Highlighted in the *Optics and Laser Europe Magazine*.

5. <u>A. C. De Luca</u> and G. Rusciano "Monitoring cellular disease by Raman Tweezers" *Nuovo Cimento B* **122B**, 731 (2008).

Abstract:

We present a spectroscopic analysis of Red Blood Cells (RBCs). The analysis was carried out at the level of single cells, which were optically trapped by means of a near-infrared laser (λ = 1064 nm). Resonance Raman excitation of hemoglobin (Hb) was performed with a second laser, emitting at λ = 532

nm. The aim of this study is to compare the Raman response of normal RBCs with thalassemic cells. Raman analysis is used to draw hemoglobin distribution inside single erythrocytes. In particular, the experimental outcomes reveal the characteristic anomaly (target shape) occurring in thalassemia. These results in vivo show the potential of our technique as a diagnostic tool for other hemopathies.

6. G. Rusciano, <u>A. C. De Luca</u>, G. Pesce and A. Sasso "Raman Tweezers as diagnostic tool of hemoglobin-related blood disorders" *Sensors* **(submitted)**

Abstract:

This review presents the development of a Raman Tweezers system for detecting, at single cell level, hemoglobin-related blood disorders. The study demonstrates that the molecular fingerprint insight provided by Raman analysis holds great promise in the field of biomedicine for distinguishing between healthy and diseased cells. Herein a Raman Tweezers system has been applied to investigate the effects of thalassemia, a blood disease quite diffuse in the Mediterranean sea region. By resonant excitation of hemoglobin Raman bands, we examined the oxygenation capability of normal, alpha- and beta-thalassemic erythrocytes. A reduction of this fundamental red blood cell function, particularly severe for beta-thalassemia, has been found. Raman spectroscopy was also used to draw hemoglobin distribution inside single erythrocytes; the results confirmed the characteristic anomaly (target shape), occurring in thalassemia and some other blood disorders. The success of resonance Raman spectroscopy for thalassemia detection reported in this review provide an interesting starting point to explore the application of a Raman Tweezers system in the analysis of several blood disorders.

Other publications:

7. G. Rusciano, <u>A. C. De Luca</u>, F. Pignatiello, and A. Sasso "Doppler-free spectroscopy of xenon in the mid-infrared using difference-frequency radiation" *Opt. Express* **13**, 8357 (2005).

Abstract:

We report on the first Doppler-free spectroscopy investigation of an atomic species, xenon, performed in the mid-infrared using difference-frequency radiation. The absorption saturated spectrum of the xenon $6p[3/2]_2 \rightarrow 5d[5/2]_3$ transition ($2p_6 \rightarrow 3d'_1$ in Paschen notation) at 3.1076 μm was investigated using about 60 microwatts of cw narrowband radiation ($\Delta\nu$=50 kHz) generated by difference-frequency mixing in a periodically-poled Lithium Niobate crystal. A single frequency Ti:Sapphire laser (power 800 mW) and a monolithic diode-pumped Nd:YAG laser (300 mW) were used as pump and signal waves respectively. We used natural enriched xenon, which contains nine stable isotopes, two of which, ^{129}Xe and ^{131}Xe, exhibit a hyperfine structure owing to their nuclear spin. The small isotope displacements expected for this atom and the complex hyperfine structure of the odd isotopes make it difficult to fully resolve the recorded saturated-absorption spectra. In spite of this, we have been able to analyze the isolated ^{129}Xe $F'' = 5/2 \rightarrow F' = 7/2$ hyperfine component by means of first-derivative FM spectroscopy.

8. <u>A. C. De Luca</u>, G. Pesce, G. Rusciano and A. Sasso "Detection of HCl and HF by TTFMS and high frequency WMS" *Spectrochimica Acta Part A* **63**, 923 (2006).

Abstract:

In this work we discuss on a compact spectrometer based on DFB diode lasers for detection of chloridric and fluoridric acids. HCl and HF concentrations are determined through optical absorption of the P(4) line (λ= 1.7 μm) and the R(3) line (λ= 1.3μm), respectively. Both lines belong to first overtone vibrational bands and their linestrengths are $7.8 \cdot 10^{-21}$ cm/molecule for HCl and $2.8 \cdot 10^{-20}$ cm/molecule for HF. We chose these lines for their relative high

intensities and because they are quite far from water vapour lines which represent the main interfering gas for trace-gases analysis. To detect these species we used two different high frequency modulation techniques: two-tone frequency modulation spectroscopy (f_1 = 800MHz and f_2 = 804 MHz) was used for HCl while for HF we followed a simpler approach based on wavelength modulation spectroscopy (f = 600 kHz).We demonstrate that the two techniques provide comparable detection limit of about 80 ppbV at atmospheric pressure. Positive testing of our spectrometer makes it suitable for in situ measurements of exhaust gases coming from waste incinerators.

9. A. C. De Luca, G. Volpe, A. Morales, M. I. Geli, G. Pesce, G. Rusciano, A. Sasso and D. Petrov "Real-time actin-cytoskeleton depolymerization detection in a single cell using optical tweezers" *Opt. Express* **15**, 7922 (2007).

Abstract:

The cytoskeleton provides the backbone structure for the cellular organization, determining, in particular, the cellular mechanical properties. These are important factors in many biological processes, as, for instance, the metastatic process of malignant cells. In this paper, we demonstrate the possibility of monitoring the cytoskeleton structural transformations in optically trapped yeast cells (Saccharomyces cerevisiae) by tracking the forward scattered light via a quadrant photodiode. We distinguished normal cells from cells treated with latrunculin A, a drug which is known to induce the actin-cytoskeleton depolymerization. Since the proposed technique relies only on the inherent properties of the optical trap, without requiring external markers or biochemical sensitive spectroscopic techniques, it can be readily combined with existing optical tweezers setups.

10. A. C. De Luca, G. Rusciano, S. Guido, S. Caserta, G. Pesce and A. Sasso "Diffusion in polymer blends by Raman microscopy" *Macromolecules* **41B**, 5512 (2008).

Abstract:

In this work, we tackle the problem of diffusion in polymer blends by using Raman microscopy. In particular, we have investigated the concentration profiles of the diffusing species outside a micron-sized droplet of the dispersed phase, by using a micro-Raman optical set-up. This approach allows the investigation of the diffusion process, occurring at a micrometric scale, in a polymer blend of two "immiscible" phases (the polyisobutylene/poly-dimethylsiloxane pair). In our case, we have measured the concentrations in the mixture due to molecular diffusion as a function of both time and distance from the droplet interface, in a geometry which has a close correspondence to the actual microstructure of a polymer blend.

- Highlighted in *Optics & Photonics Focus* (www.opfocus.org).

11. G. Rusciano, <u>A. C. De Luca</u>, A. D'Alessio, P. Minutolo, G. Pesce and A. Sasso "Surface Enhanced Raman Scattering study of nano-sized organic carbon particles produced in combustion processes" *Carbon* **46**, 335 (2008).

Abstract:

Surface-enhanced Raman scattering (SERS) has been employed for the first time to characterize nano-sized organic carbon (NOC) particles produced in ordinary combustion processes. Ag-coated glass microparticles, used as SERS substrate, provide a Raman scattering cross section enhancement up to five orders of magnitude, which allows sample investigation at low concentration level. The observed spectral features supply a deeper insight on the chemical properties of the investigated combustion product. In addition, the high sensitivity of the SERS technique might be useful to test and characterize the toxicity of NOC particles.

- Also included in the *Virtual Journal of Nanotechnology Environment, Health and Safety* n.2 (2008).

12. G. Pesce, <u>A. C. De Luca</u>, G. Rusciano, P. Netti, S. Fusco, A. Sasso "Microrheol-ogy of complex fluids using optical tweezers: comparison with macrorheologic measurements"*J. Opt. A: Pure Appl. Opt.* **(In press)**

Abstract:

The increasing interest for investigating complex systems at mesoscopic scale has opened to new experimental techniques usually indicated as microrhe-ology. Unlike bulk-based approaches (macrorheology) these new techniques make use of micrometric probes (usually microspheres) which explore the me-chanical properties of the surrounding medium. In this paper we discuss the basic idea of microrheology and we will focus on one specific technique based on Optical Tweezers. Our discussion starts from Newtonian fluids to tackle the more general case of complex fluids (hyaluronic acid solutions in this paper). A part Optical Tweezers we use also a macrorheological technique in order to compare micro- and macro-responses and to verify the reliability and comple-mentarity's of OT.

In this work we study the viscoelastic properties of low molecular weight HA (155 KDa) at low ionic strength over an extended frequency range (0.1-1000 Hz) and in a wide range of concentrations (0.01-20 mg/ml). This excursion crosses the transition from dilute to semi-dilute regime. In the interval of concentra-tions here explored and within the frequency range covered by our techniques samples prevalently exhibit a viscous behavior while the elastic contribution becomes significant at high concentrations. We find good agreement between the macro and micro-rheological techniques used in our investigation although they cover different frequency ranges.

Submitted paper:

13. <u>A. C. De Luca</u>, A. Jonas, G. Rusciano, G. Pesce, S. Guido and A. Sasso "Diffusive mixing of polymers investigated by Raman microspectroscopy and microrhe-ology" *Soft Matter* **(submitted)**

14. G. Pesce, L. Selvaggi, <u>A. C. De Luca</u>, G. Rusciano, L. Santella and A. Sasso "Viscoelastic studies in living starfish oocytes by laser and video tracking" *Biophys. J.* **(submitted)**

15. G. Rusciano, <u>A. C. De Luca</u>, G. Pesce and A. Sasso "Study of the interaction of carbon-based nanoparticles with lipid membranes by using Optical Tweezers and SERS spectroscopy" *PNAS* **(submitted)**

Appendix

```
%%%%%%%%%%%%%%%%%%%%%%%%%%%%%%%%%%%%%%%%%%%%%%%%%%%
Raman signal generated by the Monte Carlo simulation
at the modulation amplitude A = 0.5
%%%%%%%%%%%%%%%%%%%%%%%%%%%%%%%%%%%%%%%%%%%%%%%%%%%


r = 1;      "sphere radius"
f =35;    "oscillation frequency"
wk=0.534;  "parameters of beam profile"
zk=3.14*(wk)^2/0.532;
Aj=0.5;    "modulation amplitude"
cont1 = zeros(1,29);        "HIT"
tnoc1 = zeros(1,29);        "MISS"
N=10000000;
for t=1:29
y0= Aj*sin(2*pi*f*t);
for i=1:N
x =rand*2*r-r;
y= rand*2*r-r+y0;
z= rand*2*r-r;
if x^2 + (y-y0).^2 +z^2 < r^2   "sphere control"
if x^2+y^2 < (wk/2)^2*(1+(z/zk)^2)    "beam profile control"
cont1(t) = cont1(t) + 1;
else
if x^2+y^2 < (wk)^2*(1+(z/zk)^2) & x^2+y^2>(wk/2)^2*(1+(z/zk)^2)
cont1(t) = cont1(t) + (0.78)^2;
```

```
else
if x^2+y^2 < (3*wk/2)^2*(1+(z/zk)^2) & x^2+y^2>(wk)^2*(1+(z/zk)^2)
cont1(t) = cont1(t) + (0.36)^2;
else
if x^2+y^2 < (2*wk)^2*(1+(z/zk)^2) & x^2+y^2>(3*wk/2)^2*(1+(z/zk)^2)
cont1(t) = cont1(t) + (0.10)^2;
else
continue
      end
     end
    end
   end
  end
 end
end
cont1=cont1/N;
plot(cont1)


%%%%%%%%%%%%%%%%%%%%%%%%%%%%%%%%%%%%%%%%%%%%%%%%%%%
Raman signal as function of the modulation amplitude,
the beam waist is a free parameter
%%%%%%%%%%%%%%%%%%%%%%%%%%%%%%%%%%%%%%%%%%%%%%%%%%%


f=input('Which file analyze?: ','s');
wmin=input('Wo min: ');
wmax=input('Wo max: ');
p=input('step: ');
np=(wmax-wmin)/p;
npp=int8(np)+1;
%Experimental file
F=load(f);
X=F(:,1);
Y=F(:,2);
nf=max(Y);
```

```
Yn=Y/nf;
l=length(X);
r = 2;    "Sphere radius"
f =1/60;    "Oscillation frequency"
xgm = X(l)+1;
for k=1:npp
wk=wmin+(k-1)*p;    "beam profiles parameters"
zk=3.14*(wk)^2/0.532;
%%%%%%%% Calculate the values of Y "theoretical"%%%%%%%%
%%%%%%%%%%%%% to all points X "experimental"%%%%%%%%%%
for j=1:l
Aj=X(j);
cont = zeros(1,180);        HIT
N=100000;
for t=1:180
y0= Aj*sin(2*pi*f*t);
for i=1:N
x =rand*2*r-r;
y= rand*2*r-r+y0;
z= rand*2*r-r;
if x^2 + (y-y0).^2 +z^2 < r^2
if x^2+y^2 < (wk/2)^2*(1+(z/zk)^2)
cont(t) = cont(t) + 1;
else
if x^2+y^2 <(wk)^2*(1+(z/zk)^2) & x^2+y^2 >(wk/2)^2*(1+(z/zk)^2)
cont(t) = cont(t) + 0.78;
else
if x^2+y^2 <(3*wk/2)^2*(1+(z/zk)^2) & x^2+y^2 >(wk)^2*(1+(z/zk)^2)
cont(t) = cont(t) + 0.36;
else
if x^2+y^2 <(2*wk)^2*(1+(z/zk)^2) & x^2+y^2 >(3*wk/2)^2*(1+(z/zk)^2)
cont(t) = cont(t) + 0.10;
else
continue
```

```
      end
    end
   end
  end
 end
end
cont=cont/N;
end
MAX=max(cont);
MIN=min(cont);
Amp(j)=MAX-MIN;
Amp_norm(j)=Amp(j)/MAX;
    end
Diff(j)=Yn(j)-Amp_norm(j);
Diff2(j)=(Diff(j))^2;
Sum_diff(k)=sum(Diff2);
end
best_sum = min(Sum_diff);
k_best = find(Sum_diff == best_sum);
k_opt  = k_best(1)
wk_best = wmin+(k_opt-1)*p
zk_best=3.14*(wk_best)^2/0.532
plot(X,Yn,'-ro',X, Amp_norm,'-.b');
h = legend('experimental','calculated',2)
xlabel('modulation amplitude ($\mu$m)');
ylabel('Raman signal (arb. un.)');
title('Comparison theoretical/experimental');
```

Ringraziamenti

Desidero esprimere il mio ringraziamento alle persone che in questi anni hanno accompagnato e contribuito alla mia formazione e crescita professionale, nonchè alla realizzazione del presente lavoro di tesi in cui spero siano sintetizzati e ben custoditi tutti gli insegnamenti ricevuti.

E' davvero molto difficile esprimere in maniera adeguata la mia gratitudine al *supervisor* della mia attività di Dottorato, il professor Antonio Sasso. Lo ringrazio per avermi accolto nel suo gruppo come un padre, per avermi stimolato sempre in questi anni a dare il meglio di me, per aver creduto in me e nelle mie capacità. La sua saggezza, la sua pazienza, la sua grande umiltà ed onestà hanno ispirato la mia vita scientifica e non solo... e per questo gli sarò sempre debitrice.

Un sincero e speciale ringraziamento va alla Dr. Giulia Rusciano, che ha rappresentato la mia insostituibile guida e preziosa amica in questo lungo cammino. Il suo incoraggiamento incondizionato, i suoi preziosi suggerimenti ed insegnamenti, la sua amicizia mi hanno accompaganto in ogni passo di questo mio periodo di tesi. L'entusiasmo e le conoscenze che mi ha ispirato mi saranno compagne per tutta la vita. E' lei che mi ha aiutata a comprendere che per quanto possa essere dura...."il cielo è sempre più blu"!

Desidero inoltre ringraziere il Prof. Paolo Russo per aver partecipato con entusiasmo alla nascita e al faticoso sviluppo dell' esperimento condotto, fornendo spunti interessanti e una rilettura critica del testo.

Un doveroso riconoscimento va, inoltre, al Dr. Gigi Coraggio e al Dr. Giuseppe

Pesce per il loro sostegno nei momenti topici, per i suggerimenti e le intuizioni che spesso mi hanno permesso di superare agevolmente le difficoltà e accelerare i tempi di realizzazione di questo lavoro.

Un ringraziamento particolare va, infine, ai miei genitori, per avermi incoraggiato e sostenuto, incondizionatamente, nelle mie scelte; a mio fratello Vincenzo ed a Francesco per aver condiviso con me le ansie e le soddisfazioni affrontate in questo cammino, e senza i quali questi anni sarebbero stati più duri e molto meno piacevoli.

<div align="right">

Anna Chiara De Luca

Napoli, December 2008

</div>